



# **OPTICAL THEORY IMPROVEMENTS TO SPACE DOMAIN AWARENESS**

DISSERTATION

Tyler J. Hardy, Captain, USAF

AFIT-ENG-DS-16-S-011

**DEPARTMENT OF THE AIR FORCE  
AIR UNIVERSITY**

***AIR FORCE INSTITUTE OF TECHNOLOGY***

**Wright-Patterson Air Force Base, Ohio**

DISTRIBUTION STATEMENT A:  
APPROVED FOR PUBLIC RELEASE; DISTRIBUTION UNLIMITED

The views expressed in this dissertation are those of the author and do not reflect the official policy or position of the United States Air Force, the Department of Defense, or the United States Government.

This material is declared a work of the U.S. Government and is not subject to copyright protection in the United States.

AFIT-ENG-DS-16-S-011

OPTICAL THEORY IMPROVEMENTS TO SPACE DOMAIN AWARENESS

DISSERTATION

Presented to the Faculty  
Graduate School of Engineering and Management  
Air Force Institute of Technology  
Air University  
Air Education and Training Command  
in Partial Fulfillment of the Requirements for the  
Degree of Doctoral of Philosophy

Tyler J. Hardy, BSEE, MSEE  
Captain, USAF

September 2016

DISTRIBUTION STATEMENT A:  
APPROVED FOR PUBLIC RELEASE; DISTRIBUTION UNLIMITED

AFIT-ENG-DS-16-S-011

OPTICAL THEORY IMPROVEMENTS TO SPACE DOMAIN AWARENESS

Tyler J. Hardy, BSEE, MSEE  
Captain, USAF

Committee Membership:

Stephen Cain, PhD  
Chair

Major Michael Seal, PhD  
Member

Travis Blake, PhD  
Member

Benjamin Akers, PhD  
Member

ADEDEJI B. BADIRU, PhD  
Dean, Graduate School of Engineering and Management

**Abstract**

This dissertation focuses on increasing the ability to detect space objects and increase Space Domain Awareness (SDA) with space surveillance sensors through image processing and optical theory. SDA observations are collected through ground-based radar and optical systems as well as space based assets. This research focuses on a ground-based optical telescope system, the Space Surveillance Telescope (SST). By increasing the number of detectable Resident Space Objects (RSOs) through image processing, SDA capabilities can be expanded. This is accomplished through addressing two main degrading factors present in typical SDA sensors; spatial undersampling in the collected data and noise models and assumptions used in current algorithms. The assigned cost and a priori probabilities of a Bayes Multiple Hypothesis Test (MHT) are investigated in this dissertation to address the spatial undersampling. New algorithms are developed and tested, and demonstrated improved detection capabilities at operationally realistic false alarm rates. Additionally, a new noise model is developed which more accurately represents the received noise present in data collected with surveillance telescopes under certain atmospheric conditions. These algorithm have demonstrated probability of detection improvement of up to 80 percent in collected SST data over the currently employed detection techniques.

## **Acknowledgments**

I would first like to thank my advisor Dr. Cain. His guidance has been invaluable in helping me complete this dissertation. In addition, his professional mentoring will be a great asset going forward in my career. Thanks to Capt Kyle Stewart for helpful discussions on implementation techniques and Capt Jae Jeon for his inputs on the changing the number of hypotheses. I would like to thank the members of my committee for reviewing my research and giving valuable feedback. The time and effort they gave to my research was essential to creating this final product. Thank you to my wife and children. They kept me balanced and allowed me to put a lot of time and effort into completing this research.

Tyler J. Hardy

## Table of Contents

	Page
Abstract . . . . .	iv
Acknowledgments . . . . .	v
Table of Contents . . . . .	vi
List of Figures . . . . .	ix
List of Tables . . . . .	xiii
List of Symbols . . . . .	xiv
List of Acronyms . . . . .	xvii
 I. Introduction . . . . .	 1
1.1 Motivation . . . . .	1
1.2 System Description . . . . .	3
1.3 Research Goal and Objectives . . . . .	5
1.4 Document Organization . . . . .	5
 II. Background & Literature Review . . . . .	 7
2.1 Background on Space Object Detection . . . . .	7
2.2 Optical Modeling Overview . . . . .	15
2.3 Sampling Theory . . . . .	17
2.4 Developing an Accurate Model for Scintillation Noise Present in a PSF . . . . .	19
2.4.1 Overview of Atmosphere Theory . . . . .	20
2.4.2 Methods for correcting atmospheric effects . . . . .	23
2.4.3 Statistical models for scintillation . . . . .	26
 III. Improved Multiple Hypothesis Test through an Unequal Cost Assumption . . . . .	 30
3.1 SST Optical Model . . . . .	30
3.2 Theory Development . . . . .	35
3.2.1 Motivation and Selection of Alternate Hypotheses . . . . .	35
3.2.2 Detection Algorithm Based on Bayes Risk . . . . .	39
3.2.3 Model for Received Data Given Hypothesis $H_k$ . . . . .	41

	Page
3.2.4 Selecting a Cost Structure . . . . .	42
3.3 Experiment Description . . . . .	46
3.3.1 Locating and Selecting False Alarm Data . . . . .	47
3.4 Results and Analysis . . . . .	48
3.4.1 Detection and False Alarm Computations . . . . .	48
3.4.2 Receiver Operating Characteristic . . . . .	57
3.5 Full Frame Implementation . . . . .	61
3.6 Conclusions . . . . .	63
IV. Investigating Multiple Hypothesis Test Prior Probabilities . . . . .	66
4.1 Introduction . . . . .	66
4.2 Theory . . . . .	67
4.2.1 Optical Model . . . . .	67
4.2.2 Bayes Cost and Priors Discussion . . . . .	67
4.2.3 Decision Space Analysis . . . . .	69
4.2.4 Hypothesis Test Derivation . . . . .	73
4.2.5 Hypothesis Independent Threshold . . . . .	77
4.2.6 Investigating Null Hypothesis Probability . . . . .	79
4.2.6.1 Simulation . . . . .	79
4.2.6.2 Analytic . . . . .	80
4.3 Experiment Descriptions . . . . .	82
4.3.1 Simulation Description . . . . .	82
4.3.2 Collected telescope data . . . . .	83
4.3.3 Setting False Alarm Probability for Collected Data . . . . .	85
4.4 Results . . . . .	86
4.4.1 Decision Space Results . . . . .	86
4.4.2 Processing Simulated Data with MHT Algorithms . . . . .	89
4.4.3 Processing SST Data with MHT Algorithms . . . . .	91
4.5 Full Frame Implementation . . . . .	96
4.6 Conclusions . . . . .	97
V. Characterizing Point Spread Function fluctuations to improve Resident Space Object detection . . . . .	99
5.1 Methodology . . . . .	99
5.1.1 Optical Model . . . . .	101
5.1.2 Detection Theory . . . . .	104
5.1.3 Received Noise Distributions . . . . .	105
5.2 Simulation Description . . . . .	107
5.2.1 Evolving Phase Screen Over Time . . . . .	107
5.2.2 Final System Model and Implementation . . . . .	108



	Page
5.3 Results and Analysis . . . . .	111
5.3.1 Distribution Matching . . . . .	111
5.3.2 Receiver Operating Characteristic Curves . . . . .	113
5.4 Conclusions . . . . .	118
VI. Summary and Future Work . . . . .	120
6.1 Work Completed . . . . .	120
6.2 Algorithm Comparison . . . . .	122
6.3 Future Research Items . . . . .	123
6.4 Publications . . . . .	126
Bibliography . . . . .	127

## List of Figures

Figure	Page
1.1 NASA visual representation of objects in Earth's orbit [5]. . . . .	2
1.2 Model and optical diagram of the Mersenne-Schmidt design for the SST. [13] .	4
2.1 Number of total NEO and large NEA discoveries as of 15 July 2014 [8]. . . . .	8
2.2 Diameter of currently discovered and cataloged Near-Earth Asteroidss (NEAs) [8]. . . . .	9
2.3 LINEAR system detection block diagram based on [16]. The SST system utilizes a similar approach to detection. . . . .	10
2.4 Hierarchy of space object detection techniques considered in this research. This visualization demonstrates how the point detection, matched filter, Binary Hypothesis Test (BHT), and MHT algorithms are related. . . . .	13
2.5 Example of four simulated Point Spread Functions (PSFs) impacted by spatial undersampling caused by Charge-Coupled Device (CCD) pixels. Each PSF is shifted, but also changed in the shape and intensity distribution. . . . .	18
2.6 Hufnagel-Valley $C_N^2$ as a function of elevation in meters. $C_N^2$ represent the strength of the turbulence in the atmosphere. . . . .	21
2.7 Simulated star captured with both (A) short and (B) long exposure time, $T_s$ . . .	22
2.8 Block diagram of an Adaptive Optics (AO) telescope system [43]. . . . .	25
3.1 A graphical example of the division of a pixel into sub-pixel location for varying $M$ where the star in each figure represents the modeled location of the object and the dot is the true location. (A) Simple Binary test, $M = 2$ (B) Multiple hypothesis test with $M = 6$ , with sub-pixel hypotheses at the four corners and center of the pixel (C) A highly sampled pixel space with $M = 121$ hypotheses. . . . .	37

Figure	Page
3.2 Equal cost algorithm variables with an object present, $\eta_1$ and $\phi_1$ . These variables are observed over a 15-frame window, and the means and standard deviations are used to determine $P_d$ at frame 800. This data was collected on 13 Mar 2012. . . . .	51
3.3 Unequal algorithm $\mathcal{L}_u$ for a 15 frame window centered at 800 for 13 Mar 2012. The mean and standard deviation are calculated to give the probability of detection or false alarm $\mathcal{P}_u$ . . . . .	53
3.4 $P_d$ curves for ANIK-F1 as it enters eclipse on 3 consecutive nights (A) 13 Mar 2012 (B) 14 Mar 2012 (C) 15 Mar 2012. The solid black line is the Unequal-Cost Equal-Prior (UCEP) algorithm, the blue dashed line is the Equal-Cost Equal-Prior (ECEP) algorithm, the red dotted and dashed line is a binary matched filter, and the brown dotted line is a point detector. These detection curves are generated with $P_f = 4.56e - 10$ and $M = 10$ . . . . .	54
3.5 ROC curves centered at frames (A) 800 (B) 850 (C) 900 from 13 March 2012 using a 15 frame window with $M = 10$ . . . . .	58
3.6 ANIK-F1 at 3 points during the eclipse, captured with the SST. The frames used are (A) 800, (B) 850, and (C) 900 on 13 March. ANIK-F1 loses intensity as it enters the eclipse and more close resembles the background. . . . .	59
3.7 ROC curve using UCEP MHT, $\mathcal{L}_u$ , at frame (A) 800 (B) 850 and (C) 900 from 13 March 2012 using a 15 frame window. Three values of $M$ are compared: 2, 6, and 10. . . . .	60
4.1 Decision space within a single CCD showing all sub-pixel locations, along with the locations of the nine alternate hypotheses. . . . .	70

Figure	Page
4.2 Decision space analysis for a single SST CCD pixel. The hypothesis assignment matrix for (A) the correlation metric, $\mathcal{H}_c$ , and (B) distance metric, $\mathcal{H}_d$ . Each color shade corresponds to a similar hypothesis. Sub-pixel positions are tested every $1\mu\text{m}$ . . . . .	72
4.3 Analysis of $P_d$ for varying $\pi_0$ prior probabilities for $P_f = 1e - 10$ . . . . .	80
4.4 Flow diagram of process to (A) simulate data with an RSO present and (B) simulate data with no RSO present. Both data sets are needed to generate Receiver Operating Characteristic (ROC) curves. . . . .	84
4.5 Comparison of three proposed methods: distance, correlation, and empirical based methods of assigning sub-pixel positions. . . . .	87
4.6 A single instance of a ROC curve for both the ECEP and Equal-Cost Unequal-Prior (ECUP) algorithms. Simulated RSO and data with no objects present are needed to generate probability of detection and false alarm. . . . .	90
4.7 Statistical comparison of ECEP and ECUP algorithms over 100 monte carlo iterations. $P_d$ values for both algorithms are found for a false alarm probability of $P_f = 1e - 10$ . . . . .	92
4.8 A sample subset of SST data processed with (A) the ECEP algorithm and (B) the ECUP algorithm. In this example, one additional detection is observed. . .	93
4.9 Difference in number of binary detections, $\Delta_o$ , over 32 sample frames from data collected on nights (A) 073, (B) 074, and (C) 075. . . . .	94
4.10 Combined histogram for $\Delta_o$ , the number of additional binary detections with ECUP algorithm. All three nights analyzed 073-075 are included. . . . .	95
5.1 Diagram of two potential different atmosphere propagations. In (A) a multiple step propagation is demonstrated, in (B) a single phase screen directly against the pupil is demonstrated. . . . .	109

Figure	Page
5.2 Error between candidate Probability Density Functions (PDFs) and received intensity fluctuations. $E_{\text{RMS}}$ is calculated for a variety of seeing values, $r_o$ . . .	112
5.3 A demonstration of a simulated received PSF under two different conditions. In (A) a long exposure atmosphere model is used, and in (B) a PSF generated with the negative binomial and Poisson model or the ideal mixed PDF. . . . .	114
5.4 Log-Likelihood Ratio (LLR) observations over 100 Monte Carlo iterations. The LLR is generated for both the (A) Gaussian algorithm and the (B) mixed PDF algorithm. . . . .	115
5.5 ROC curves comparing the new mixed PDF (solid line) against the traditional Gaussian detection algorithm (dashed line). These curves were generated with simulated RSO and background data. . . . .	117
6.1 $P_d$ versus computational complexity diagram for several SDA algorithms. Processing time for a full frame of SST data is also included. . . . .	123

## List of Tables

Table	Page
1.1 SST System Parameters. [13] . . . . .	4
3.1 Average measured optical aberration Zernike coefficients, $a_j$ for the SST. . . .	32
3.2 List of hypotheses considered and a description of object location at the CCD. .	36
3.3 Apparent magnitude improvement of Equal and Unequal MHT over the current BHT at 50 percent detection threshold. . . . .	56
3.4 Processing times for equal- and unequal-cost algorithms processed on graphics card. . . . .	63
4.1 The sub-pixel locations of the $M$ hypotheses ( $\mu m$ ) along with the calculated priors $\pi_k$ and weighting values $W_k$ based on the empirical method. . . . .	89
4.2 Average number of additional binary detections by ECUP, $\bar{\Delta}_o$ , and standard deviation, $\sigma_{\Delta_o}$ , for three nights 13-15 March 2012. . . . .	95
6.1 Description of MHT algorithms including the assignment of costs and prior probabilities and where they are developed. . . . .	122

## List of Symbols

Symbol	Definition
$a_j$	Zernike weighting coefficients for aberrations
$A(x, y)$	Amplitude function
$B$	Background photons observed
$b_j, c_j$	Zernike weighting coefficients for atmospheric aberrations
$C_{ik}$	Cost function
$C_N^2$	Refractive index structure function
$d$	Aperture Diameter (meters)
$D(x, y)$	Received data
$F$	Cumulative Distribution Function
$f$	Focal Length (meters)
$f_c$	Cutoff frequency
$f_x, f_y$	Spatial frequency coordinates
$h(x, y)$	Point Spread Function
$H_k$	$k^{\text{th}}$ Hypothesis
$\mathcal{H}(\alpha, \omega)$	Matrix of selected Hypotheses for the position $\alpha, \omega$
$I(x, y)$	Model of received data
$j$	Imaginary number $\sqrt{-1}$
$\mathcal{L}$	Likelihood Ratio Test
$M$	Number of hypotheses in test
$m, n$	Pupil plane coordinates
$\mathcal{N}(\mu, \sigma)$	Gaussian distribution with mean $\mu$ and variance $\sigma$
$N_x, N_y$	Total number of pixels in image
$P(m, n)$	Pupil Function

Symbol	Definition
$\mathcal{P}$	Probability of detection or false alarm
$P_d$	Probability of detection
$P_f$	Probability of false alarm
$p(\mathbf{D} H_k)$	Probability of data given $H_k$
$\mathcal{R}$	Bayes Risk
$r_o$	Atmospheric coherence diameter
$T_{\alpha,\omega}(x,y)$	Sub-pixel PSF matrix
$\ \vec{V}_k\ $	2 norm for distance based prior assignment
$W_k$	Weighting term for $k^{\text{th}}$ hypothesis
$x, y$	Detector plane coordinates
$Z(m, n)$	Zernike Polynomials
$Z_j$	$j^{\text{th}}$ observation space
$\theta(m, n)$	Phase errors from atmosphere or aberrations
$\theta_k$	Estimated photons for $k^{\text{th}}$ hypothesis
$\lambda$	Wavelength
$\beta$	Difference between Nyquist and actual sampling
$\alpha, \omega$	Sub-pixel position shifts
$\pi_k$	Prior probability for $k^{\text{th}}$ hypothesis
$\Delta$	Sample spacing
$\Delta_s$	Required Nyquist sample spacing
$\sigma$	Variance of received data
$\sigma_k$	Normalizing variance term
$\Gamma$	Threshold of test
$\eta$	Value of equal-cost test when $H_0$ is chosen
$\phi$	Minimum value of all equal-cost test hypotheses besides $H_0$



Symbol	Definition
$\tau$	Threshold test adjustment
$\Delta M$	Apparent Magnitude

## **List of Acronyms**

Acronym	Definition
ACS	Advanced Camera for Surveys
AFIT	Air Force Institute of Technology
AO	Adaptive Optics
BHT	Binary Hypothesis Test
CCD	Charge-Coupled Device
CDF	Cumulative Distribution Function
DARPA	Defense Advanced Research Projects Agency
DoD	Department of Defense
ECEP	Equal-Cost Equal-Prior
ECUP	Equal-Cost Unequal-Prior
FoV	Field of View
GEO	Geosynchronous Earth Orbit
GEODSS	Ground-based Electro-Optical Deep Space Surveillance
HST	Hubble Space Telescope
LINEAR	Lincoln Near Earth Asteroid Research
LLR	Log-Likelihood Ratio
LRT	Likelihood Ratio Test
MHT	Multiple Hypothesis Test
NASA	National Aeronautics and Space Administration
NRC	National Research Council
NEA	Near-Earth Asteroids
OTF	Optical Transfer Function
PDF	Probability Density Function

Acronym	Definition
PMF	Probability Mass Function
PSD	Power Spectral Density
PSF	Point Spread Function
RMSE	Root Mean Squared Error
ROC	Receiver Operating Characteristic
RSO	Resident Space Object
SNR	Signal to Noise Ratio
SDA	Space Domain Awareness
SST	Space Surveillance Telescope
UCEP	Unequal-Cost Equal-Prior
UCUP	Unequal-Cost Unequal-Prior
WSMR	White Sands Missile Range

# OPTICAL THEORY IMPROVEMENTS TO SPACE DOMAIN AWARENESS

## I. Introduction

### 1.1 Motivation

The motivation for this research is to increase Space Domain Awareness (SDA) capabilities by proposing a new detection algorithm that improves the ability to detect space objects. SDA is a large field that encompasses several components including the detection, tracking, and characterization of space objects. These objects include satellites, orbital debris, and Near-Earth Asteroids (NEA). SDA is currently achieved through multiple methods including ground and space-based optical systems and ground-based radars. This research effort focuses on ground-based observation telescopes, specifically the Space Surveillance Telescope (SST). The SST is a telescope built by MIT Lincoln Labs under the direction of the Defense Advanced Research Projects Agency (DARPA). The mission of the SST program is “to enable ground-based, broad-area search, detection and tracking of small objects in deep space for purposes such as space mission assurance and asteroid detection [1].” The SST is a large field-of-view telescope with the ability to quickly scan the night sky and detect and track objects in the Earth’s orbit, as well as deep space asteroids.

There are multiple stakeholders in SDA data collection. They include the Department of Defense (DoD) and other US and foreign government agencies. These agencies have published space policies that include improving SDA data collection as a priority for their organization [2–4]. It is important that space objects in orbit are cataloged in order to mitigate their potential to cause severe damage to space assets through collisions or malicious actions. Avoiding space objects is critical to maintaining functional space assets and retaining a tactical edge in the space domain. Information collected by the SST and

other SDA telescopes is used for achieving the goals outlined in US space policies and for maintaining a robust and accurate SDA picture. Any improvements in the ability of the SST to detect objects in orbit will help in satisfying this goal of improved detection and characterization of space objects. Figure 1.1 is a visual representation of objects located in Earth's orbit. It provides a graphical example of the orbital areas that contain the most congestion and concern. 95 percent of the objects displayed in Figure 1.1 are orbital debris [5].

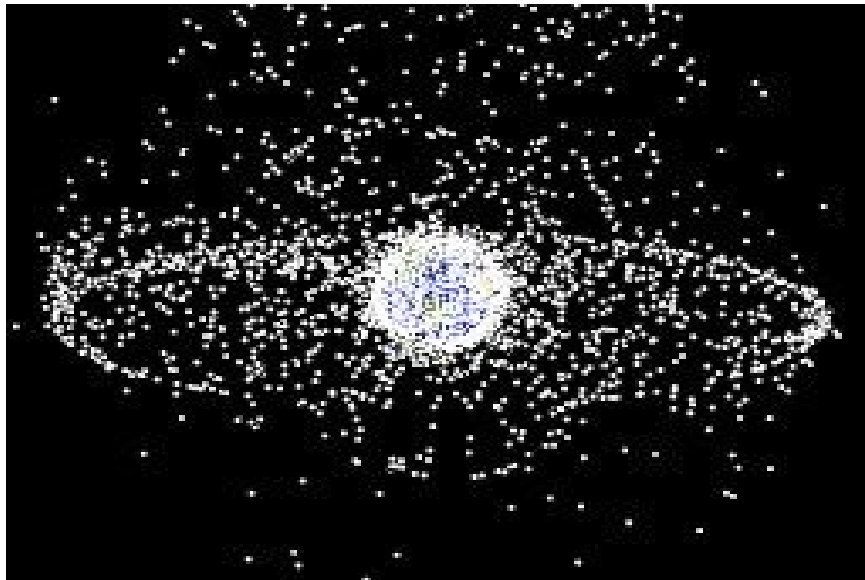


Figure 1.1: NASA visual representation of objects in Earth's orbit [5].

In addition to the detection of objects in orbit, detecting NEAs is another part of the SST's mission. National Aeronautics and Space Administration (NASA) has been tasked with detecting 90 percent of the NEAs that pose a severe threat to humankind by 2020 [6]. These objects are defined as asteroids larger than 140m in diameter that have a perihelion distance of less than 1.3 Astronomical Units from the sun. In a 2010 National Research Council (NRC) report on the progress towards this goal, it was determined that the NEA survey is not on track to be completed by 2020 [7]. One major challenge identified is

the lack of necessary funding. These conclusions were further detailed in a 2014 NASA Inspector General report [8]. Due to a lack of necessary funding, as stated in these reports, there is a significant benefit to utilizing existing telescope systems to improve SDA data collection efforts. Improving the ability of the SST to detect dimmer and smaller objects will improve the progression towards the mandated goal, with little or no additional cost or hardware. At the time of this report, NASA believes they have currently surveyed 10 percent of the 90 percent goal, with many of those surveyed objects being larger than 1km.

Multiple studies have investigated the environmental and population risk factors caused by NEAs. In [9], Chapman demonstrates that impacts from objects as small as 1km, many of which are still not cataloged as stated previously, have the potential to destabilize the global ecosystem threatening human civilization. Other studies explore other potential asteroid impact factors, including an ocean impact study by Morrison et. al. [10], and bias corrected impact prediction data by Stuart and Binzel [11].

## **1.2 System Description**

This dissertation focuses mainly on the SST. To investigate the research questions proposed, both simulated and captured SST data is processed with the newly developed detection algorithms. The SST system is a Mersenne-Schmidt design and is currently located at the White Sands Missile Range (WSMR) in New Mexico at approximately 8,000ft elevation [12]. The weather and altitude provide generally favorable conditions for data collections on most nights. Table 1.1 shows additional key system parameters of the SST. Figure 1.2 shows an optical diagram of SST as well as a model of the complete telescope system.

The SST is currently anticipated to be moved to Exmouth, Australia. This will improve the global coverage compared to the currently implemented Ground-based Electro-Optical Deep Space Surveillance (GEODSS) network. In addition, a second

Table 1.1: SST System Parameters. [13]

Parameter	Value
Focal Length	3.5m
Primary Mirror / Obscuration	3.5m / 1.75m
CCD Pixels Size	$15\mu\text{m} \times 15\mu\text{m}$
Total Number Pixels	6144x4096
Center Wavelength	500nm

telescope may be installed at the WSMR to replace the original. Any new algorithms can potentially be implemented in the original telescope, or updated to the new data processing pipeline.

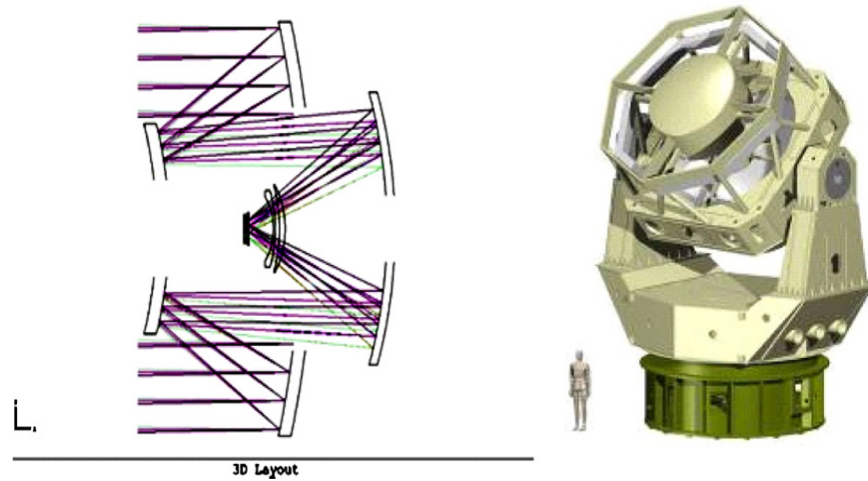


Figure 1.2: Model and optical diagram of the Mersenne-Schmidt design for the SST. [13]

### **1.3 Research Goal and Objectives**

The goal of this research is to improve the detection capability of current ground-based SDA optical telescopes with new detection algorithms by addressing two main degrading factors: spatial undersampling and the received noise assumptions. This dissertation addresses this research goal with the following research questions. These research questions led to the three main topics covered in this dissertation.

1. Will a new realistic cost function improve the detection performance of a Bayes Criterion MHT?
2. Do the assignments of a priori probabilities in a MHT improve the detection performance?
3. Can using a more realistic noise model for detection algorithms increase the ability to detect space objects?

Research questions 1 and 2 address the spatial undersampling, and research question 3 addresses the received noise assumptions.

### **1.4 Document Organization**

This document is organized into 6 chapters that cover the relevant background, as well as each research question addressed in section 1.3. Chapter 2 is a review of relevant background and publications in this research area. The background includes detection theory and a review of current and newly proposed algorithms. In addition, a review of atmospheric theory and methods for correcting for the atmospheric effects present in SDA data collections is presented.

Chapter 3 explores the development of a new detection algorithm. This algorithm is based on an unequal-cost MHT, expanding on previously developed matched filter and equal cost MHT algorithms.



Chapter 4 examines the segmentation of a single pixel into the decision space for a MHT. This segmentation is used as a basis for the prior probabilities used in a MHT. Simulated and collected telescope data are both analyzed.

Chapter 5 investigates the underlying statistics of the received data. The goal with this portion of the research is to expand upon the Gaussian distribution of noise assumed in the Chapter 3. The atmosphere and random photon arrival times are investigated to create an accurate joint model. Chapter 6 covers the future work that can be investigated after this dissertation.

## **II. Background & Literature Review**

This chapter outlines background research and discoveries that relate to the research topics discussed in this dissertation, with two main topic areas. The first topic area is background on space object detection, focusing on both the history and current methodology used. The second topic area is an investigation of the properties and effects of the atmosphere, and the methods of dealing with its impact on imaging systems.

### **2.1 Background on Space Object Detection**

The SST is one of the latest systems to collect data on space objects, including NEA detection. Before the use of Charge-Coupled Device (CCD) technology, searches for NEAs were conducted by two main methods. The first method involved the human eye and using memory or note-taking to capture object locations. Through these observations, astronomers could determine differences in object position over time in order to locate asteroids. When photograph technology became available, the comparison of film images allowed for detailed comparison over time. Film comparison is more exact, but still requires manual analysis, limiting the quantity of information that can be processed and the complexity of the algorithms that can be used.

Figure 2.1 is a plot of the number of NEA objects detected by year. It demonstrates that the vast majority of these objects have been found and cataloged in the past 20 years. In addition, a small percentage of the cataloged objects are what NASA classifies as large NEAs.

As Figure 2.1 shows, large advancements in the discovery of asteroids have occurred over the last 20 years. These discoveries can be tied to the use of digital detection techniques. The Spacewatch program began developing digital detection techniques in the early 1980s [14]. This program involves capturing images with CCDs, and processing

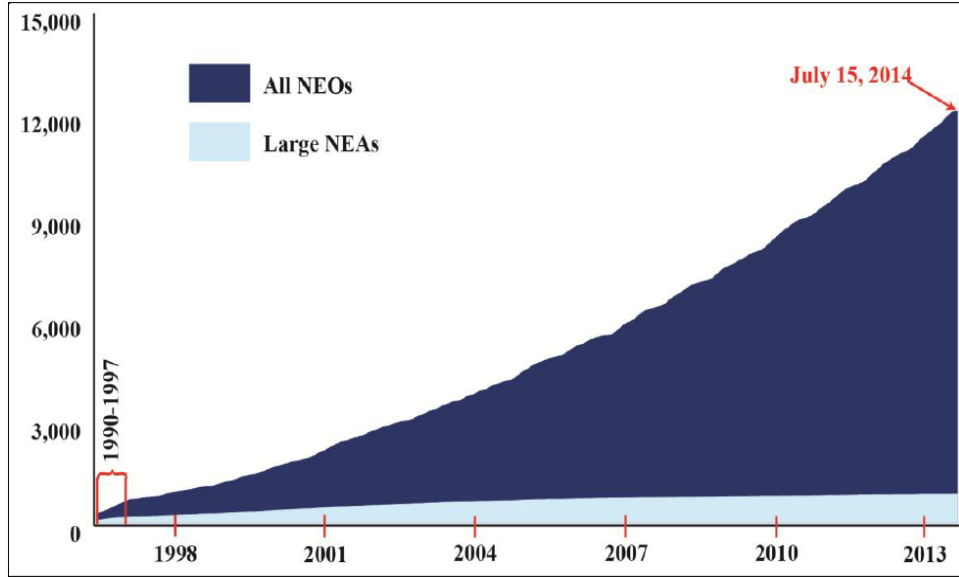


Figure 2.1: Number of total NEO and large NEA discoveries as of 15 July 2014 [8].

the data with moving object detection algorithms. As awareness and understanding of the threats posed by NEAs and space debris detection rose, additional programs and research efforts were created to address these issues. Figure 2.2 demonstrates the diameters of discovered NEA objects. As the diameter of the space object increases it becomes more easily detectable with ground-based telescopes, and a larger percentage of the objects are discoverable. Larger objects occur less frequently than smaller objects, so there are less to be discovered.

Another program of note is the Lincoln Near Earth Asteroid Research (LINEAR) program. Details about the LINEAR program are given by Stokes *et al.* in [15]. LINEAR uses a GEODSS telescope to capture images together with a Binary Hypothesis Test (BHT) point detector to detect NEAs. As described by Viggh *et al.*, a point detector is used to generate a binary map of ones and zeros signifying where objects are present [16]. The SST currently uses a similar point detection algorithm to LINEAR. A binary map is generated in a similar method to LINEAR, and then detections are monitored over three

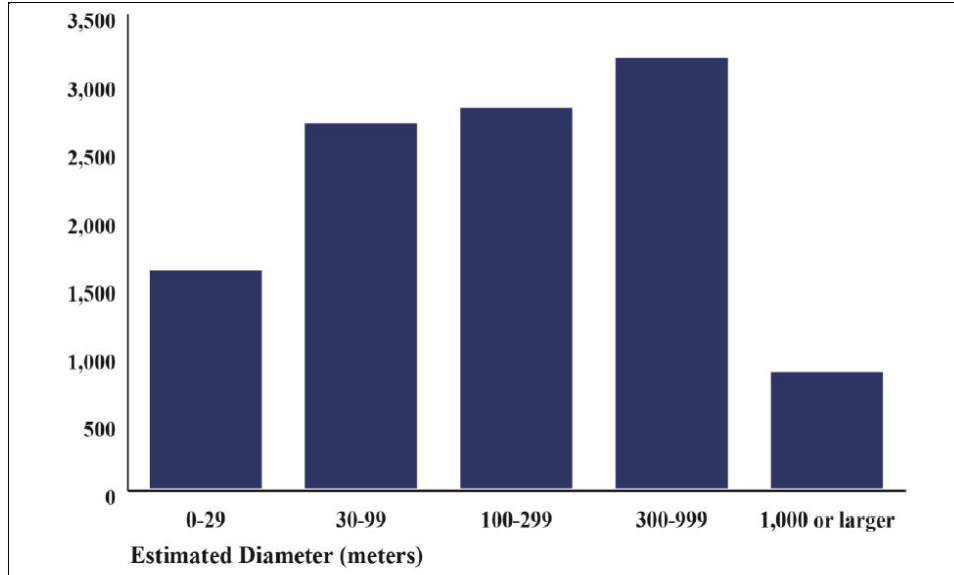


Figure 2.2: Diameter of currently discovered and cataloged NEAs [8].

consecutive frames to make a final detection decision. If three consecutive detections are observed, there is considered to be an object present. This method of detection works well if the majority of the object's intensity is in a single pixel. A point detector yields the largest possible Signal to Noise Ratio (SNR) for that pixel, and the greatest chance for detection. A point detector can be implemented with relative simplicity and does not have large computational requirements. A major drawback of this method is that the intensity from an object can be spread over multiple pixels, reducing the peak intensity of any single pixel. Figure 2.3 is a block diagram depicting the entire detection process used by LINEAR [16].

The detection process contains three important elements: data capture and pre-processing, the detection algorithm, and post-processing and output. When discussing detection algorithms, the middle two blocks are the processes being referenced. The pre- and post-processing portions can remain the same regardless of the detection theory used to generate a binary map.

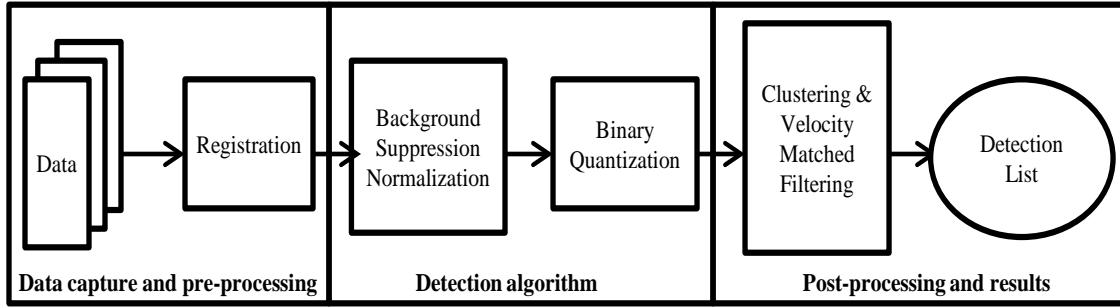


Figure 2.3: LINEAR system detection block diagram based on [16]. The SST system utilizes a similar approach to detection.

Recently more emphasis has been put on the characterization, modeling, and resolved imaging of space objects. Gathering this information can provide additional detail on the object, but each collection technique presents its own technical challenges. This research does not address this aspect of SDA. The detections and tracks generated from the search telescopes, including the SST studied in this research, will lead to follow-up investigations by other sensors to gather additional information. The follow-up sensors may collect the necessary characterization data. Additionally, the detection algorithms and techniques developed in this dissertation can be applied to other research areas. One example is star tracking for communications or navigation. The space objects and stars both appear as point sources, and can be processed similarly. Increasing the number of detected stars in an image by using advanced detection techniques can potentially increase the pointing or navigation accuracy of star trackers.

There are three key factors that impact the types of detection algorithms that are developed, and their effectiveness in detecting space objects. It is important to understand the conditions under which the data is collected. The following assumptions are made about the data:

- All objects observed through the optics are unresolved point sources. The apparent size of space objects on the detector are not necessarily limited to one pixel due to intensity spreading effects including optical aberrations or atmospheric effects. Since the objects are unresolved, there is no need for image reconstruction algorithms which can be computationally costly.
- The decisions about an object being present or not are made only by the data available in a single frame or captured image. The persistence of Resident Space Objects (RSOs) may be noted frame to frame to reduce false alarms, as is the case with the SST. There are algorithms that can take advantage of multiple frames to increase detection performance, but these are not investigated in this dissertation.
- In Chapters 3 and 4, the frames are collected with long exposure imaging. According to Goodman, long exposure images are captured with an integration period of greater than 10ms [17]. Additionally, the integration time is not long enough to cause objects moving at sidereal rate to streak.

Noting these assumptions, more specific detection algorithms can be developed that take advantage of the known data collection methods. With the increase in computer memory and processing speed, increasingly advanced detection algorithms have become possible. Methods that do more than compare single pixels against a threshold provide greater detection ability at the cost of processing complexity. Using the expected image of an object viewed as a point source, or Point Spread Function (PSF), to search and make detection decisions is known as a matched filter technique. This method allows more than a single pixel to be used in the detection decision. Matched filtering effectively averages the noise over all the pixels used. One current standard for a matched filter algorithm used in multiple NEA programs is SExtractor, proposed by Bertin in [18]. This is a software package that processes astronomical images and performs detection and classification of

objects. The portion of SExtractor that relates to this paper is the detection, or thresholding, step. The authors propose a method of convolution between the received data and the PSF for faint unresolved objects, the type of objects investigated in this paper. Additional methods by Bertin applying SExtractor and improving the algorithm can be found in [19, 20], these improvements utilize the traditional matched filter technique.

Matched filter space object detectors can be separated into two categories: spatial only, and spatial and temporal. In a spatial only target detection, only the spatial characteristics of the object being investigated are utilized in the detection process, which can include the shape and intensity distribution. This type of algorithm is used when the object does not move significantly during the integration time of the image. Matched filter algorithms accounting for both space and time are also utilized for detection of space objects. In these algorithms by Gural et. al and Pohlig, the spatial and temporal characteristics are both used to make detection decisions [21, 22]. These detection algorithms are not investigated further in this paper because they do not match the data collection methods used in the SST, where the integration time does not allow for significant orbital motion.

In spatial matched filtering, it is important to have an accurate model or prediction of what the object is expected to look like in the imaging system. In [23], O'Dell shows that the spatial sampling of the CCD pixels impacts the resulting image. The author investigates the effects of sampling at both Rayleigh and Nyquist rates, and demonstrates the impact on detection performance of a matched filter in undersampled systems.

In [24], Zingarelli demonstrates a method for increasing the detection performance over a traditional matched filter technique in undersampled systems. Recognizing that where the object is formed within a CCD pixel will change the distribution of the image, the author creates multiple potential PSFs for comparison. This leads to a MHT, where multiple sub-pixel locations of objects are used to create modeled PSFs to compare potential objects against. A key factor in the development of the MHT is assigning the costs

and prior probabilities of the hypotheses, which represent two of the research questions and are investigated in Chapters 3 and 4 respectively. Figure 2.4 shows the structure of the relevant detection algorithms described in this section. As shown in Figure 2.4, the detection algorithms considered to this point can be described in a hierarchy. This dissertation focuses on the matched filter MHT, and the choices for assigning costs and prior probabilities.

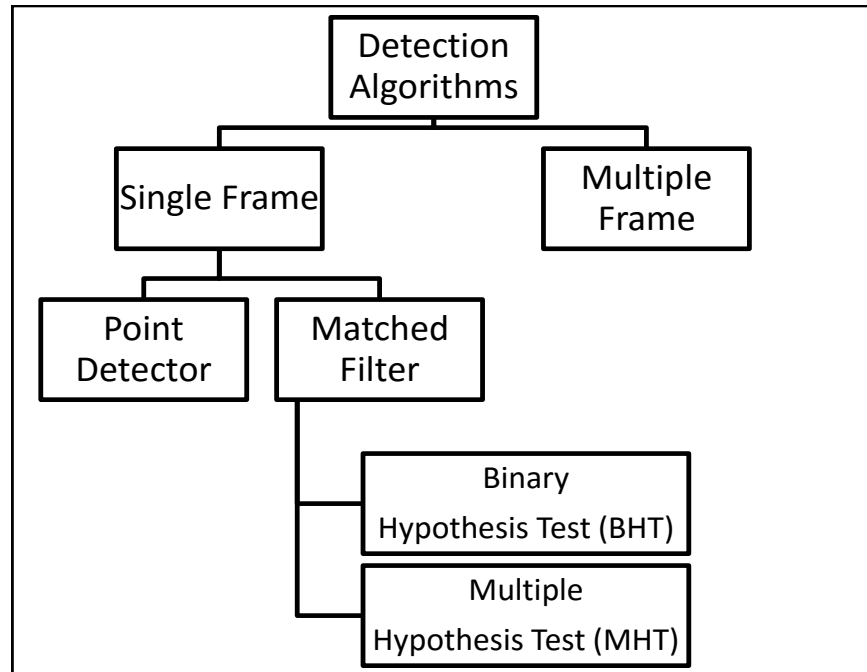


Figure 2.4: Hierarchy of space object detection techniques considered in this research. This visualization demonstrates how the point detection, matched filter, BHT, and MHT algorithms are related.

In addition, the choice for the received noise can be applied to any of the detection algorithms shown in Figure 2.4, potentially changing the performance of the algorithms. One key factor in building a detector is accurately modeling the distribution of the expected received data. In Chapters 3 and 4, it is assumed that the received data is Gaussian, but a



method is presented for implementing non-Gaussian received data tests with different costs and prior probability assumptions. In Chapter 5, a new model for noise in the PSF is developed, and a detection algorithm based on the model is used.

The MHT proposed in this research is based on a Bayes risk described by Van Trees [25]. In Bayes risk there are two important variables that can be assigned that change the form and effectiveness of the test. They are the costs associated with selecting each hypothesis and the prior probabilities, or the probability of each hypothesis occurring. While multiple hypothesis detection based on Bayes risk is a relatively new research area in SDA, it has applications in several other areas. One of these is the detection and classification of reflecting objects in radar imagery investigated by Ertin [26]. The authors present an unequal cost MHT, by penalizing misclassification of objects differently than missed detections or false alarms. A key difference is that the choice for the cost of a misclassification still requires the algorithm to make a classification decision, which is not done in Chapter 3. Another example of unequal cost MHT is the removal of symbols with errors in a frequency-hop communication system investigated by Baum and Pursley [27]. Again, different choices for costs and received data assumptions lead to different algorithms.

Unequal prior probability has use in other research areas outside of SDA and space object detection. Often in cases where the input conditions might change, and adapting the assumptions or inputs to the algorithm may provide additional performance gains. These input conditions are the prior probabilities. Cognitive radar [28], neural networks [29] and adaptive algorithms [30, 31], Bayes estimators [32], and quantization of prior probabilities [33] are research areas that have investigated this effect. In some cases the focus is comparing equal vs. unequal prior probabilities only, but some research has also been done on a non-constant assignment of priors. In the case of the SST and SDA, the priors may change between collections or frames due to changing atmospheric conditions.

Decisions about how often the priors need to be updated, or the optimal feedback for the priors are not covered in this research. In the next section, the relevant background for the optical model is discussed.

## **2.2 Optical Modeling Overview**

A key element in this research is choosing an accurate optical model. The optical model developed here is used for several purposes throughout this research, including simulating data and creating the PSFs for the matched filter algorithms. This section provides a brief overview of the model and details where the model is described further.

Depending on the research area, different aspects of the optical model are used. The main components of an optical model can be described by the following four factors: the propagation model, the model for aberrations, atmospheric model, and the received noise model. In this dissertation, the light captured by the telescopes is generally incoherent. This is because the source of the light from RSOs in orbit is reflected incoherent sunlight. Additional complications and considerations are required for coherent light, but these topics are not considered in this research.

The first step in creating an accurate optical model is recreating the electromagnetic field as it propagates from one point in space to another. Rayleigh-Sommerfeld propagation is derived from Maxwell's equation and describes an electromagnetic field as the result of a wave traveling from one plane to another. Although it is the most accurate way to completely describe a field after a propagation, it is also the most computationally complex method for propagating a field. For the large CCD arrays considered in this research, it is not feasible. Rayleigh-Sommerfeld propagation can be reduced by making an assumption about the distance from the source to the receiver plane, along with the relative size of source and receiver planes [34]. These factors determine which method can be accurately implemented.

$$z^3 \gg \frac{\pi}{4\lambda} \left[ (x - \xi)^2 + (y - \eta)^2 \right]_{\max}^2 \quad (2.1)$$

$z$  is propagation distance between the source and received plane,  $\lambda$  is the wavelength being considered,  $x, y$  are receiver plane coordinates and  $\xi, \eta$  are source plane coordinates. If equation (2.1) is true, a Fresnel propagation can be implemented. A Fresnel propagation is less computationally complex than the Rayleigh-Sommerfeld propagation. The Fresnel approximation can be further reduced to a Fraunhofer propagation. Fraunhofer can be thought of as the far field effect of a propagation, or in the case where a focusing optic is employed. It is accurate when the following condition is met:

$$z \gg \frac{k(\xi^2 + \eta^2)_{\max}}{2} \quad (2.2)$$

where  $k$  is the wave number  $\frac{2\pi}{\lambda}$ . If this condition is met, it can be considered valid to utilize a Fraunhofer propagation. The benefit of using a Fraunhofer propagation is that it can be implemented with a two-dimensional Fourier Transform.

$$U(x, y) = \frac{e^{jkz} e^{j\frac{k}{2z}(x^2+y^2)}}{j\lambda z} \iint_{-\infty}^{\infty} U(\xi, \eta) \exp \left[ -j\frac{2\pi}{\lambda z}(x\xi + y\eta) \right] d\xi d\eta \quad (2.3)$$

$U(\xi, \eta)$  is the field at the source plane, and  $U(x, y)$  is the resulting field at the receiver plane. Throughout this dissertation, Fraunhofer propagation is used. To generate the PSF, the source field is assumed to be a single point source located at a significant distance from the aperture. The result of this first long propagation is a plane wave normal to the optic axis of the telescope system. The second propagation needed is from the telescope aperture to the CCD received plane. This is where the Fraunhofer propagation is computed. The propagation from aperture to receiver needs to take into account other factors, including the telescope aberrations and atmosphere, which are discussed next.

An imaging system can be considered diffraction limited “if a diverging spherical wave, emanating from a point-source object, is converted by the system into a new wave,

again perfectly spherical, that converges toward an ideal point in the image plane [34].” In other words, a diffraction limited system is an ideal system that contains no imperfection on the lenses or mirrors. The diffraction limited system has the largest spatial frequency content allowed by the aperture dimensions. Any aberrations added to a diffraction limited system limit the maximum allowable frequency.

In a non-diffraction limited system, the defects in the optics used, or aberrations, affect the formation of the image and generally need to be accounted for to create an accurate model. In Chapters 3 and 4, these aberrations are included in the model and described. In Chapter 5 aberrations are not included. This is because the focus of the research is on the temporal changes in the PSF caused by the atmosphere, and the lens aberrations are assumed to not change temporally over the integration period of the system.

The effect of the atmosphere on the optical model is captured in two different methods in this dissertation. These methods are dependent on the length of integration time used in the data collection. The two methods are a long exposure atmosphere and a short exposure atmosphere model. More details on the model for the atmosphere are discussed in section 2.4.

### **2.3 Sampling Theory**

The primary motivation for using a MHT is to overcome the effects of undersampling by the CCD pixels. If a telescope system is spatially undersampled, a small shift of where an object is formed within a single pixel can result in a different shape or distribution of intensity. Instead of shifting and retaining the spatial information, an aliased PSF loses spatial information and can have a different shape completely. This presents a problem in matched filter-based detection algorithms, where the goal is to match objects in the data to the hypothesized PSFs. Figure 2.5 shows four examples of an undersampled PSF model generated with a small sub-pixel shifts.

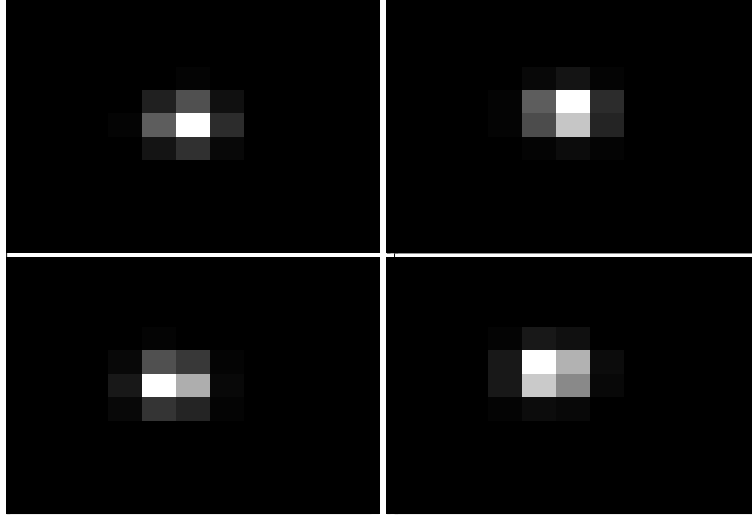


Figure 2.5: Example of four simulated PSFs impacted by spatial undersampling caused by CCD pixels. Each PSF is shifted, but also changed in the shape and intensity distribution.

As shown in Figure 2.5, the intensity and distribution of the PSF changes as the RSO is moved within a pixel. If the RSO is properly sampled, the PSFs would have the same shape, and only be shifted slightly in position. A common method of determining the sampling required is using angular resolution found through a Rayleigh criterion. In [23], O'Dell shows that in a matched filter detection algorithm, Rayleigh always undersamples when compared to the required Nyquist sampling. The required Nyquist sampling is found by combining the maximum frequency present in a diffraction limited system with the Nyquist theorem on minimum required sampling. This gives the following required spatial sampling,  $\Delta_s$ , described by Goodman [34]:

$$\Delta_s \leq \frac{\bar{\lambda}f}{2d} \quad (2.4)$$

where  $\bar{\lambda}$  is the center wavelength observed,  $f$  is focal length of the system, and  $d$  is the diameter of the pupil. Looking at the variables of equation (2.4), it is evident that there is a limited amount of user control in the required Nyquist sampling. The center wavelength

is a property of the observed light. The main method of selecting the desired sampling rate is the ratio of  $\frac{f}{d}$ , but these parameters are essential to other portions of system design. These design components include the Field of View (FoV) of the telescope and the physical dimensions of the system.

Substituting the SST parameters into equation (2.4), a center wavelength of 500nm with a focal length and pupil diameter of 3.5m, gives a required sampling size of  $0.25\mu\text{m}$ . The SST pixels are  $15\mu\text{m}$  square, but are grouped 2x2 in these data collections. The binned pixels give an actual sampling size of  $30\mu\text{m}$ . The difference between required and actual sampling in this case is 120 times. If the system is not diffraction limited, the actual undersampling factor will be much less. This is due to the pupil diameter  $d$  being limited by the effective seeing parameter,  $r_o$ . Seeing parameter values change depending on atmospheric conditions, but are typically smaller than 10cm at the Socorro, NM site.

## **2.4 Developing an Accurate Model for Scintillation Noise Present in a PSF**

The noise present in an image captured through a telescope can have several potential sources including read out noise, dark current, photon counting noise, and noise caused by the atmosphere. Traditionally, SDA detection algorithms have utilized a Central Limit Theorem justification to assume that the combination of all of the noise sources present in the system result in an overall Gaussian distribution of noise within the received data. Multiple research efforts have looked at detection algorithms based on the noise in the received data not being Gaussian. In multiple research efforts it is assumed that the noise is dominated by Poisson noise, and other sources do not contribute significantly [22, 35]. In these cases, a more complicated relationship is found to be necessary in order to implement the algorithm. One example of building a detector optimized for Poisson noise is investigated by Pohlig [22]. In this case, the dominant source of noise in the received data is the random arrival time of photons. The author states this can be achieved through a very

low noise CCD in low intensity collection. In [35], Peterson assumes that the distribution of the received data is Poisson, and the author achieves similar results.

The goal in this portion of research is to account for the two phenomenon present, and combine them into a single model. These phenomenon are the atmosphere and photon counting noise. It is well understood that noise due to random photon arrival times follows a Poisson distribution [17]. The impact of the atmosphere, and the fluctuations it causes in received intensity is less understood. This section outlines atmospheric theory that has been developed, as well as current methods for overcoming its effects.

#### ***2.4.1 Overview of Atmosphere Theory.***

The atmosphere causes random wavefront errors to any field that propagates through it, and these wavefront errors are due to changes in temperature and wind at different points in the propagation path that affect the index of refraction [36]. The degradation in image quality due to the atmosphere presents significant challenges across several types of imaging systems. Both coherent and incoherent optical systems, from laser systems and communication to ground based telescope imaging account for the effects of the atmosphere.

These systems utilize different techniques to improve the performance of the optical system. Given the fact that the atmosphere behaves as a random process, it is impossible to completely describe its behavior with a deterministic set of equations. Instead, many efforts have looked at determining the statistics of the atmosphere. Assuming the atmosphere is statistically homogeneous and isotropic, the covariance can be used to give a Power Spectral Density (PSD) as detailed by Andrews and Phillips [36]. The PSD is a function of the strength of turbulence in the atmosphere,  $C_N^2$ . In horizontal propagation,  $C_N^2$ , is often assumed to be constant. In vertical or slant imaging, as in stellar observations,  $C_N^2$  is often modeled as a function of elevation,  $h$ . Figure 2.6 shows an example plot of a popular model for  $C_N^2$ , the Hufnagel-Valley.

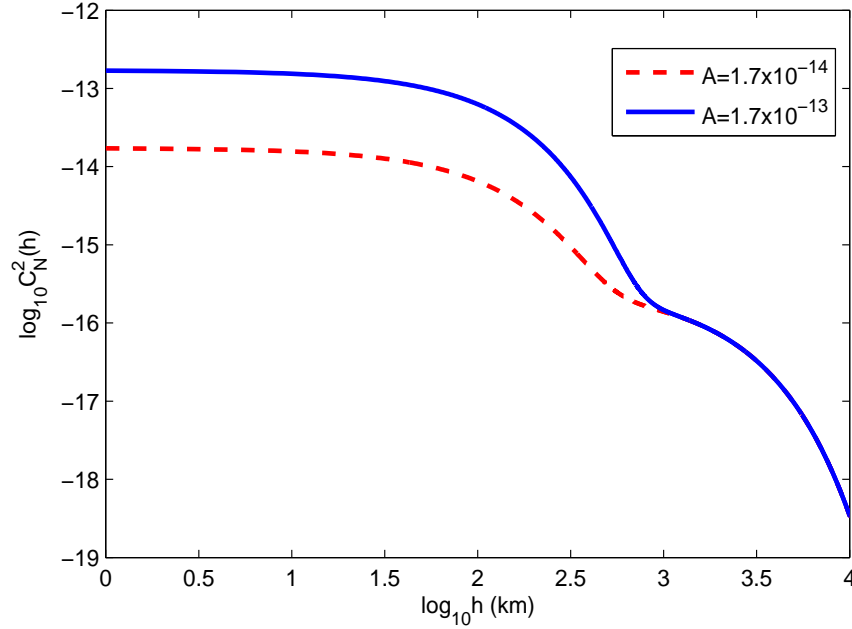


Figure 2.6: Hufnagel-Valley  $C_N^2$  as a function of elevation in meters.  $C_N^2$  represent the strength of the turbulence in the atmosphere.

The Hufnagel-Valley profile depends on the value of turbulence on the ground,  $A$ . This value affects the profile up to approximately 3000m. The value  $A = 1.7 \times 10^{-14}$  is selected for the commonly used H-V $_{\frac{5}{7}}$  model. Combining the statistical description of the atmosphere with known wave propagation equations, theoretical derivations can be made for the received fields, intensity, and intensity fluctuations. These are related to the first, second, and fourth order moments respectively.

The random phase errors in light propagated through the atmosphere cause changes in the shape, brightness, and location of the image formed at the focal length or CCD of an imaging system. These changes manifest as intensity fluctuations in the received image. These fluctuations are known as scintillation. Scintillation can present as a temporal fluctuation, such as a star twinkling over time, or as a spatial fluctuation, known as speckle [36]. Characterizing how scintillation can impact the PSF will result in an



improved statistical description of noise in the received data. Knowledge of noise statistics could potentially contribute to improving detection algorithm performance. A thorough summary of the progress towards understanding and correcting for the earth's atmosphere is described by Roddier in [37].

Accounting for the effect of the atmosphere on the PSF is dependent on the exposure time,  $T_s$ , used. In the short exposure atmosphere, the intensity has less spread, but contains more variance in shape, intensity, and location. The long exposure atmosphere averages the random phase effects, and as a result decreases the fluctuations, causing a larger spatial spread in the PSF. For exposure times much greater than 10ms, atmospheric effects are effectively averaged, and a long exposure atmosphere model can be accurately used. In the long exposure atmosphere model, the received data is assumed to be constant in time, and is a function of seeing, wavelength, focal length, and position. This is due to the fact that the intensity variance over time,  $\sigma_I^2$ , effectively goes to zero. For  $T_s$  much less than 10ms, the effects of the atmosphere are “frozen [17].” This leads to a large variance,  $\sigma_I^2$ . Figure 2.7 demonstrates two simulated images captured with a short exposure and long exposure time.

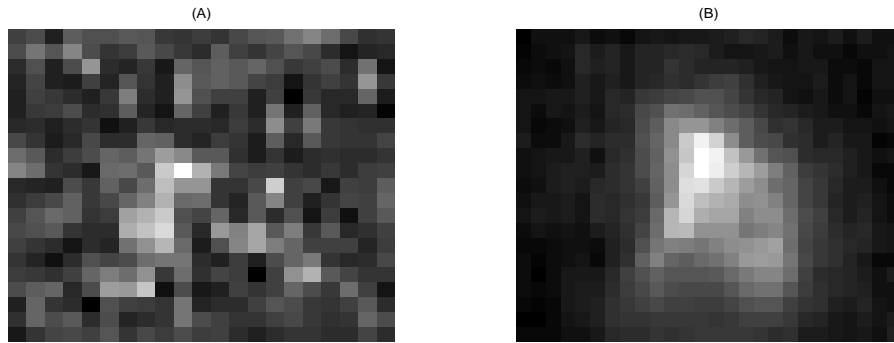


Figure 2.7: Simulated star captured with both (A) short and (B) long exposure time,  $T_s$ .

In (A), the short exposure image has two factors impacting its appearance. The first is that since a small exposure time is used, the captured intensity is quite low. As a result, it is more difficult to separate the object from background noise. In addition, the object may contain spatial variations due to the atmosphere. If a second short exposure image is shown, the effect of temporal scintillation could also be demonstrated by the change in intensity between the two images. In (B), the long integration time has allowed for more intensity, distinguishing the object more clearly from the background. In addition, the spatial dimensions of the object have increased due to the averaging of the atmosphere.

An example of a system operating in the short exposure model is found in the laser communication area. Characterizing intensity fluctuations are essential to the field of laser communications. The atmospheric degradation effect on laser beams causes a loss of intensity and the spreading of the laser spot. Due to the high data rates typically used, these systems operate in the short exposure regime. A key factor in a laser communication system is signal reliability, which is related to the PDF of the intensity according to Al-Habash et. al. [38]. For this reason, several research efforts have investigated the fundamental distribution of noise in the propagation of light through the atmosphere. Alternatively, a telescope imaging distant objects would need a large time period to collect a sufficient number of photons from the dim object. Identifying the characteristics of different atmospheric effects is important, and can help to determine appropriate methods for correcting them. Removing atmospheric spread provides an estimate of the original object, increasing clarity and resolution. More information about these efforts is included in the next section.

#### ***2.4.2 Methods for correcting atmospheric effects.***

There are several ways to mitigate atmospheric effects. Adaptive Optics (AO) and image restoration are two popular methods. They can be used individually or together to achieve increased performance. In AO, the wavefront errors are estimated, and a control

system is used to actuate deformable mirrors to correct for these errors before the image is formed at the CCD. Adaptive optics are implemented during the design phase of system development. Using AO, a portion of the wavefront errors are corrected before the image is digitally captured. This provides resolution benefits without post-processing of the data. The additional performance comes at a cost in hardware, sensing and control, and cost. Depending on the desired application and the benefits provided, these additional costs are not always justifiable. In AO corrected systems, there are often residual phase errors that are not corrected for. To correct for remaining errors, additional methods such as image restoration can still be used. In [39, 40], the issue of image processing in AO corrected images is investigated by Racine et. al. and Fusco et. al.

Adaptive optics systems are not investigated further in this research for two primary reasons. One of these reasons is that the SST system, which is the focus of this research, does not utilize an AO system. AO is not utilized in SST mainly due to the large FoV [41]. AO operates on the assumption that all portions of the received wave propagate through the same atmosphere or one that is highly correlated. In a large FoV collection, this assumption is not valid. Current research efforts have demonstrated AO correction over a 2 arcmin FoV— [42], a small percentage of the FoV of SST. The second reason AO are not investigated further is that the techniques developed here can still be utilized in an adaptive optics system. Figure 2.8 shows an example block diagram of an adaptive optics telescope system.

A second method often utilized is correcting for the atmospheric effects with image processing. In this case, no additional hardware is needed. The image formed at the CCD still contains the effects of the atmosphere, and post-processing is used to obtain the original image or to account for the atmosphere. Within the field of image processing, there are two important cases that lead to different approaches. These cases are resolved and unresolved imaging. In a resolved image, separate portions of an imaged object are

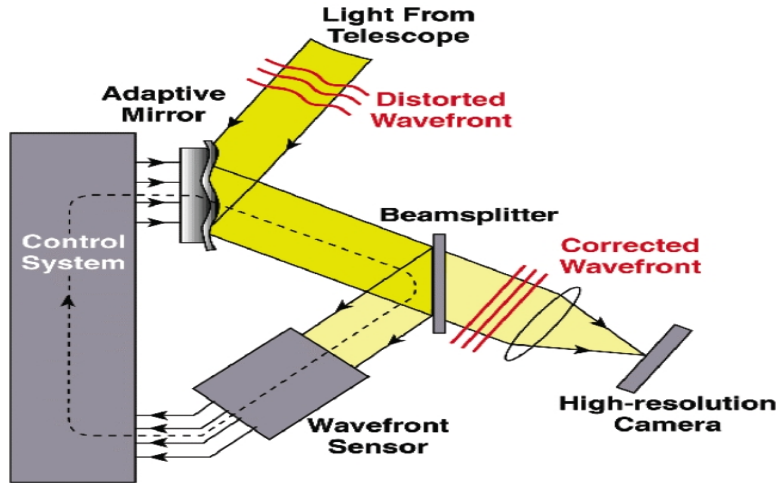


Figure 2.8: Block diagram of an AO telescope system [43].

able to be differentiated from each other. In an unresolved image, the object may occupy a single or small number of pixels, and much if not all spatial information about the object is lost. The ability to resolve an object is a function of several factors, including CCD sampling, lenses, wavelength, and the distance and size of the target. In resolved imaging, it is often desirable to use signal processing to remove the effects of the atmosphere. These systems are typically trying to capture physical characteristics of the object being imaged, and the blurring caused by the atmosphere degrades and limits this capability.

There are several proposed techniques for image restoration in resolved imaging. One common practice is to use deconvolution [44, 45]. In deconvolution, an estimate of the truth image is computed through the reversal of the process of image formation. From optical theory, an image is formed through the convolution of the truth object with the PSF of the optical system [34]. Using knowledge about the possible and likely PSF, an estimate can be formed of the truth object. Additionally, there are methods for estimating both the PSF and the original object, known as blind deconvolution.

In an unresolved imaging system, the spatial information of the object may not be as important. As a result, it is not necessary to implement costly image restoration algorithms.

One example of where this type of imaging may occur is in space imaging of distant or small objects, as is the case in this research. Although there may be instances of image restoration in space imaging, including attempting to resolve binary star systems, this effort does not use these techniques.

In an optical system built for detection of space objects, the algorithm used to detect the objects is key. In this situation, the objective is to create a binary map of object locations from an image. A detection algorithm is used to determine if each pixel is one or zero depending on if an object is considered to be in that pixel or not. This map of the detected object is then used for further image processing techniques to determine additional information for cataloging objects. Such information may include orbit determination, size, and comparison against already known objects. As described earlier, these algorithms depend on knowledge of the distribution of the noise in the image. In these situations, the noise caused by the atmosphere can be accounted for by understanding the statistical fluctuations it causes.

This type of direct detection system can be useful in a situation where large amounts of data need to be processed. The image restoration methods described previously can be computationally expensive. In a large survey telescope like the SST, the required processing times are not feasible. In addition, the spreading caused by the atmosphere helps create distinct PSF shapes that can be used for match filter detection algorithms, which are discussed in Chapter 3. This research focuses on the analysis of the distribution of the received data to directly perform detection algorithms without AO or the image restoration techniques described above. There are several approaches for obtaining a noise distribution. These methods are described in the next section.

#### ***2.4.3 Statistical models for scintillation.***

There are three practical methods for developing a statistical model for the noise in the PSF. These methods are a theoretical based approach, simulation, and analysis of

measured data. Each of these methods present benefits and challenges. If the results derived from these methods agree, it increases confidence in the achieved result from any of the individual methods.

Determining a statistical model from theory is the most robust method for identifying the true distribution. This approach is independent of the telescope or imaging system used, and is therefore applicable in any optical system. One drawback is that due to its complicated nature, it may not be realistic to develop a closed form solution to this problem. Starting from the first principles of atmospheric theory is the most accurate way to build an improved detector. Several research efforts have attempted to determine distributions of received intensity through the atmosphere. These efforts have focused on both characterizing the statistics of the atmosphere [46–48] and the resulting PSF formed from an optical system viewing through the atmosphere [49, 50]. One generally accepted model of the intensity fluctuations due to the atmosphere is log-normal distribution. The log-normal is derived from theory developed by Tatarskii in [51, 52], and is experimentally verified in multiple physical experiments [53, 54]. The drawback to these methods is that they assume that the noise caused by the atmosphere is the only significant source, and therefore is the dominant source of noise in the image. This may be the case for certain intensity objects, atmospheric conditions, or exposure times. However, this assumption is not made in this research.

A second method for determining a statistical model is to collect and analyze a large amount of data to develop a model. This approach does not depend on deriving the fundamental properties of the atmosphere, but attempts to characterize it through its impact on measured data. The drawback of this method is that the results are dependent on a large number of data collections, and the analysis of those collections. There are several relevant examples of published research using this method. This observational method is used by Jee et. al. in [55], but the authors characterize spatial fluctuations in the PSF rather than

temporal. Additionally, this work focuses on the Advanced Camera for Surveys (ACS) which is installed on the Hubble Space Telescope (HST). This is a key difference between this research effort and [55]. Since HST is outside of the Earth's atmosphere, the PSF fluctuations are not caused by the atmosphere, but by other factors.

Another research effort that investigates the statistical and temporal properties of scintillation is completed by Dravins et. al. in [56]. In this paper, two statistical aspects of intensity fluctuations are investigated. The first uses a photon counter to determine a density function for the number of received photons. The second statistical aspect investigated is the autocorrelation. The autocorrelation provides insight into the behavior of the intensity fluctuations over time. Due to the nature of the data collection method described in this paper, the authors investigate short exposure times, in the sub-millisecond regime. It is shown that over a specified time separation, the correlation drops to a negligible amount. At this time separation, it can be assumed that the two images are independent. This fact could be used to characterize longer exposure times that might be utilized by the SST. To match the collected data to potential distribution fits, two methods may be used. The first method is to fit histograms of the received data to PDF and utilize an error metric like Root Mean Squared Error (RMSE). The second method is to investigate the statistical moments of the received data. With this method, the authors experimentally determine that a beta distribution of the second kind provides the closest match to the statistical moments under their assumptions. The authors have no physical motivation for choosing this distribution, only stating that it provides the closest match to the third and fourth order moments of the distributions tested.

A third approach to characterize the noise present is to utilize a simulation. The benefit of a simulation is that a large amount of data can be easily generated for little to no cost. This can solve some of the problems presented by the measured data method. A drawback to this method is that several limiting assumptions are made to make the simulation feasible.

In addition, both measured data and simulation depend on utilizing specific telescope parameters for several properties, including lens aberrations and telescope diameter to atmospheric seeing ratio. Performing a simulation relies on modeling two key components of the system: the atmosphere and the optical system. Building an optical model is straightforward and well understood. Only a few assumptions such as a Fraunhofer propagation can be used. Simulating light propagating through the atmosphere presents several challenges. The first is whether to represent the atmosphere as a single or multiple phase screen. Depending on assumptions of the viewing angle, either can be justifiable.

In this research, a single random phase screen is used, and its details are developed in Chapter 5. In addition, there are several proposed methods for creating random phase screens. They are a Fourier Transform-based phase screen described by Schmidt [57] and a Zernike polynomial based phase screen developed by Cain and Richmond [58]. Both of these methods use the underlying statistics developed in Kolmogorov theory [59, 60], but implement these statistics in different ways. In [61], Roddier et. al. show that the wavefront errors due to the atmosphere can be accurately represented with Zernike polynomials. Using the models described above, the simulated intensity can be observed as a function of both exposure time and seeing conditions. From this data, a statistical fit can be made to determine which distribution most closely matches the simulated results.

This dissertation will first theoretically derive the solution for the distribution of intensity fluctuations in a received PSF. To provide a validation of the theory, simulated space object data will be analyzed. They will provide solutions in the case where an analytic solution is not feasible. Chapter 3 will outline the development of an improved Multiple Hypothesis detection algorithm based on a Gaussian assumption of noise in the collected image.



### III. Improved Multiple Hypothesis Test through an Unequal Cost Assumption

In this Chapter a new detection algorithm that could be utilized in SDA telescopes is proposed. Section 3.1 presents an optical model for the SST system that is used in the algorithm. Section 3.2 describes the theory involved in developing the detection algorithm. Section 3.3 discusses the experimental setup used to collect data for this Chapter. Section 3.4 outlines results and data analysis. Section 3.5 discusses a method for full frame implementation of the detection algorithm. Section 3.6 discusses the conclusions made based on the presented results and potential future work.

#### 3.1 SST Optical Model

The image created by an optical system viewing a point source or spatial impulse is known as the PSF. The algorithm developed for this chapter requires a model for the expected PSF of the objects being investigated. The SST views space objects that are either relatively small and located in earth orbit, or very distant objects like stars and asteroids. Using geometric optics, the ratio of pixel size to focal length can be compared to the size of the object and distance from the SST. Using this relation, it is evident that all of these potential objects are effectively point sources to the telescope.

As described in Chapter 2, if the conditions are met, a Fourier Transform can be used to perform a field propagation. Goodman demonstrated that the PSF of an optical system,  $h_{\text{opt}}(x, y)$ , can be found by the following relation [34]:

$$h_{\text{opt}}(x, y) = |\mathcal{F}\{P(m, n)\}|^2 \quad (3.1)$$

where  $x, y$  are spatial distance pixel coordinates in the detector plane, and  $m, n$  are pixel coordinates in the pupil plane.  $P(m, n)$  is a pupil function that mathematically describes the effect of the pupil on incoming light, and  $\mathcal{F}$  is a two-dimensional Fourier transform. This

relation holds for a flat focal plane array, which the SST does not have. It is assumed that the SST does not have a focal plane array in this research effort. This implies there may be small errors in PSFs created off the optic axis. The creation of optimal PSF is not the focus of the research, and all algorithms tested use the same flat focal plane array assumption.

In a diffraction limited optical system consisting of a perfect lens or mirror, the pupil function consists of only the geometry of the pupil,  $P(m, n) = A(m, n)$ , and contains no other phase distortions.  $A(m, n)$  is an amplitude function that is one or zero, depending on if light is able to pass through the pupil at the  $m, n$  pixel location. In this optical model, the SST is assumed to have a 3.5m primary mirror and a 1.75m obscuration. The physical telescope has secondary mirror arms and other minor obstructions, but these objects do not have a significant impact on the produced image.

In a non-ideal imaging system, imperfections in the lenses or mirrors cause phase distortions to any light passing through the optics. These distortions are modeled as phase fluctuations to the pupil function [34]:

$$P(m, n) = A(m, n) \exp [j\theta_o(m, n)] \quad (3.2)$$

The phase aberrations  $\theta_o(m, n)$ , are expressed as the sum of a set of orthonormal Zernike polynomials, with each polynomial representing a type of phase distortion [62].

$$\theta_o(m, n) = \sum_k a_k Z_k(m, n) \quad (3.3)$$

The weighting coefficients  $a_k$  represent the amount of the  $k^{th}$  Zernike polynomial  $Z_k(m, n)$  present in the optics. These coefficients are unique to the imaging system being used. To create an accurate model of the PSF, the aberrations present in the telescope need to be experimentally measured. Finding the values for these coefficients can be difficult, especially in a three-mirror optical system, but Woods has described a method for obtaining the Zernike coefficients values [63]. Using this method, the SST program can

experimentally estimate the first 11 coefficients. These values can change over time, but average values are used in this research to simulate the aberrations in the system. Only the first 11 coefficients are used in this model for two reasons. The first reason is that a large portion of the power in the aberrations is contained in the lowest order polynomials. Secondly, the SST system is undersampled, and any high frequency distortions will not be observable in the sampled images. Table 3.1 shows the measured coefficients for the first 11 polynomials.

Table 3.1: Average measured optical aberration Zernike coefficients,  $a_j$  for the SST.

<b>Coefficient</b>	<b>Value (Waves)</b>	<b>Coefficient</b>	<b>Value (Waves)</b>
$a_1$	2.09	$a_7$	0.28
$a_2$	-5.95	$a_8$	-0.73
$a_3$	-5.30	$a_9$	0.36
$a_4$	6.89	$a_{10}$	-0.48
$a_5$	1.26	$a_{11}$	-0.16
$a_6$	-0.28		

The next important effect to model is the atmosphere. The atmosphere is well modeled as a random process to any light that travels through it. This results in a propagation path for the light that has varying indices of refraction in space and time. The difference in path lengths results in phase front distortions and the image is not formed correctly at the image plane. A telescope collects photons over a specified period of time known as the integration time,  $T$ . The random atmosphere acts differently as a function of the integration time used. It has been shown that over long integration times,  $T \gg 100\text{ms}$ , the telescope effectively averages the random atmosphere [17]. An expression for this average random atmosphere

or long exposure Optical Transfer Function (OTF),  $H_L$ , is derived in [17]. The OTF is the Fourier transform of the PSF, and represents the frequency response of the system to an impulse.

$$H_L(f_x, f_y) = \exp \left( -3.44 \left[ \frac{\bar{\lambda} z \sqrt{f_x^2 + f_y^2}}{r_0} \right]^{\frac{5}{3}} \right) \quad (3.4)$$

$f_x$  and  $f_y$  are spatial frequency variables at the image plane,  $\bar{\lambda}$  is the center wavelength of the telescope,  $z$  is the focal length, and  $r_0$  is the seeing parameter. The seeing parameter is a variable that characterizes the intensity of fluctuations in the atmosphere. A smaller  $r_0$  indicates stronger fluctuations, implying the atmosphere will have a larger effect on the telescope. Typical observed ranges for  $r_0$  at the SST site in the White Sands Missile Range are 5-15cm. Next, the Fourier Transform of the optical PSF and long exposure OTF are multiplied in the frequency domain to obtain the combined OTF. Then the inverse Fourier is performed to obtain the new PSF model,  $h(x, y)$ :

$$h(x, y) = \mathcal{F}^{-1} \left( \mathcal{F} [h_{\text{opt}}(x, y)] H_L(f_x, f_y) \right) \quad (3.5)$$

The model described up to this point is accurate, if the image presented to the detector is sampled completely. In order to sample completely, the system must sample the image greater than the Nyquist frequency,  $f_s$ . The Nyquist frequency is twice the cutoff frequency,  $f_c$ , of the system, and is the rate at which a system needs to be sampled to prevent any aliasing. The maximum frequency content possible, or the cutoff frequency, in an optical system is [34]:

$$f_c = \frac{d}{\bar{\lambda} z} \quad (3.6)$$

where  $z$  is the focal length of the system and  $d$  is the diameter of the aperture. Using the inverse relationship between sampling frequency and sample spacing, the necessary sample spacing  $\Delta_s$  is found by:

$$\Delta_s = \frac{1}{2f_c} \Rightarrow \Delta_s \leq \frac{\bar{\lambda}z}{2d} \quad (3.7)$$

If an optical system is not properly sampled, aliasing occurs and data is lost. A value of 500nm is used for  $\bar{\lambda}$  in this model because it is close to the center of the visible range and produces an integer ratio between actual pixel size and Nyquist sampling. Solving equation (3.7) with the system parameters of the SST, the required pixel spacing needed to accurately sample the intensity at the CCD array is  $\Delta_s = 0.25\mu\text{m}$ . For most data collections by the SST, the  $15\mu\text{m}$  pixels are grouped into 2x2 data bins, giving an effective pixel size of  $\Delta_t = 30\mu\text{m}$ . Since  $\Delta_t > \Delta_s$ , the SST is not sampled at Nyquist. This implies that a shift in where the image is formed at the CCD can potentially cause differently shaped PSFs. To be able to simulate this effect, shifting is performed at this point in the model, prior to adjustment for the aliasing caused by sampling. The effect of shifting before or after modeling the sampling effect is well-documented in [24]. The author demonstrates that shifting after sampling does not adequately represent the effects of sub-pixel location object changes. To shift the PSF,  $h(x, y)$ , two variables are introduced; a distance shift in the  $x$  direction,  $\alpha$ , and  $y$  direction,  $\omega$ . Since the PSF is created in a large zero padded matrix, utilizing a circular shift introduces no edge effects.

$$h_s(x, y) = h(x + \alpha, y + \omega) \quad (3.8)$$

After the shift is implemented, the difference between required and actual sampling is modeled with a blurring function. Assuming square CCD sensors, this blurring function is expressed as rectangles in the  $x$  and  $y$  dimensions with a width of  $\beta$ , the ratio of system

sampling vs. required Nyquist sampling. This more accurate model for the PSF,  $h_d(x, y)$ , is produced by convolving the optical PSF from equation (3.8) with the following equation:

$$h_d(x, y) = \sum_{x_1=1}^{N_x} \sum_{y_1=1}^{N_y} h_s(x_1, y_1) \text{rect}\left(\frac{\beta x - x_1}{\beta}\right) \text{rect}\left(\frac{\beta y - y_1}{\beta}\right) \quad (3.9)$$

$x_1$  and  $y_1$  are convolution variables and  $N_x$  and  $N_y$  are the total number of pixels in the  $x$  and  $y$  direction respectively, while  $h_d(x, y)$  represents the convolved and downsampling effects on the PSF of sampling at a frequency greater than Nyquist.

This PSF model is used for this simulation because it combines the lens aberrations with the actual sampling size for the system, further increasing the fidelity of the SST model. Finally, the new PSF is normalized to sum to one. This allows the PSF to be scaled to match a specified object intensity.

$$h_n(x, y) = \frac{h_d(x, y)}{\sum_{x=1}^{N_x} \sum_{y=1}^{N_y} h_d(x, y)} \quad (3.10)$$

$h_n(x, y)$  is the final modeled PSF used in this chapter. Depending on the  $\alpha$  and  $\omega$  shifts used, the values and distribution of  $h_n(x, y)$  will change. Next, the theory and motivations for the detection algorithm being developed is described.

## 3.2 Theory Development

In this section, an algorithm is developed for a Multiple Hypothesis Test (MHT). There are several benefits to using a MHT, along with a strong physical motivation. Using a MHT algorithm presents unique computations, which are addressed in this section.

### 3.2.1 Motivation and Selection of Alternate Hypotheses.

In a MHT,  $M$  different potential hypotheses are considered. Each hypothesis corresponds to a particular set of input conditions. In this case, each input condition represents a modeled PSF viewed through the SST system. As described in section 3.1, sub-pixel shifts of an object's location on the CCD array will change not just the position,

but the shape of the resulting image. This effect due to aliasing will cause the PSF to have different shapes depending on the location of the object at the CCD [24]. The goal of using a MHT is to utilize several different potential PSF distributions to achieve a higher probability of detection for an object that may be located in one of the sub-pixel locations. Table 3.2 shows a list of potential hypotheses used in this model.

Table 3.2: List of hypotheses considered and a description of object location at the CCD.

Hypothesis	Description
$H_0$	No Object Present
$H_1$	$\alpha_1, \omega_1$ Shifts
$H_2$	$\alpha_2, \omega_2$ Shifts
$\dots$	$\dots$
$H_{M-1}$	$\alpha_{M-1}, \omega_{M-1}$ Shifts

By picking  $\alpha$  and  $\omega$  to be specific sets of spatial shifts in  $x$  and  $y$ , a model for objects located in the corners, center, and sides of a pixel can be developed. Choosing the number of hypotheses and their position location is an important decision. As described in Chapter 2, only two hypotheses are currently used by the SST program. These two hypotheses are that the object is present or not present. Through a Likelihood Ratio Test (LRT), the test is reduced to examining individual pixels and determining their SNR. If a space object is located in the corner of a pixel, photons may spread into adjacent pixels, and the peak intensity of the pixel of interest is lowered. This effect lowers the SNR value of the pixel being tested, decreasing the probability of detecting that object. To mitigate this effect, correlation algorithms are proposed to compare not just a single pixel, but the entire expected PSF [35]. This concept is expanded to include multiple alternative hypotheses

consisting of shifted aliased PSFs that are used as potential alternative hypotheses [24]. Figure 3.1 shows a graphical representation of an object formed on a single pixel with three different  $M$  values, along with the true object location. The small dot indicates the true location of the object, and the lines indicate the separation of the pixel into its decision space areas.

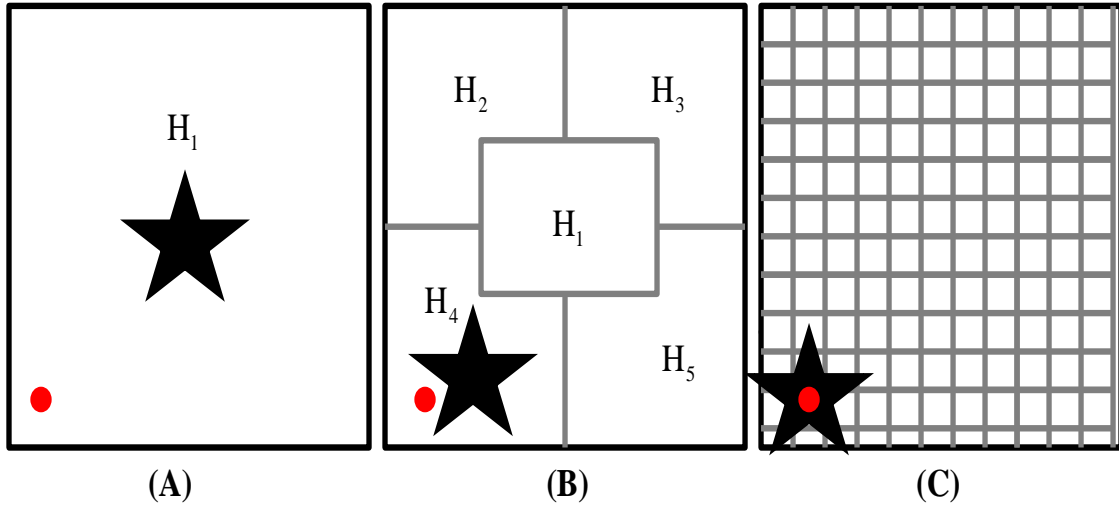


Figure 3.1: A graphical example of the division of a pixel into sub-pixel location for varying  $M$  where the star in each figure represents the modeled location of the object and the dot is the true location. (A) Simple Binary test,  $M = 2$  (B) Multiple hypothesis test with  $M = 6$ , with sub-pixel hypotheses at the four corners and center of the pixel (C) A highly sampled pixel space with  $M = 121$  hypotheses.

A BHT is illustrated in (A). In this case, the object is assumed to be in the center of the pixel. Given that the object is actually located in the bottom left corner, the point detector or correlation BHT might not adequately capture the resulting PSF. This can manifest as a lower probability of detection. In (B), a MHT where  $M = 6$  hypotheses is illustrated. In this case, a PSF is created that would model an object in the bottom corner



adequately. This algorithm would likely have a greater probability of detection due to the strong correlation between the modeled and observed PSF. Finally in (C), a densely sampled pixel is illustrated. Similarly to (B), this choice of  $M$  would produce a PSF that would likely correlate well with the observed PSF. The small change in sub-pixel locations used in (B) and (C) would not present a noticeable change in the PSF.

At a certain point, the addition of an increasing number of hypotheses introduces error into the decision criteria. Since the PSFs are created through simulation, many resulting shapes and intensity distributions can be created. For a large number of  $M$ , the alternate hypotheses may have a higher chance of resembling random noise present in the system. This effect can potentially increase the false alarm rate of the detector, demonstrating the trade-off between the number of hypotheses and the detection capability. In addition, the creation and hypothesis testing of the additional hypotheses presents additional computation cost.

Theoretically,  $M$  can be increased to infinity, creating a continuously sampled space. This result would lead to an estimation instead of a detection approach. Following this logic, an alternative approach to the MHT presented in this section could be implemented. In this method, an estimate is found for the sub-pixel location of a potential object at every pixel. Then a model of the PSF due to an object at that location is created, and a BHT is performed based on that estimate. This BHT could resemble the currently used SST algorithm. This method would result in performing an additional estimation algorithm at every pixel location in addition to the detection algorithm, which is a significant drawback.

Another drawback with an estimation of the location approach is that the user might not be interested in the sub-pixel location, and only want to use that information to increase the detection performance. In an estimation problem, the sub-pixel location would be considered a nuisance parameter. There are methods of performing estimation without estimating nuisance parameters, described by Kay [64], but they are utilized when the end

goal of the problem is to estimate information about a signal. The space object detection algorithm described here could utilize estimation for nuisance parameters, but is still a detection problem at the core, meaning the end goal of the user is to determine if an object is present or not.

An additional reason that this problem is framed as a MHT is that it allows for a very specific set of choices for sub-pixel locations. This set is selected as the most likely to occur, and will have the largest impact on the intensity and shape of the resulting PSF. The MHT can be tailored to a specific optical system and mission requirements. In the next section, the theory involved with creating and implementing a MHT algorithm is described.

### 3.2.2 *Detection Algorithm Based on Bayes Risk.*

In this algorithm,  $M$  different sub-pixel locations are considered. In both [25, 65] a Bayes criterion is shown for a multiple hypothesis test, including methods for reducing the test to a usable form. A Bayes risk hypothesis test details how to select the hypothesis that results in the minimal risk,  $\mathcal{R}$ , on average. The hypothesis that results in the smallest risk is the most likely to match the true hypothesis.

$$\mathcal{R} = \sum_{i=0}^{M-1} \sum_{k=0}^{M-1} \pi_k C_{ik} \int_{Z_i} p(\mathbf{D}|H_k) d\mathbf{D} \quad (3.11)$$

In the risk expression,  $\pi_k$  is the a priori probability for the  $k^{th}$  hypothesis, or how likely it is to occur.  $C_{ik}$  is the cost associated with choosing the  $i^{th}$  hypothesis when the  $k^{th}$  hypothesis has occurred. The cost is a number between zero and one that indicates how big of an error is made, with zero being no error and one being the most significant type of error. The conditional PDF of the received data given  $H_k$  occurred is  $p(\mathbf{D}|H_k)$ .  $Z_k$  is observation space for the  $k^{th}$  hypothesis.

To reduce this expression into a form that can be implemented, the null hypothesis space  $Z_0$  is separated into its non-overlapping regions  $Z_0 = Z - Z_1 - \dots - Z_{M-1}$ . Next,

noting that integrals over the entire decision space  $Z$  equal one, and grouping similar terms of  $Z_k$  gives the following relation:

$$\mathcal{R} = \sum_k^{M-1} \pi_k C_{kk} + \sum_i^{M-1} \int_{Z_i} \sum_{\substack{k=0 \\ k \neq i}}^{M-1} \pi_k (C_{ik} - C_{kk}) p(\mathbf{D}|H_k) d\mathbf{D}. \quad (3.12)$$

The first summation term in equation (3.12) is a constant risk, implying that it is independent of the choice of region  $i$ , and can be excluded from the decision criteria. The cost for selecting a correct hypothesis,  $C_{kk}$ , is assumed to have no associated risk and is defined to be zero. The minimum Bayes risk is then found by choosing the region  $i$  that results in the smallest risk  $\mathcal{R}$ . The  $i$  that results in the minimum risk is the hypothesis  $H_i$  which minimizes Bayes risk. Determining this region  $i$  is implemented by selecting the integrand over  $Z_i$  with the smallest value. This results in the following decision criteria:

$$H_i = \min_{i \in 0:M-1} \left( \sum_{\substack{k=0 \\ k \neq i}}^{M-1} \pi_k C_{ik} p(\mathbf{D}|H_k) \right) \quad (3.13)$$

By using equation (3.13) directly, a detection algorithm can be implemented. If  $H_0$  produces the minimum risk value, then the algorithm says no object is present. On the other hand, if any other hypothesis produces the minimum risk, it is decided that an object is present at the sub-pixel location hypothesis providing the minimum risk value. This MHT can be reduced further through specific choices for costs and priors, or implemented directly. If it is implemented directly, the MHT is flexible, because any combination of distributions for  $p(\mathbf{D}|H_k)$ , costs, or priors can be used without changing the basic structure of the algorithm. A drawback of this method is that finding the smallest hypothesis requires non-linear functions and is computationally complex. In this research effort, both a direct implementation and a reduced algorithm based on specific choices are investigated. To further reduce the MHT from equation (3.13), a few additional details are needed, including

a model for the conditional probabilities  $p(\mathbf{D}|H_k)$ , and a structure for the prior probabilities  $\pi_k$  and costs  $C_{ik}$ . These factors are investigated in the next sections.

### 3.2.3 *Model for Received Data Given Hypothesis $H_k$ .*

An important component for a hypothesis test is having a model for the received data. It is well-known that photon arrival times of light is a Poisson process [17]. Photon arrival times are not the only source of noise present in the SST system. The CCD can introduce several different sources of error, including dark current and spatial non-uniformity across pixels [58, 66]. Under the  $H_0$  hypothesis, when no object is present, the measured data contains only low intensity background light and noise from the CCD. Since the received data is dominated by CCD noise, it is assumed to be Gaussian. In the other  $M-1$  hypotheses, there is considered to be an object present, and therefore Poisson noise will contribute more significantly towards the overall noise level. Despite the additional Poisson noise, it is assumed that the Gaussian noise sources still dominate in these alternate hypotheses. As a result, the received data given these hypotheses is also considered to be Gaussian. As described in Chapter 2, several research efforts have investigated potential alternate PDFs for these hypotheses [22, 35]. Making these stated assumptions, the conditional PDF for a single pixel of received data given  $H_k$  is expressed as:

$$P(D|H_k) = \frac{1}{\sqrt{2\pi}\sigma} \exp\left(-\frac{(D-I)^2}{2\sigma^2}\right) \quad (3.14)$$

$I$  is the expected mean of the received data. If no object is present,  $H_0$ , the expected mean is only the background photons observed,  $I = B$ . In the other hypotheses,  $I$  is the object intensity  $\theta$  plus the constant background,  $I = \theta + B$ . In both cases,  $\sigma$  is the standard deviation of the received data. Assuming each pixel in the image is independent, the joint conditional probability of received image data  $\mathbf{D}$  given the  $k^{th}$  hypothesis is:

$$P(\mathbf{D}|H_k) = \left(2\pi\sigma^2\right)^{-\frac{N_x N_y}{2}} \exp\left(-\sum_{x=1}^{N_x} \sum_{y=1}^{N_y} \frac{(D(x,y) - I(x,y))^2}{2\sigma^2}\right) \quad (3.15)$$

In this case,  $I(x, y) = B$  for  $H_0$  and  $I(x, y) = \theta h_n^k(x, y) + B$  for  $H_k$ . Additionally,  $h_n^k(x, y)$  is the normalized model for the PSF of the  $k^{th}$  hypothesis.

### 3.2.4 Selecting a Cost Structure.

To implement the MHT, it is necessary to choose values for the costs,  $C_{ik}$ , and priors,  $\pi_k$ . Often if there is not strong evidence otherwise, an equal cost and uniform prior probability scheme is chosen. This cost scheme, a Equal-Cost Equal-Prior (ECEP) assignment, weighs all errors with the same amount of cost. For example, a false alarm has the same cost as an error in sub-pixel detection and a missed detection. It also assumes that all hypotheses occur with the same probability.

$$C_{ik} = \begin{cases} 0, & i = k \\ 1, & i \neq k \end{cases}, \quad \pi_k = \frac{1}{M} \quad (3.16)$$

In certain situations, this cost structure accurately represents the true state of the system. In a SDA environment, it is much more probable that there is no object present,  $H_0$ , than having an object present,  $H_{k \in 1:M-1}$  due to the relatively small number of detectable objects in a large search volume. As described in Chapter 2, a detection algorithm utilizing uniform priors and equal costs is implemented [24]. One reason for its use is its ability to reduce the algorithm to a sufficient statistic or SNR test. Using SNR is a common practice in other SDA efforts [21]. This approach gives the author the ability to directly compare detection algorithm performance to the point detector used by the SST. Using these equal cost and prior assumptions equation (3.13) reduces to the following LRT comparison:

$$\mathcal{L}_e = \max_{k \in 1:M-1} \left( \underbrace{\sum_{x=1}^{N_x} \sum_{y=1}^{N_y} \frac{D(x, y) - \hat{B} \left( \frac{h_n^k(x, y)}{\sigma_k} \right)}{\sigma}}_{\text{SNR}_k} \right) \underset{H_0}{\overset{H_k}{\geq}} \Gamma_{M\text{-ary}} \quad (3.17)$$

$\hat{B}$  is the estimated background intensity and is found by determining the median value of all the pixels in the 15x15 window.  $\sigma$  is the standard deviation of the received data. To calculate  $\sigma$ , the standard deviation of the 15x15 window is found. Next, the outliers with intensity more than 3 standard deviations above the estimated background are removed. A new  $\sigma$  is calculated with these outliers removed. More details about this process are described in Section 3.4.  $\sigma_k$  is a normalizing factor that is included to ensure that  $\mathcal{L}_e$  has the same standard deviation as the original point detector. The value for  $\sigma_k$  is found by summing the squared PSF of the  $k^{\text{th}}$  hypothesis. The SNR for each hypothesis  $k$  is computed, and the maximum SNR is compared to a threshold  $\Gamma_{\text{M-ary}}$ .

Alternatively, this model implements a cost scheme with Unequal-Cost Equal-Prior (UCEP) assumptions, where errors of different types are weighted differently. A third type of error besides false alarm and missed detection is introduced. This third error occurs when an object is detected, but is misclassified as having the incorrect sub-pixel location. There is no cost associated with this “mixed-detection” event. This cost is useful in a situation where the detection of the object is more highly valued than a precise location, as is the situation for the SST. For example, in the SST program, the detection results feed into other data processing steps that perform clustering and locating. Missed detections and false alarms are still considered to have a cost of one. To compare to previous algorithms, an equal prior probability for  $\pi_k$  assumption is made for this MHT.

$$C_{ik} = \begin{cases} 0, & i = k \\ 0, & i \neq k \cap (i \cap k \neq 0) \\ 1, & i \neq k \cap (i \cup k = 0) \end{cases}, \pi_k = \frac{1}{M} \quad (3.18)$$

Implementing the costs from equation (3.18) into the Bayes risk from equation (3.13) and reducing gives the following detection criteria:

$$\mathcal{L}_u = \log \left( \sum_{k=1}^{M-1} \frac{p(\mathbf{D}|H_k)}{p(\mathbf{D}|H_0)} \right) \underset{H_0}{\overset{H_1}{\geq}} 0 \quad (3.19)$$

Using the assumed Gaussian distributions described in equation (3.15) for  $p(\mathbf{D}|H_k)$ , the ratio of conditional densities can be reduced. Combining the exponentials and canceling like terms gives the following relation for  $\mathcal{L}_u$ :

$$\mathcal{L}_u = \log \left( \sum_{k=1}^{M-1} \exp \left[ - \sum_{x=1}^{N_x} \sum_{y=1}^{N_y} \frac{\theta_k h_n^k(x, y)}{\sigma^2} \times \left( \hat{B} - D(x, y) + \frac{\theta_k h_n^k(x, y)}{2} \right) \right] \right) \underset{H_0}{\overset{H_1}{\geq}} \Gamma_u \quad (3.20)$$

Unlike an equal cost approach, this MHT does not simplify to a SNR calculation due to the summation of all of the potential alternate hypotheses which are exponentials. This demonstrates both how additional information is being used to make the detection decision, and how the cost structure reduces the test to a decision between only  $H_1$  and  $H_0$ . This implies that no sub-pixel information is inferred from this test. Another distinguishing factor between an equal and unequal cost approach is that the intensity of the object  $\theta_k$  is now needed to determine  $\mathcal{L}_u$ . The intensity  $\theta_k$  is the object intensity used in the current MHT method presented in [24]. There are different intensities for each hypothesis because the shifting results in more or less spreading of the PSF, causing intensity changes. In the previous equal cost MHT algorithm,  $\theta$  is not defined directly, but is chosen by the selection of a threshold  $\Gamma_{\text{M-ary}}$  since  $\theta$  is included in the threshold.

$$\theta_k = 2\Gamma_{\text{M-ary}} \frac{\sqrt{\sum_{x=1}^{N_x} \sum_{y=1}^{N_y} h_n^k(x, y)^2}}{\sum_{x=1}^{N_x} \sum_{y=1}^{N_y} h_n^k(x, y)^2} \quad (3.21)$$

The algorithm presented in equation (3.20) is a reduced form of the decision criteria shown in equation (3.13), but is specific to a set of costs. To evaluate the performance of equal and unequal costs in the detection of objects, the non-reduced equal cost approach presented in (3.13) is compared to the reduced unequal cost algorithm derived in (3.20).

There are benefits and drawbacks to using both the ECEP and UCEP algorithms. Using the previously developed equal cost algorithm shown in equation (3.17) gives both detection capability and sub-pixel location information. The largest hypothesis SNR is compared to the threshold, and if an object exceeds that threshold it is considered to be in that sub-pixel location. The additional position information can be useful in improving object tracking. A drawback of this algorithm is that each SNR calculation is only based on one PSF model. Each of the  $M$  hypotheses are correlated against the received data,  $\mathbf{D}$ , and are used to choose the maximum. This equal cost method of detection is a series of binary hypothesis tests fused together. The alternative ECEP algorithm presented with this research is a direct implementation of equation (3.13), resulting in similar benefits to the previously developed approach. The benefit to the new implementation is that it is flexible in its ability to change the prior probabilities or costs if desired.

In contrast to the ECEP, the UCEP algorithm consists of a combination of all potential hypotheses for the selection of  $k$ . This implies the data from each hypothesis is combined to make a single decision. A drawback of the unequal cost detection algorithm from equation (3.20) is that it is unable to be reduced to a sufficient statistic such as SNR. As a result, there are additional computation complexities which may limit performance or implementation operationally.

A significant difference with this new approach is the space in which decisions are made. Previous work has reduced the hypothesis test to a sufficient statistic, namely SNR. Using the SNR, it is more straightforward to determine the probability of detection. On the other hand, using an UCEP algorithm (3.20) gives a complicated relationship between  $M$  hypotheses in risk space. As part of this effort, a method to determine  $P_d$ ,  $P_f$ , and create ROC curves in risk space is developed. These derivations are included in section 3.4. Next, the experiment used to collect data is described.



### 3.3 Experiment Description

To measure the performance of the detection algorithms, data collected from the SST system is analyzed. In operational use, the telescope will observe varying intensity objects. To demonstrate that a new detection algorithm performs better than the currently implemented BHT, objects of high, intermediate, and low intensity need to be investigated. An improvement in detection of any of these types of objects will enhance the overall capabilities of the SST system.

One approach to test the MHT would be to find a variety of known and cataloged space objects of varying intensity, and image these objects with the SST. It may be difficult to find enough objects of particular intensity without a large search. It could also require a long period of search, or multiple nights to capture these objects. During that time, important parameters may change, including the seeing  $r_0$  or optical aberrations in the telescope. Instead, this research uses a data set of the SST observing the Geosynchronous Earth Orbit (GEO) communications satellite ANIK-F1 as it enters into an eclipse. The SST is programmed to track the orbital elements of the satellite as it enters an eclipse caused by the earth. Collecting images in this manner causes the satellite to change intensity as a function of time, transitioning from bright to dim. Collecting images of this event reduces the requirement of searching several areas of sky and locating objects of specific magnitudes.

The data set described here was originally collected to observe the performance of another detection algorithm presented in [24]. The result of this observation is a set of data including a space object that transitions from easily detectable to very difficult to detect over the course of a few minutes, or a few hundred images. This experiment was conducted during the vernal equinox in 2012 and was repeated over several nights from 28 Feb 2012 to 23 Mar 2012.

### ***3.3.1 Locating and Selecting False Alarm Data.***

To completely compare a set of algorithms, the detection performance should be noted for different false alarm rates.  $P_f$  is the probability that when the algorithm is presented with data containing no object, it indicates that an object is present. To find a value for  $P_f$ , captured data containing no object is needed. There are two potential methods to create data with no object present.

One method is to generate independent Poisson random variables at each pixel with a mean of the background intensity. This simulated data would give an approximation of actual data that might be observed by the SST when no object is present. Alternatively, this research uses collected SST data to be as realistic as possible. Due to the potential for dim objects at any point, it can be difficult to determine if there is truly an object such as a star in any subset of data. There may be an object present, but barely above the noise floor and not noticeable to the human eye. To ensure a set of data is used with no object, a patch of sky is collected and averaged over multiple frames. Since the SST system is tracking a satellite in GEO, most of the objects not in GEO will move at the sidereal rate. This rate translates to 8 pixels of motion per frame or greater.

To generate a set of false alarm data, a 15x15 pixel patch of observed sky is tracked through 60 consecutive frames. The 60 frames are then averaged to give a longer effective integration time. If there were a dim celestial object consistently present in this portion of sky, it would become more intense as the noise is reduced through the averaging process. Through several trials, a portion of sky is found and documented with no pixel outside of 3 standard deviations of the mean in this averaged data set. This implies that there is a high likelihood that all of the fluctuations are due to noise, and no object is present in the data set. This data set is then used to calculate an upper bound of the false alarm rates used in the results.

### 3.4 Results and Analysis

Each image collected by SST consists of 6144x4096 pixels that are 2x2 binned. To perform the detection algorithm in a tractable amount of time, a small subset of the image around the satellite of 15x15 pixels is extracted from each frame. This allows for the algorithm to quickly process a MHT on the center pixel, but still includes enough pixels to capture the entire PSF and a sufficient amount of background pixels to calculate accurate background statistics. In operational use, this 15x15 window surrounding the pixel of interest would slide through the image as each new pixel is tested. For this analysis, the window surrounding the center pixel of ANIK-F1's PSF is investigated in each frame.

Another important factor of the data analysis is outlier removal. Within each 15x15 window there may be objects in addition to the object of interest. These “nuisance objects” are detrimental to the test being performed on the center pixel. When the background,  $\hat{B}$ , is estimated by finding the median, the nuisance objects inflate the value of the background statistics, making the object of interest seem more dim relative to the background. This effect causes a decrease in detection performance.

These objects are removed in a two-step process similar to the method described in [24]. First, the background and variance is estimated for the entire 15x15 window. Next, the individual pixels are compared against the estimated background. Any pixels that are 3 standard deviations or greater than the background are removed. This does not include the PSF of the object of interest. Finally, the standard deviation is calculated.

#### 3.4.1 Detection and False Alarm Computations.

As mentioned in section 3.2.4, a unique method of computing  $P_d$  and  $P_f$  is proposed in this section. Looking at equation (3.13), there are two important cases in determining detections and false alarms. These cases are the value of the algorithm when  $H_0$  is chosen,  $\eta$ , and the minimum value of the rest of the  $M-1$  other hypothesis,  $\phi$ . To give a similar comparison to the UCEP algorithm, the logarithm is taken of both cases to move the

variables into a log space. The data being processed,  $\mathbf{D}$ , is contained in the exponential function. As a result it is common in detection and estimation to make decisions in log space. The expression for these random variables are defined by the two expressions below:

$$\eta_g = \log \left( \sum_{k=1}^{M-1} \pi_k C_{0k} p(\mathbf{D}|H_k) \right). \quad (3.22)$$

$$\phi_p = \log \left[ \min_{i \in 1:M-1} \left( \sum_{\substack{k=0 \\ k \neq i}}^{M-1} \pi_k C_{ik} p(\mathbf{D}|H_k) \right) \right] \quad (3.23)$$

The subscript  $p$  signifies which case the variables were generated under. These random variables are generated by two different conditions. The first condition  $p = 1$  is when an object is present in the data. In this case,  $\mathbf{D}$  equals the 15x15 frame of data surrounding ANIK-F1. This data is used to generate the probability of detection. The sub-pixel location can also be determined by noting which  $i$  provides the minimum from equation (3.23). The accuracy or benefits of using this estimate for the sub-pixel location of the object is not investigated in this research. The second condition,  $p = 0$ , is when image data containing no objects, as described in section 3.3.1, is used for  $\mathbf{D}$ . Processing this data gives the false alarm rate of the test. To create a single frame detection from this MHT, the two variables can be compared with the following relation:

$$\eta_p \underset{H_0}{\overset{H_1}{\geq}} \phi_p + \tau \quad (3.24)$$

If  $\phi_p$  is less than  $\eta_p$ , an object is considered to be present; if the opposite is true, no object is present. The threshold  $\tau$  can be changed to allow the user to achieve a desired  $P_f$ . Implementing equation (3.24) would yield one instance of a detection decision for a single frame. This value may not be representative of how often that outcome occurs. Instead, a sequence of frames are used to generate a probability of detection,  $P_d$ , at that particular

intensity. Finding the probability of detection relies on knowledge of the distribution of the variables  $\phi_p$  and  $\eta_p$ .

As described in section 3.2.3, the conditional probabilities  $p(\mathbf{D}|H_k)$  are assumed to be Gaussian. Investigating the values of the variables over the collected data shows that the random variables appear to follow a Gaussian distribution. To verify this, a sliding window of 15 frames is used to compute the statistics for  $\eta$  and  $\phi$ . An interesting trade-off exists due to the object continuously losing intensity. Ideally, to ensure the best fit for statistics, a large window would be used. This would allow high confidence in both the Gaussian distribution assumption and the calculated mean and standard deviations of the data. A drawback of using too large of a window is that the intensity of the satellite decreases too much between the beginning and the end of window. This results in data that appears Gaussian, but has a non-constant mean. In this case, the mean value of  $\eta_p$  and  $\phi_p$  is a function of the frame number, or object intensity. To avoid this, a sliding window of 15 frames is used. This window was large enough to generate accurate statistics, but not long enough to cause the intensity of ANIK-F1 to change significantly. Making this assumption, the mean and variance statistics can describe the behavior of both  $\eta_p$  and  $\phi_p$ . Figure 3.2 shows a plot of  $\eta_p$  and  $\phi_p$  values when  $p = 1$  over a 15 frame window.

For the case shown in Figure 3.2, the value for  $\phi_1$  is always less than the value of  $\eta_1$ . If a single point detection decision is used, a detection would be made at every point, assuming a threshold value of  $\tau = 1$ . Designating a value of 1 for a detection or 0 for no detection at each frame could give one instance of the detection capability of the algorithm. Using a single point approach as described may not represent the typical or average detection performance given slightly different noise or other fluctuations. Instead, the means  $\mu_\phi$  and  $\mu_\eta$ , and standard deviations  $\sigma_\phi$  and  $\sigma_\eta$  are used to determine how probable a detection is in general. To generalize the decision rule in equation (3.24) to more than one instance, the probability of detection or false alarm  $\mathcal{P}_e$  is created.  $\mathcal{P}_e$  represents the

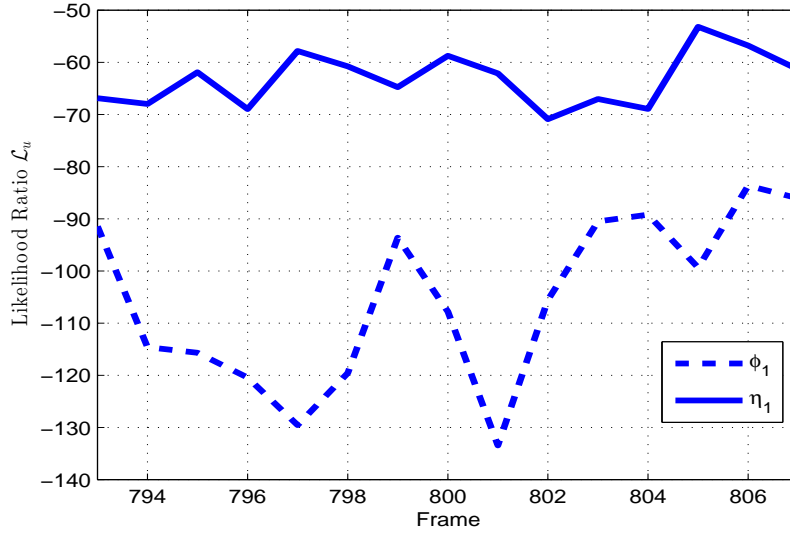


Figure 3.2: Equal cost algorithm variables with an object present,  $\eta_1$  and  $\phi_1$ . These variables are observed over a 15-frame window, and the means and standard deviations are used to determine  $P_d$  at frame 800. This data was collected on 13 Mar 2012.

probability that the random variable  $\phi_p$  is less than the random variable  $\eta_p$ . In general, the probability that one random variable is greater than another is not directly computable, so instead an intermediate conditional probability for a given  $\eta_p$  is calculated.

$$\mathcal{P}_e(\eta_p) = p_\phi(\phi_p < \eta_p | \eta_p) = \int_{-\infty}^{\eta_p} p_\phi(\phi_p) d\phi_p \equiv F_\phi(\eta_p) \quad (3.25)$$

The conditional probability  $p_\phi(\phi_p < \eta_p | \eta_p)$  causes the overall probability  $\mathcal{P}_e$  to become a function of  $\eta_k$ . The probability that a random variable is any value below a threshold is defined as a Cumulative Distribution Function (CDF). The CDF  $F_\phi(\eta_p)$  is calculated by integrating the PDF for  $\phi$ ,  $p(\phi_p)$ , from  $-\infty$  to the threshold  $\eta_p$ . Evaluating  $F_\phi(\eta_p)$  gives the probability of detection or false alarm for a single given value of  $\eta_p$ . To determine  $\mathcal{P}_e$  not as a function of  $\eta_p$ , Bayes Theorem is utilized, and the distribution is integrated over all possible values of  $\eta_p$ .

$$\mathcal{P}_e = \int_{-\infty}^{\infty} p_{\phi}(\phi_p < \eta_p | \eta_p) p_{\eta}(\eta_p) d\eta_p = \int_{-\infty}^{\infty} \underbrace{\left( \int_{-\infty}^{\eta_p} p_{\phi}(\phi_p) d\phi_p \right)}_{F_{\phi}(\eta_p)} p_{\eta}(\eta_p) d\eta_p \quad (3.26)$$

$p_{\eta}(\eta_p)$  is the PDF for the random variable  $\eta$  evaluated at  $\eta_p$ . At this point an analytical solution for  $\mathcal{P}_e$  is not easily determined. To calculate  $\mathcal{P}_e$ , the integral over  $\eta_p$  is solved numerically using a Riemann sum.

$$\mathcal{P}_e = \sum_{\eta_p} F_{\phi}(\eta_p) p_{\eta}(\eta_p) \Delta\eta_p \quad (3.27)$$

To analytically solve the integral, a finite range of  $\eta_p$  values are needed.  $\eta_p$  is varied from -200 to 200 with  $\Delta\eta_p = 1$ . The range of  $\eta_p$  is selected to be large enough to cover potential function values. A similar approach is used to determine  $P_d$  and  $P_f$  for the unequal costs algorithm  $\mathcal{L}_u$  in equation (3.20). One significant difference is that there are no longer two random variables to compare. Instead there is one random variable and a constant threshold. As a result, the probabilities  $\mathcal{P}_u$  can be calculated by comparing  $\mathcal{L}_u$  to a fixed threshold  $\Gamma_u$ . Figure 3.3 is a plot of the value of  $\mathcal{L}_u$  calculated as a function of frame number. The value for  $\mathcal{L}_u$  for this window is always above the threshold, assuming  $\Gamma = 0$ .

The statistics of a sliding 15 frame window are calculated for the mean  $\mu_{\mathcal{L}}$  and standard deviation  $\sigma_{\mathcal{L}}$ .  $\mathcal{P}_u$  is then found. The probability of false alarm or detection is defined as the probability that the random variable  $\mathcal{L}_u$  is greater than the threshold  $\Gamma_u$ .

$$\begin{aligned} \mathcal{P}_u = p_{\mathcal{L}_u}(\mathcal{L}_u > \Gamma_u) &= \int_{\Gamma_u}^{\infty} p_{\mathcal{L}_u}(\mathcal{L}_u) d\mathcal{L}_u \\ \mathcal{P}_u &= 1 - F_{\mathcal{L}_u}(\Gamma_u) \end{aligned} \quad (3.28)$$

Utilizing the fact that the PDF integrates to one over its entire probability space, the probability  $\mathcal{P}_u$  can be found by subtracting the CDF of  $\mathcal{L}_u$  from one. Up until this point,

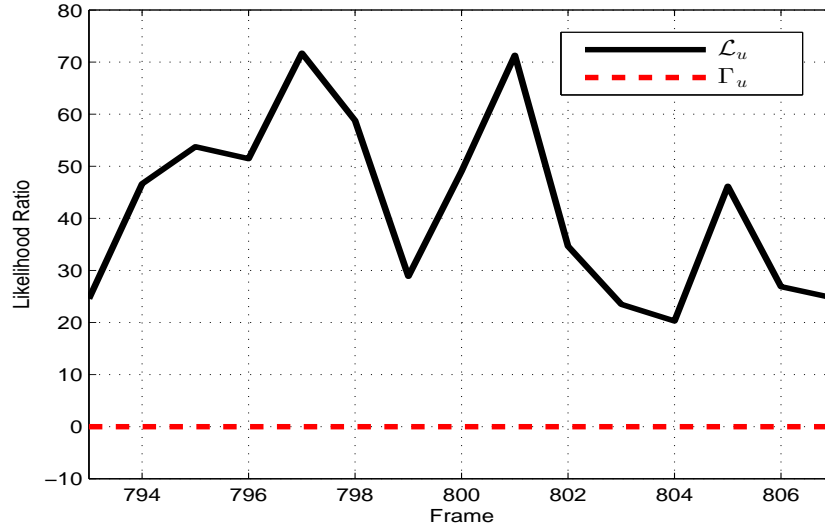


Figure 3.3: Unequal algorithm  $\mathcal{L}_u$  for a 15 frame window centered at 800 for 13 Mar 2012. The mean and standard deviation are calculated to give the probability of detection or false alarm  $\mathcal{P}_u$ .

the probabilities  $\mathcal{P}_e$  and  $\mathcal{P}_u$  have been left generalized. The benefit is that the calculations for  $P_d$  and  $P_f$  are very similar and only the input conditions are varied. Since  $P_d$  is the probability of choosing  $\phi$  when  $\phi$  is true, and  $P_f$  is the probability of choosing  $\phi$  when  $\eta$  is true, the expression for  $\mathcal{P}_e$  and  $\mathcal{P}_u$  can be used for both detection and false alarm probabilities. By varying  $p$ , or whether an object is present or not, both probabilities can be calculated.

$$\mathcal{P}_{e,u} = \begin{cases} P_d, & p = 1 \\ P_f, & p = 0 \end{cases} \quad (3.29)$$

Using equations (3.27) and (3.28), values of  $P_d$  and  $P_f$  based on the algorithms described in section 3.2.4 are calculated from the collected data. The first result investigated is the probability of detection at the false alarm rate currently used by the SST system. The first step is to verify the results against previous methods. After this has been verified,



conclusions can be made about any changes or improvements. This comparison is between an equal cost MHT approach originally presented in [24], an unequal cost MHT, and the currently used binary point detector. Using an equal cost MHT but calculating  $P_d$  differently and achieving similar results for a given false alarm rate with the same collected data would verify this new method.

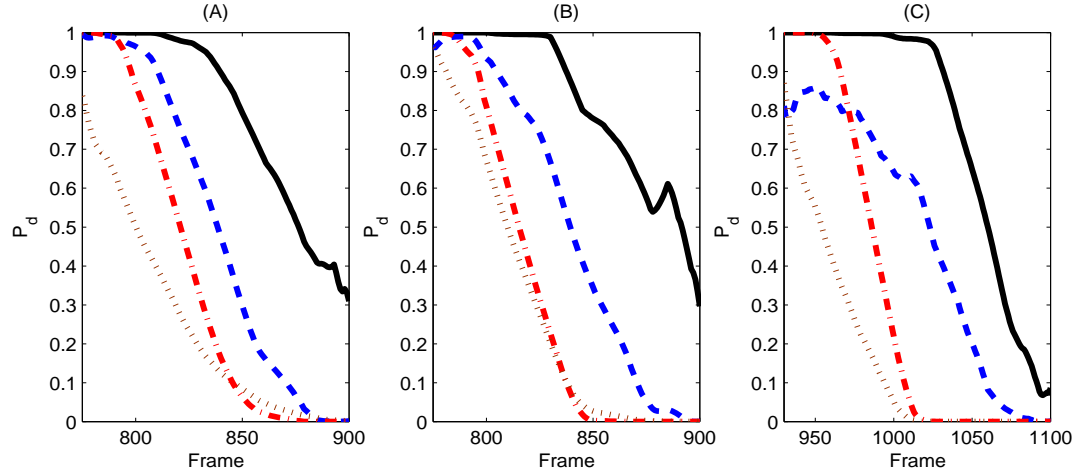


Figure 3.4:  $P_d$  curves for ANIK-F1 as it enters eclipse on 3 consecutive nights (A) 13 Mar 2012 (B) 14 Mar 2012 (C) 15 Mar 2012. The solid black line is the UCEP algorithm, the blue dashed line is the ECEP algorithm, the red dotted and dashed line is a binary matched filter, and the brown dotted line is a point detector. These detection curves are generated with  $P_f = 4.56e - 10$  and  $M = 10$ .

Figure 3.4 shows the probability of detection curves for data collected from the SST on three consecutive nights. The first night (A) was collected 13 Mar 2012. The UCEP algorithm outperforms the ECEP algorithm across all of the frames, with a difference range of 10-60 percent depending on the frame number. The UCEP algorithm also shows increases of 40-90 percent over the currently implemented point detector. Both the ECEP and UCEP algorithms start close to  $P_d = 1$ , decrease quickly as the satellite enters the

eclipse, but the UCEP algorithm only drops to approximately 30 percent detection over the same period of the eclipse. From [24], the ECEP MHT crosses 50 percent detection at approximately frame 840, while the new equal cost MHT developed crosses at frame 825. The point detector crosses at approximately frame 780 and the UCEP algorithm does not cross 50 percent until frame 875. Similar trends are present in the other nights, with UCEP MHT  $P_d$  improvements between 5-65 percent in (B) and 5-70 percent in (C) over the ECEP MHT and 10-90 percent in (B) and 10-95 percent in (C) over the point detector.

In all three days processed, the object goes from easily detectable to low  $P_d$  across approximately 100 frames. In [24] the transition happens across approximately 85 frames. The new ECEP MHT seems to match  $\mathcal{L}_e$  from equation (3.17), the method and results presented in [24] with a small number of differences. One of these differences is that the preprocessing of the data before implementation into the algorithm may be different. Another contributing factor is whether stars in close proximity to ANIK-F1 are removed or not. Stars entering the small frame being processed can negatively impact the detection performance by driving up the noise statistics for the window. Another difference is that the data is processed with different methods. In this new method, a SNR statistic is not used and the data is processed in risk space. As a result, the random numbers are combined in a different and non-linear method, giving a slightly different performance.

Another difference is the method of computing  $P_f$ . Actual collected data selected to have no object present is used instead of simulating a false alarm rate. Using the collected false alarm data described in section 3.3.1 with the algorithm to generate false alarm probability as opposed to estimating  $P_f$  from the threshold gives a more accurate measure of the true false alarm rate of the tests.  $P_f$  is calculated to be  $7.3\text{e-}4$  for the equal cost algorithm using the estimated  $\theta_i$  based on the threshold of  $\Gamma_{\text{M-ary}} = 6.22$  from [24]. The false alarm rates generated by running the ECEP and UCEP MHT are not equal. The calculated  $P_f$  for the unequal MHT is found to be  $2.8\text{e-}8$ . To give an even comparison

of detection across frames, a threshold  $\tau$  value of -27.5 is used in the UCEP algorithm, to match the false alarm rates between the two algorithms. Once the algorithms have the same  $P_f$ , the three consecutive frame rule is taken into effect. As mentioned previously, the SST requires the current BHT point detector to observe a detection over three consecutive frames to consider an object present. This helps reduce the false alarm rate due to single image noise spikes or other non-constant sources. The measured  $P_f$  and  $P_d$  rates are cubed to account for this effect.

To quantify the percent improvement in detection performance with an additional metric, the apparent magnitude between algorithms is calculated. By noting ANIK-F1's intensity at  $P_d = 0.5$  for each algorithm, the apparent magnitude,  $\Delta M$ , between them can be determined.

$$\Delta M = -2.5 \log_{10} \left( \frac{\mathcal{I} - \hat{B}}{\mathcal{I}_{\text{ref}} - \hat{B}} \right) \quad (3.30)$$

$\mathcal{I}$  is the total intensity in the pixel containing ANIK-F1 when either the equal or unequal cost algorithm crosses the 50 percent detection threshold, and  $\mathcal{I}_{\text{ref}}$  is the total intensity when the current BHT crosses 50 percent. A larger positive  $\Delta M$  indicates a dimmer object in comparison to the reference object.

Table 3.3: Apparent magnitude improvement of Equal and Unequal MHT over the current BHT at 50 percent detection threshold.

	13 March	14 March	15 March
<b>ECEP MHT</b>	1.67	0.46	1.06
<b>UCEP MHT</b>	2.40	0.87	1.44

On all three nights both of the MHT algorithms used saw an increase in  $\Delta M$  over the BHT. In addition, there is an improvement of 0.73, 0.41, and 0.38 in apparent magnitude when the UCEP algorithm is used.

The detection performance at the current SST program specified  $P_f$  is important, but does not completely compare the detection performance against a range of false alarm rates. To investigate  $P_d$  performance across varying levels of  $P_f$ , ROC curves are generated at multiple intensity levels.

### 3.4.2 Receiver Operating Characteristic.

A ROC curve is a method to demonstrate  $P_d$  and  $P_f$  as a function of the selected threshold levels. To generate a ROC curve, sets of  $P_d$  and  $P_f$  data pairs are calculated for a specific threshold level  $\tau$ . The threshold is varied until a full range of detection and false alarm probabilities between 0 and 1 are calculated. The ROC curve for the equal cost method is calculated with the following relation.

$$\mathcal{P}_e(\tau) = \sum_{\eta_p} F_\phi(\eta_p + \tau) p_\eta(\eta_p) \Delta\eta_p \quad (3.31)$$

The threshold can be combined with  $\eta_p$  in various ways, but addition is chosen because it allows for an easy way to determine  $\tau$  values needed, and it works even if the value for  $\eta_p$  is zero. Values for the threshold  $\tau$  are chosen to ensure two key factors. The first is that all possible values of  $P_f$  and  $P_d$  are obtained. The second is that there are enough points on the sampling grid to generate a smooth curve. The unequal cost ROC curve is found with the following equation.

$$\mathcal{P}_u(\tau) = \int_{-\infty}^{\Gamma_u + \tau} p(\mathcal{L}_u) d\mathcal{L}_u = F_{\mathcal{L}_u}(\Gamma_u + \tau) \quad (3.32)$$

Due to the large quantity of pixels being tested, a low  $P_f$  is required to give a manageable number of false alarms across each image. Due to the importance of low

$P_f$  values, the ROC curve is plotted as a semi-log plot. Taking the log of  $P_f$  provides better insight into algorithm performance across a larger set of values.

Figure 3.5 includes ROC curves for both the ECEP and UCEP MHT algorithms. The ROC curves are produced with 15 frame windows centered at three different frames from the data collection on 13 Mar 2012.

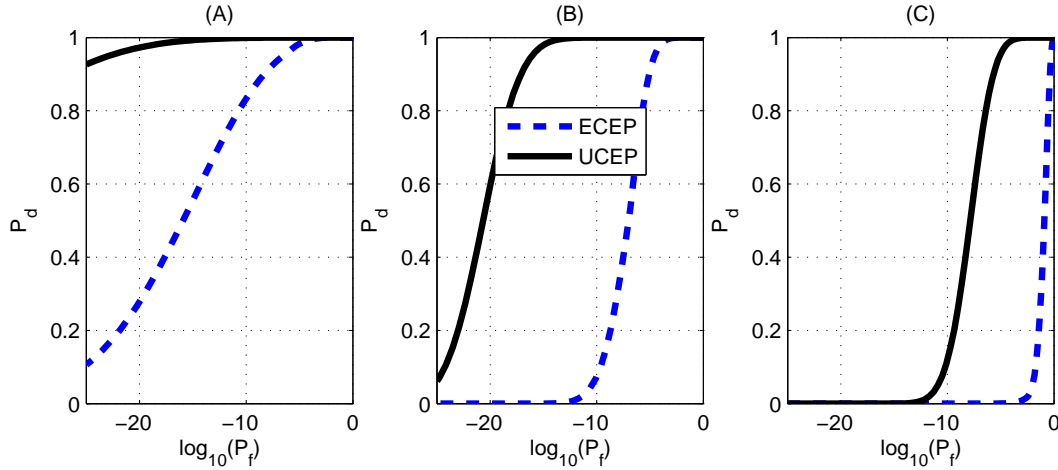


Figure 3.5: ROC curves centered at frames (A) 800 (B) 850 (C) 900 from 13 March 2012 using a 15 frame window with  $M = 10$ .

In (A), the window is centered at frame 800. At this point in the collection, the satellite is still very visible. The ECEP and UCEP algorithms both achieve a greater than 80 percent  $P_d$  at up to  $10e-10 P_f$ . The ECEP algorithm drops off more quickly than the UCEP algorithm, giving up to an 80 percent increase when  $P_f = 10e-25$ . In (B), frame 850 is used as the center frame. The satellite is more difficult to detect in this window. The UCEP algorithm performs much better for a large variety of  $P_f$  values, including up to a 100 percent difference at  $10e-12$ . In (C), a window around frame 900 is utilized. The satellite is very difficult to detect at this low intensity. Looking at an image at this point, it would be hard to determine if an object is present or not, as shown in Figure 3.6. Figure

3.6 shows ANIK-F1 at three points as it enters eclipse on 13 March. Both algorithms have a lower probability of detection for the same probability of false alarm when compared to earlier frames. At the realistic  $P_f$  values that might be used in the SST system, both algorithms are below 10 percent detection.

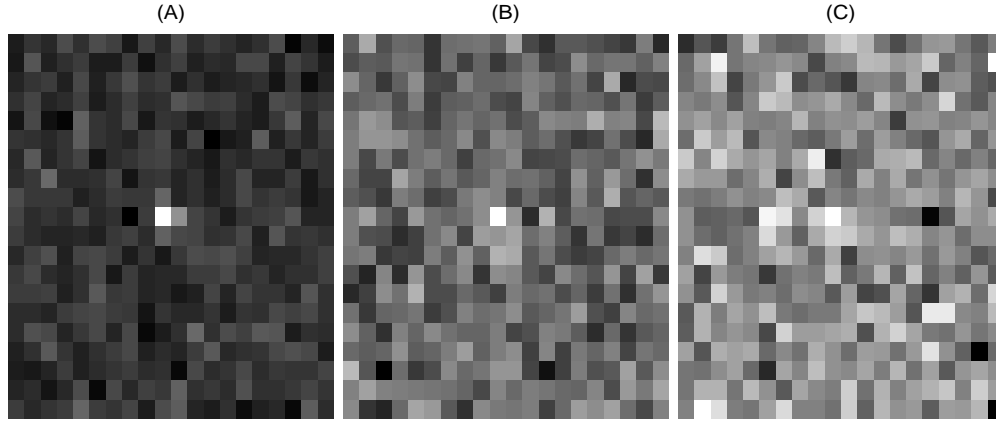


Figure 3.6: ANIK-F1 at 3 points during the eclipse, captured with the SST. The frames used are (A) 800, (B) 850, and (C) 900 on 13 March. ANIK-F1 loses intensity as it enters the eclipse and more close resembles the background.

The next factor investigated is the number of hypotheses,  $M$ , used in the test. As described in section 3.2.1, the number of hypotheses used may impact the detection performance of the algorithm. To compare  $M$ , the UCEP structure,  $\mathcal{L}_u$ , is used. The data collected on 13 Mar 2012 is analyzed in this chapter with other nights demonstrating similar performance. Figure 3.7 shows ROC curves for  $M$  values of 2, 6, and 10, for varying satellite intensities. For  $M = 6$  four corner sub-pixel locations are used along with the center of the pixel. To generate these corner locations, both  $\alpha$  and  $\omega$  shifts of  $\pm 30\mu\text{m}$  are used. For  $M = 10$ , top, bottom, and side locations are added. These locations use a shift of  $\pm 30\mu\text{m}$  in either  $\alpha$  or  $\omega$ , and no shift in the other dimension.

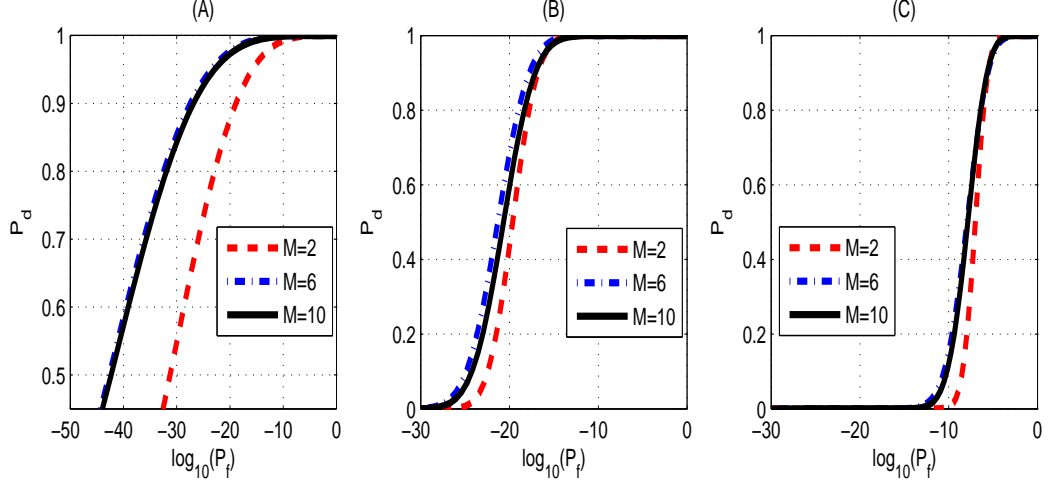


Figure 3.7: ROC curve using UCEP MHT,  $\mathcal{L}_u$ , at frame (A) 800 (B) 850 and (C) 900 from 13 March 2012 using a 15 frame window. Three values of  $M$  are compared: 2, 6, and 10.

Several interesting trends are apparent as the value of  $M$  changes. One important observation is that the number of hypotheses used has an impact on the performance of the algorithm. This effect is more noticeable for higher intensity objects. In (A), the satellite is still intense, and the  $M = 2$  ROC curve is lower than both the 6 and 10 hypotheses case. The performance difference is an up to 60 percent lower detection rate for the same false alarm rate, implying that the MHT performs better than the BHT. As the object loses intensity and enters the eclipse, the separation between the MHT and the BHT is decreased. In (B), at frame 850 the max detection separation is approximately 20 percent, and in (C) at frame 900 the separation is approximately 15 percent. Another interesting result is that the difference between the number of hypotheses beyond the binary case is less significant. Using  $M = 6$ , the detection performance is never below the  $M = 10$  case. The improvement ranges from 0-5 percent depending on the night being processed and the false alarm rate. This result demonstrates that there is a trade-off between increasing the number of sub-pixel locations to capture potential aliased PSF and creating additional false alarms. The choice of  $M = 6$  is due to the fact that it is the first multiple hypothesis case

that will symmetrically cover potential sub-pixel locations. This is done by choosing the four corners and the center.

One important thing to note is that the  $M = 2$  case shown in Figure 3.7 is a BHT, but is not the point detector currently used by SST. There are two differences between this binary correlation and a point detector. The first difference is that in the correlation, a 15x15 pixel window is used to make the decision between  $H_0$  and  $H_1$ , and only a single pixel is used in the point detector. Secondly, the correlation uses outlier removal as described in section 3.4.

In addition to the performance increase, using  $M = 6$  also reduces the required computations to calculate  $\mathcal{L}_u$ . By using six hypotheses, only five alternate hypothesis terms need to be calculated, compared to nine when  $M = 10$ , reducing computation cost by approximately 45 percent, assuming the processing times for each hypothesis are equal. The selection of  $M$  gives a way to control the computational time required for the unequal cost method, but in general this method is more costly than the currently implemented point detector. Due to the fact that  $\mathcal{L}_u$  is not linear, processing techniques like Fourier transforms cannot be used to increase processing speed. Currently the point detector in the SST system runs in real time, and can create detections as quickly as images are captured. Using the new proposed UCEP MHT, the same processing technique will not be possible. This allows the user a choose between processing speed and detection performance.

### **3.5 Full Frame Implementation**

The UCEP algorithm presented in this research is more computationally complex than previously proposed methods. To implement the algorithms into the current SST data processing pipeline, it is important to investigate the feasibility of achieving real time or near real time analysis. Looking at the final detection algorithm for the unequal cost method gives insight into possible methods for processing the data more quickly.



$$\mathcal{L}_u = \sum_{k=1}^{M-1} \exp \left[ \sum_{x=1}^{N_x} \sum_{y=1}^{N_y} \frac{\theta_k h_k(x, y)}{\sigma^2} \left( D(x, y) - \hat{B} - \frac{\theta_k h_k(x, y)}{2} \right) \right] \quad (3.33)$$

The most computationally expensive portion of the algorithm is performing operations on the large matrices. As mentioned previously, the full frame data, 2x2 binned, contains 6144x4096 pixels. The first step to increase the processing speed is to separate the argument of the exponential function in  $\mathcal{L}_u$  into data dependent and non-data dependent calculations.

$$\sum_{x=1}^{N_x} \sum_{y=1}^{N_y} h_k(x, y) D(x, y) - \underbrace{\frac{\hat{B} \theta_k}{\sigma^2} \sum_{x=1}^{N_x} \sum_{y=1}^{N_y} h_k(x, y) - \frac{\theta_k^2}{2\sigma^2} \sum_{x=1}^{N_x} \sum_{y=1}^{N_y} h_k(x, y)^2}_{\psi} \quad (3.34)$$

$\psi$  represents the non-data dependent portion of the equation. Both  $\hat{B}$  and  $\sigma$  are background data statistics that need to be computed in each frame, and are needed for both ECEP and UCEP algorithms. The only variable changing from frame to frame is the data,  $D(x, y)$ . The significant difference is the correlation between the data and the  $k^{th}$  PSF. The UCEP algorithm has two additional data processing steps; the exponential function and a sum of the  $M - 1$  total hypotheses.

Allowing the window of  $N_x$  and  $N_y$  to go to the entire frame allows for simultaneous processing of an entire data frame. A small window no longer needs to be used to cycle through the image, decreasing the processing time. MATLAB has a function that allows data processing on the graphics card. Using this function, the correlation can be passed to a compatible graphics card. The correlation function can be computed more quickly with this method, allowing for a faster overall processing time.

The full frame data is processed with a HP Z820 workstation. The processor in the workstation is a Intel Xeon CPU E5-2650 at 2.6GHz with 64 GB of RAM. The software used is Windows 7 and MATLAB R2015b. The graphics processor used is a NVIDIA Quadro K6000. Defining  $T_{\text{ECUP}}$  and  $T_{\text{ECEP}}$  as the time it takes the computer described to

process the respective algorithms, the average and maximum processing times are shown below.

Table 3.4: Processing times for equal- and unequal-cost algorithms processed on graphics card.

	$T_{\text{ECEP}}$	$T_{\text{ECUP}}$	$\Delta T$
<b>Mean</b>	187 ms	237 ms	26.7%
<b>Maximum</b>	408 ms	568 ms	39.2%

$\Delta T$  represents the additional processing time required by the ECUP algorithm as a percentage. As Table 3.4 demonstrates, there is a definite jump in processing time required by the UCEP algorithm. The 26.7 percent additional time may or may not impact real time operation of the processing depending on the required time for other processes. These processes include loading the data frames, clustering, orbit determination, and other post detection processing. These processes are common to both the ECEP and UCEP algorithms.

### 3.6 Conclusions

This chapter presents a method of increasing the detection capability of the SST over the current BHT algorithm. Due to the spatial aliasing caused by the pixel size, a MHT is used to account for potential different sub-pixel shifts resulting in changes to the shape and distribution of the PSF. These PSFs are used to correlate with received data to detect objects. It is demonstrated that the probability of detection is increased by using an UCEP MHT detection algorithm when compared to an ECEP algorithm.  $P_d$  gains of up to 80 percent are observed for the same  $P_f$  rate. The number of hypotheses used within the MHT is also investigated. It is found that there is a relationship between the number of hypotheses

used and detection performance. The results show that a MHT clearly outperforms a BHT, and that using 6 hypotheses slightly outperformed 10, with the additional benefit of reduced computational time. With the  $M=6$  hypothesis assumption, the aliased PSFs proposed more accurately match the observed PSF in the data without raising the probability of false alarm by introducing additional hypotheses.

The key contributions of this research are a new reduced algorithm for implementing an UCEP MHT based on received data with a Gaussian distribution, and a method for determining average  $P_d$  and  $P_f$  based on a general cost structure. This chapter investigates the limiting cases of cost selections. The first being that all errors have the same cost, resulting in a large emphasis being placed on correctly identifying the correct sub-pixel location. The second limiting case is the UCEP algorithm. The UCEP does not put any cost on errors in sub-pixel location, and instead uses that data in essence as a nuisance parameter. The ability to generate ROC curves for any intermediate case can be useful in determining the best cost structure for a specific application.

There are several areas of future research that could improve or add to the results presented. This research focuses on received data that is assumed to be Gaussian. Through this research, a method for implementing a different model for received data is developed that can be used on any potential distribution of received data. The limiting cases of costs are considered in this chapter. There are many additional cost structures in between the two presented here. For specific applications these cases may give better detection performance. The drawback is that they will not reduce as well as the equal or unequal cost schemes presented here. Additionally, the unequal cost method here is more computationally complex than the currently implemented algorithms. Simplification and efficient implementation are not a focus of this research. To use this algorithm operationally, these factors will need to be investigated further.

In the next chapter a Bayes risk MHT is further investigated by developing a detection algorithm with unequal prior probability.

## IV. Investigating Multiple Hypothesis Test Prior Probabilities

### 4.1 Introduction

The main goal in this chapter of the dissertation is to create a detection algorithm that uses an unequal prior probability assignment to improve detection capabilities. This chapter addresses the research question: Do the assignments of a priori probabilities in a MHT improve the detection performance?

The distribution of space objects on the CCD of a ground-based telescope, and how that sub-pixel position translates to several potential aliased PSFs is key in answering this research question. Due to the large number of potential space objects, their arbitrary location relative to the observation point, and physical properties of the optics, it is acceptable to assume that a RSO has a uniform probability of occurring anywhere within a single pixel. The question to be answered in this chapter is: assuming a uniform distribution across a single CCD pixel, what are the resulting prior probabilities,  $\pi_k$ , in a MHT? Additionally, if a detection algorithm is derived using these probabilities, is it able to outperform previously proposed hypothesis tests?

As described in Chapter 2, due to aliasing present in many telescopes, the sub-pixel position can affect both the shape and location of the resulting PSF. This chapter covers several different topics relating to the investigation of the prior probabilities. These aspects include: background and motivation for this type of MHT, a decision space analysis for assigning prior probabilities, optical modeling theory, and the development of the detection algorithm. The algorithm is tested against both simulated space objects and data collected from the SST.

## 4.2 Theory

To implement an unequal-prior detection algorithm, there are two important factors. One factor is the ability of the algorithm to reduce to a calculable statistic. Also pertinent is how well the algorithm detects objects, and realistic and representative values for the prior probabilities  $\pi_k$ . This section covers the theory on both of these topics.

### 4.2.1 *Optical Model.*

To mitigate the effects of aliasing, candidate PSFs are needed for the MHT to compare against. There are two approaches to producing these. The first is to capture representative PSFs from the collected data. The drawback to this method is that the PSF is specific to the conditions of the night captured, including the seeing,  $r_o$ , and the sub-pixel location of the object. A large sampling of objects would potentially need to be investigated in order to obtain complete models for the  $M$  alternate hypotheses.

Alternatively, this research uses an optical model to create representative PSF based on the input conditions. A more detailed derivation is described in section 3.1. The final PSFs  $h_k(x, y)$ , shown in equation (3.10), are created through a combination of four important factors: the optical PSF including lens aberrations and telescope parameters, a long exposure atmosphere model [17], any shift from the center of the CCD, and the spatial aliasing effect modeled as a blurring function.

The modeled PSFs  $h_k(x, y)$  are used for several purposes in this chapter. It is used to evaluate the decision space and determine prior probabilities, for data creation, and is a key factor in the detection algorithm. Next, the decision space for the hypotheses in this test is investigated to determine the prior probability.

### 4.2.2 *Bayes Cost and Priors Discussion.*

To make a decision if an object is present, a Bayes Criterion is used [25]. This equation provides a method of choosing the hypothesis that results in less risk  $\mathcal{R}$  on average.

$$\mathcal{R} = \sum_{i=0}^{M-1} \sum_{k=0}^{M-1} \pi_k C_{ik} \int_{Z_i} p(\mathbf{D}|H_k) d\mathbf{D} \quad (4.1)$$

$M$  is the total number of hypotheses considered. The cost,  $C_{ik}$ , represents the impact of choosing hypothesis  $i$  when hypothesis  $k$  has occurred. The value of  $C_{ik}$  ranges from zero to one, with one giving the largest cost penalty to a decision. The prior probabilities,  $\pi_k$ , represent how likely each potential hypothesis is to occur. The priors range between zero and one, and must sum to a total of one. When using a Bayes Criterion-based MHT, there are several variables that impact the algorithm that results from the hypothesis test. The two discussed in this paper are the costs,  $C_{ik}$  and the a priori probabilities,  $\pi_k$ .  $\mathbf{D}$  is a matrix containing one single frame of data.  $H_k$  is the  $k^{\text{th}}$  hypothesis.  $H_0$  is the null hypothesis, where it is assumed that no space object is present.  $H_1$  through  $H_{M-1}$  are the alternate hypotheses. These correspond to instances where the space object is considered present, and each hypothesis signifies a different sub-pixel position. These sub-pixel positions are described in Table 4.1.

Different cost and a priori probability approaches have been researched, and there are several differences between the approaches. The first area of difference is the assignment of cost. An Equal-Cost Equal-Prior (ECEP) test, originally proposed in [24], penalizes the algorithm for incorrectly deciding between two alternate hypotheses. This emphasis on determining the correct sub-pixel position can lead to more accurate sub-pixel position estimates, potentially at the cost of the detection of space objects. Alternatively, an Unequal-Cost Equal-Prior (UCEP) assumption will not penalize for selecting the wrong alternate hypothesis, as long as an object is correctly detected [67]. Unequal-cost algorithms are more computationally complex and do not reduce to a SNR sufficient statistic. Unequal-cost algorithms are not discussed further in this chapter.

The other variables where different assumptions can be made in a Bayes Risk MHT are the a priori probabilities. In this chapter, two different a priori probability approaches

are investigated. They are an Equal-Cost Equal-Prior (ECEP) and an Equal-Cost Unequal-Prior (ECUP). ECEP assumes the following cost and probability assignment:

$$C_{ik} = \begin{cases} 0, & i = k \\ 1, & i \neq k \end{cases}, \quad \pi_k = \frac{1}{M}. \quad (4.2)$$

The ECUP algorithm assumes the same cost assignment, but the prior probabilities,  $\pi_k$ , for each hypothesis  $k$  are not necessarily the same or  $\frac{1}{M}$ . The prior probabilities are typically assumed to be equal if there is no prior knowledge of the system or method of determining accurate values for  $\pi_k$ . This chapter considers several methods for finding accurate prior probability values, and determines if more binary detections can be found with the resulting algorithm.

#### 4.2.3 *Decision Space Analysis.*

A key element to creating an algorithm that takes into account an unequal prior probability assumption is determining accurate prior probabilities for each sub-pixel hypothesis,  $H_k$ . Without a method of accurately determining these values, the actual benefit of an ECUP test may not be realized. The assignment of priors reflects how point sources present in different locations within a CCD translate into potential PSFs. This paper investigates three potential methods for segmenting the pixel into a decision space. These methods are: a distance-based metric, a correlation metric, and an empirical method. Each method is described and analyzed in the following paragraphs.

A critical assumption common with all of these methods is that a space object is equally likely at any position within a pixel. This sub-pixel position,  $(\alpha, \omega)$ , is the physical distance in  $\mu m$  within a 2x2 binned pixel. This assumption implies a uniform probability across the entire pixel. To segment the decision space, a sub-pixel map is created. In the map, each position tested has the same probability of occurrence. To ensure a fine enough coverage of the entire pixel, sub-pixel positions are tested every  $1\mu m$  in both  $\alpha$  and  $\omega$ . This results in 31 positions in each dimension and 961 positions total.



In this chapter,  $M = 10$  hypotheses are used in the test. These hypotheses are PSFs generated through the optical model where a space object is assigned to be in a defined location within a pixel. As previously mentioned, the hypotheses positions are defined by  $\alpha$  and  $\omega$ , the position within a  $30 \times 30 \mu\text{m}$  pixel, with the origin being the center of the pixel. The locations within a pixel are the corners where  $\alpha = \pm 15$  and  $\omega = \pm 15$ , sides where  $\alpha = 0$  and  $\omega = \pm 15$ , top and bottom where  $\alpha = \pm 15$  and  $\omega = 0$ , and the center of each pixel.

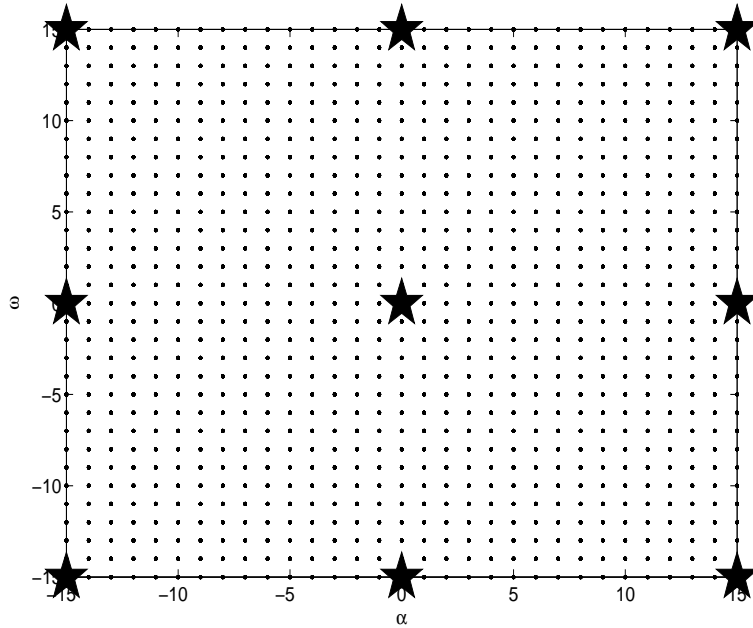


Figure 4.1: Decision space within a single CCD showing all sub-pixel locations, along with the locations of the nine alternate hypotheses.

There are multiple reasons for using these positions. First, they give an even representation of the potential resulting PSFs based on the coverage of the entire pixel. Additionally, they can reduce computational complexity and reduce the number of tests, due to sharing the corners and sides hypotheses between adjacent pixels. In this case,

rather than testing all nine alternate hypotheses, only five are needed for each pixel. This approach was first proposed in [24]. An alternate layout of hypothesis positions with  $M = 6$  is proposed in chapter 3, but is not investigated in this chapter.  $M = 10$  hypotheses are used in this research to compare against the previously proposed  $M = 10$  ECEP algorithm.

The first method considered is the correlation metric. Both the ECEP and ECUP algorithms are based on a matched filter, or correlation test. By determining which hypothesis correlates most closely with each sub-pixel position tested, an assignment matrix can be formed by noting the most closely correlated hypothesis at each sub-pixel position  $\alpha, \omega$ . This is done with the following equation:

$$\mathcal{H}_c(\alpha, \omega) = \underset{k}{\operatorname{argmax}} \left[ \sum_{x=1}^{N_x} \sum_{y=1}^{N_y} \frac{T_{\alpha,\omega}(x, y) h_k(x, y)}{\sigma_k} \right]. \quad (4.3)$$

$\sigma_k$  is a normalization term based on the  $k^{\text{th}}$  hypothesis present in the ECEP algorithm,  $\sigma_k = \sqrt{\sum_{x=1}^{N_x} \sum_{y=1}^{N_y} h_k^2(x, y)}$ .  $\mathcal{H}_c(\alpha, \omega)$  is an entry in the hypothesis assignment matrix  $\mathcal{H}_c$ . Each coordinate represents a sub-pixel position and contains the closest hypothesis match.  $T_{\alpha,\omega}(x, y)$  is a 16x16 pixel modeled PSF based on a space object at the sub-pixel location  $(\alpha, \omega)$ . An important note is that the PSFs for  $T_{\alpha,\omega}(x, y)$  and  $h_k(x, y)$  are generated by performing the appropriate shift on the highly sampled model PSFs and downsampled as described in equation (3.9).

The second proposed method for assigning a sub-pixel position to a hypothesis being considered is a distance-based metric. The distance vector in this case is between the  $k^{\text{th}}$  hypothesis position and the proposed  $\alpha, \beta$  sub-pixel position. There are several methods for measuring the distance, or size of a vector. In this research, a 2-norm is used to find the “closest point” between the sub-pixel position being tested and the locations of the hypotheses.

$$\mathcal{H}_d(\alpha, \omega) = \underset{k}{\operatorname{argmin}} \left( \|\vec{V}_k\| \right) \quad (4.4)$$

$\vec{V}_k$  is a vector between each hypothesis  $k$  located at  $(\alpha_k, \omega_k)$ , and the sub-pixel position,  $(\alpha, \omega)$ , being tested.  $\mathcal{H}_d(\alpha, \omega)$  is the hypothesis assignment matrix for the distance-based metric. At each sub-pixel position, nine vectors are created and the smallest 2-norm is selected as the hypothesis that best represents the sub-pixel position being tested.

Figure 4.2 shows the decision space analysis for a single CCD pixel resulting from the correlation and distance-based metrics. The plots demonstrate the physical layout of the decision space and the boundaries between each hypothesis. Each sub-pixel position is assigned a corresponding hypothesis and is grouped into a section with similarly assigned hypotheses.

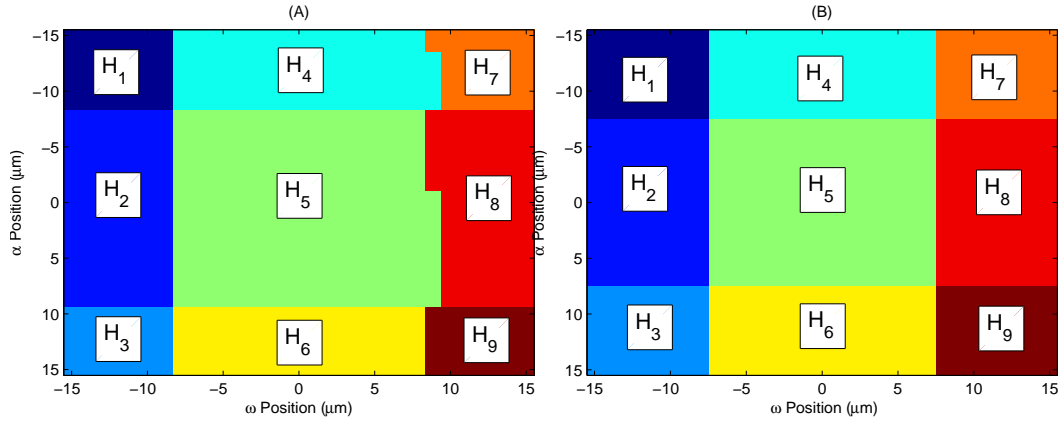


Figure 4.2: Decision space analysis for a single SST CCD pixel. The hypothesis assignment matrix for (A) the correlation metric,  $\mathcal{H}_c$ , and (B) distance metric,  $\mathcal{H}_d$ . Each color shade corresponds to a similar hypothesis. Sub-pixel positions are tested every  $1\mu\text{m}$ .

Looking at the distribution of hypothesis assignments in Figure 4.2, there are similarities between the correlation and distance-based metrics. Both segment the decision space into rectangles based on the location of the hypotheses. The correlation metric has sub-pixel positions between  $H_5$  and  $H_8$ , as well as  $H_4$  and  $H_7$ , that do not directly create

perfect rectangular boundaries. These are due to optical effects not included in the distance metric, such as lens or mirror aberrations and atmospheric effects.

The final method being considered to determine prior probabilities is an empirical method. The empirical method uses detection made on collected SST data to determine how often each hypothesis is observed. This method depends on implementing the ECEP algorithm and noting the selected hypothesis. One drawback is that the empirical method only analyzes objects that it detects. The inherent assumption when using this method is that non-detectable objects will have the same spatial distribution as detectable objects. Using the ECEP algorithm, the following SNR equation can be used to assign sub-pixel positions [24]:

$$\text{SNR}_k = \sum_{x=1}^{N_x} \sum_{y=1}^{N_y} \frac{(D_{x_o, y_o}(x, y) - B) h_k(x, y)}{\sigma \sigma_k}. \quad (4.5)$$

$D_{x_o, y_o}(x, y)$  is a data window that is  $N_x$  by  $N_y$  pixels centered at  $x_o, y_o$ .

$$\mathcal{H}_e(x_o, y_o) = \underset{k}{\text{argmax}} [\text{SNR}_k] \quad (4.6)$$

The three methods described to this point all have an associated hypothesis assignment matrix,  $\mathcal{H}$ . This matrix gives each sub-pixel position the hypothesis that it most closely resembles. The prior probability values calculated from all three methods are included in section 4.4. One distinction between the methods is that  $\mathcal{H}_c$  and  $\mathcal{H}_d$  represent a single CCD pixel, while  $\mathcal{H}_e$  represents an entire frame of SST data. Therefore,  $\mathcal{H}_e$  does not provide insight into how the decision space inside the pixel is physically distributed as shown in Figure 4.2, only the prior probability of each hypothesis occurring.

#### 4.2.4 Hypothesis Test Derivation.

The next step is to implement the potential  $\pi_k$  values discussed in the previous section into a detection algorithm and determine how the change in assumptions affects the detection performance of the algorithm. As mentioned previously, with an unequal-

prior approach there are two choices for costs: Equal-Cost Unequal-Prior (ECUP) and Unequal-Cost Unequal-Prior (UCUP). When implementing an equal-cost assumption, the Bayes criterion [25] can be reduced to the following relation:

$$\max_k \left[ \frac{\pi_k}{\pi_0} \frac{p(\mathbf{D}|H_k)}{p(\mathbf{D}|H_0)} \right] \underset{H_0}{\overset{H_k}{\gtrless}} 1 \quad (4.7)$$

where  $p(\mathbf{D}|H_k)$  is the conditional PDF of the data, given that hypothesis  $k$  is true.  $\mathbf{D}$  is a matrix that represents a received image. The hypothesis test will select the max ratio of probabilities and conditional PDFs and compare the resulting ratio against one. Based on the result of the comparison, a decision on which hypothesis is selected can be made. If the ratio is less than one, it is assumed that no object is present. If the ratio is greater than one, an object is assumed present and the largest hypothesis  $k$  is selected. A varying selection of costs will result in a different ratio test. Alternate cost assumptions are not investigated in this chapter.

To reduce equation (4.7), a model for what the received data  $\mathbf{D}$  contains is needed. This model is described in equation (4.8).

$$I(x, y) = \begin{cases} \theta h_k(x, y) + B & H_k, k \in [1, 9] \\ B & H_0 \end{cases} \quad (4.8)$$

$\theta$  is the modeled RSO intensity.  $h_k(x, y)$  is the PSF based on the  $k^{th}$  hypothesis described in section 4.2.1 and  $B$  is the background photo count.  $I(x, y)$  represents the average expected value, but there will be noise present in the data. As a result, a noise model is needed to completely represent the conditional PDF. In this case, the model assumes Poisson counting as the dominant noise source. In previous research efforts, both Poisson and Gaussian noise assumptions have been made. One reason for this is that it has been shown that for a flat background, as is the case in this situation, both Gaussian and Poisson assumptions lead to the same algorithm [22, 35]. Multiple sources of noise tend to give an overall Gaussian distribution to the noise present in the system. Alternative

noise assumptions are investigated further in Chapter 5 [68]. Assuming an independent joint Gaussian noise distribution, the PDF ratio in equation (4.7) results in the following relation:

$$p(\mathbf{D}|H_k) = (2\pi\sigma^2)^{-\frac{N_x N_y}{2}} \exp\left(-\sum_{x=1}^{N_x} \sum_{y=1}^{N_y} \frac{(D(x,y) - I(x,y))^2}{2\sigma^2}\right). \quad (4.9)$$

$N_x$  and  $N_y$  are the number of pixels in the  $x$  and  $y$  direction.  $\sigma$  is the measured standard deviation of the received data  $D(x,y)$ . Combining equations (4.7) and (4.8), combining exponentials, and expanding gives the following equation:

$$\exp\left[\sum_{x=1}^{N_x} \sum_{y=1}^{N_y} -\frac{1}{2\sigma^2} (\theta^2 h^2(x,y) - 2\theta h(x,y)(D(x,y) - B))\right] \underset{H_0}{\overset{H_k}{\geq}} \frac{\pi_0}{\pi_k}. \quad (4.10)$$

This equation can be further reduced by taking the natural log, removing the exponential function.

$$\sum_{x=1}^{N_x} \sum_{y=1}^{N_y} -\frac{1}{2\sigma^2} (\theta^2 h^2(x,y) - 2\theta h(x,y)(D(x,y) - B)) \underset{H_0}{\overset{H_k}{\geq}} \ln\left(\frac{\pi_0}{\pi_k}\right) \quad (4.11)$$

It is obvious that for an equal-prior assumption, the natural log of prior probabilities goes to zero. This assumption gives one less term on the threshold side of the equation to be concerned with. Continuing to reduce the left side of the equation gives:

$$\begin{aligned} & \sum_{x=1}^{N_x} \sum_{y=1}^{N_y} (-\theta^2 h^2(x,y) + 2\theta h(x,y)(D(x,y) - B)) \underset{H_0}{\overset{H_k}{\geq}} \ln\left(\frac{\pi_0}{\pi_k}\right) 2\sigma^2 \\ & \sum_{x=1}^{N_x} \sum_{y=1}^{N_y} 2\theta h(x,y)(D(x,y) - B) \underset{H_0}{\overset{H_k}{\geq}} \ln\left(\frac{\pi_0}{\pi_k}\right) 2\sigma^2 + \theta^2 \sum_{x=1}^{N_x} \sum_{y=1}^{N_y} h^2(x,y) \\ & \sum_{x=1}^{N_x} \sum_{y=1}^{N_y} (D(x,y) - B)h(x,y) \underset{H_0}{\overset{H_k}{\geq}} \ln\left(\frac{\pi_0}{\pi_k}\right) \frac{\sigma^2}{\theta} + \frac{\theta \sum_{x=1}^{N_x} \sum_{y=1}^{N_y} h^2(x,y)}{2}. \end{aligned} \quad (4.12)$$

The left side of equation (4.12) now resembles a SNR, but without the standard deviation of the data. To give a true SNR, both sides are divided by  $\sigma$  to give the following:

$$\sum_{x=1}^{N_x} \sum_{y=1}^{N_y} \frac{(D(x,y) - B)}{\sigma} h(x,y) \underset{H_0}{\overset{H_k}{\geq}} \ln\left(\frac{\pi_0}{\pi_k}\right) \frac{\sigma}{\theta} + \frac{\theta \sum_{x=1}^{N_x} \sum_{y=1}^{N_y} h^2(x,y)}{2\sigma} \quad (4.13)$$

The left side of equation (4.13) contains a correlation of the received data  $D(x,y)$  and the  $k^{\text{th}}$  PSF. This implies that the algorithm is looking for how similar the received data and the expected PSF are. Introducing a normalization factor to ensure that the SNR statistic is unit variance [24] gives the following equation:

$$\underbrace{\sum_{x=1}^{N_x} \sum_{y=1}^{N_y} \frac{(D(x,y) - B)}{\sigma} \frac{h(x,y)}{\sigma_k}}_{\text{SNR}_k} \underset{H_0}{\overset{H_k}{\geq}} \underbrace{\frac{\sigma \ln\left(\frac{\pi_0}{\pi_k}\right)}{\theta \sqrt{\sum_{x=1}^{N_x} \sum_{y=1}^{N_y} h^2(x,y)}}}_{W_k} + \underbrace{\frac{\theta \sum_{x=1}^{N_x} \sum_{y=1}^{N_y} h^2(x,y)}{2\sigma \sqrt{\sum_{x=1}^{N_x} \sum_{y=1}^{N_y} h^2(x,y)}}}_{\Gamma} \quad (4.14)$$

where  $\sigma_k$  is a normalization factor to keep the SNR a zero mean unit variance random variable [24]. Investigating the threshold gives insight into the effect on the threshold of unequal prior probability.

Combining equations (4.7) and (4.20) and grouping terms dependent on  $K$  gives this reduced equation:

$$\max_k [\text{SNR}_k - W_k] = \text{SNR}_{W_k} \underset{H_0}{\overset{H_k}{\geq}} \Gamma_k. \quad (4.15)$$

where  $W_k$  is a weighting factor based on the non-equal prior probabilities. If  $\pi_0 = \pi_k$ , then the weighting term will reduce to zero and equal the threshold in the equal prior probability case. The ratio of  $\pi_0$  to  $\pi_k$  can increase or decrease the weighting factor, changing the probability of false alarm and detection. Increasing the probability of any hypothesis other than the null hypothesis will lower the effective threshold value.

Modifying the SNR by the weighting factor changes the mean, and therefore the algorithm does not have exactly the same  $P_f$  as [24]. In this research the  $P_f$  is determined through applying the algorithm to simulated data containing no RSO. Due to this factor, a false alarm analysis is also included, leading to ROC curves that directly compare performance across a large range of  $P_f$  values.

It is important to note that the threshold  $\Gamma$  is a function of  $k$ . This implies that there is a different threshold for each of the hypotheses. The hypothesis dependent threshold from equation (4.15) is used for the analysis of the simulated data. In the next section, the Bayes risk is derived in a different method, creating an hypothesis independent threshold.

#### 4.2.5 Hypothesis Independent Threshold.

Beginning with equation (4.20), the goal in this section is to derive a detection algorithm that is independent of  $k$  in the threshold. This was originally proposed to help prove that the prior probability of the null hypothesis does not affect detection performance. The proof of the null hypothesis prior probability is covered in section 4.2.6.2.

$$\sum_{x=1}^{N_x} \sum_{y=1}^{N_y} \frac{(D(x, y) - B)}{\sigma} h_k(x, y) \underset{H_0}{\overset{H_k}{\geq}} \ln \left( \frac{\pi_0}{\pi_k} \right) \frac{\sigma}{\theta} + \frac{\theta \sum_{x=1}^{N_x} \sum_{y=1}^{N_y} h^2(x, y)}{2\sigma}. \quad (4.16)$$

Separating equation (4.16)

$$\text{SNR}_k = \sum_{x=1}^{N_x} \sum_{y=1}^{N_y} \frac{(D(x, y) - B)}{\sigma} h_k(x, y) \quad (4.17)$$

$$W_k = \frac{\sigma \ln \left( \frac{\pi_0}{\pi_k} \right)}{\theta} + \frac{\theta \sum_{x=1}^{N_x} \sum_{y=1}^{N_y} h^2(x, y)}{2\sigma} \quad (4.18)$$

$W_k$  is effectively a weighting term that modifies the SNR value based on the likelihood of the hypothesis occurring. A weighting term is needed for each hypothesis  $k$ , and it can be precomputed for each set of priors and PSF hypotheses used. The computation of these terms does not add significant processing time compared to an ECEP test. The second



term in the weighting factor is what is traditionally defined as the threshold term  $\Gamma$ .  $\Gamma$  is generally the threshold value that sets the false alarm rate for the hypothesis test. This is set to 6 for the currently implemented SST BHT, but it is modified to 6.2212 to keep a constant false alarm rate in the ECEP MHT presented in [24]. More discussion regarding setting the desired  $P_f$  rates is covered in section 4.3.3.

In the new MHT algorithm, both SNR and  $W_k$  have a dependence on  $k$ , and are moved to the left side of the equation. Selecting the hypothesis that gives the largest value indicates which hypothesis is most likely to have occurred. This hypothesis is then compared against the null hypothesis to make a final detection decision.

$$\max_k [\text{SNR}_k - W_k] \underset{H_0}{\overset{H_k}{\geq}} 0 + \tau \quad (4.19)$$

The algorithm is theoretically compared against a threshold of zero, but a threshold adjustment term,  $\tau$ , is added to achieve different  $P_f$  values. Selecting a specific  $\tau$  value allows for the algorithm to operate at the desired false alarm rate. Comparing against the proposed ECEP test as shown below, from [24], the similarities can be quickly observed.

$$\max_k [\text{SNR}] \underset{H_0}{\overset{H_k}{\geq}} \Gamma \quad (4.20)$$

One noticeable benefit is that the equal cost portion of the algorithm still preserves the ability to select a hypothesis  $k$ . In [67], improved detection performance was observed, but the algorithm could only make a binary decision between a space object being present or not. The sub-pixel position information available from the ECEP and ECUP algorithms is shown to be useful in increasing tracking accuracy by Sligar [69]. Another difference is the additional calculation required for the weighting terms. As mentioned previously,  $W_k$  does not depend on the full frame data, and can be computed once per frame to get accurate background standard deviation and updated priors if desired.

As shown, the derived ECUP algorithm is able to be reduced to a sufficient statistic, and is not too computationally complex. These factors are all positive indicators for a successful algorithm. Next, the three methods for determining realistic and accurate prior probabilities are investigated.

#### **4.2.6 Investigating Null Hypothesis Probability.**

Two methods are used to investigate the potential values for the null hypothesis. It is theorized that the value selected for the null hypothesis value does not change the capabilities of the detection algorithm. If this is shown to be the case, there is no need to determine an accurate estimate for  $\pi_0$ .

The first method used is to perform the detection algorithm on simulated data with several different potential  $\pi_0$  values. If  $P_d$  does not change significantly across the tested values, it can be assumed that the value for  $\pi_0$  has no impact. Alternatively, an analytic approach is used based on the hypothesis independent MHT proposed in equation (4.19). These approaches are covered in the next two sections.

##### **4.2.6.1 Simulation.**

After assigning alternate hypotheses prior probabilities, the probability for null hypothesis  $H_0$  needs to be determined. Accurately determining this probability empirically from the collected data is difficult. This is due to the large number of stars, satellites, debris, and other space objects, and their spatial distribution. Instead of attempting to estimate a value for  $\pi_0$ , this paper shows that its value does not significantly change detection performance. The probability of an RSO being present in any pixel being tested is  $\pi_0$ . Figure 4.3 shows the effect that implementing the detection algorithm from equation (4.20) with  $\pi_0$  values ranging from 0.05 to 0.95 has on computed  $P_d$ . Each  $\pi_0$  test computed over 100 Monte Carlo iterations to determine its statistics. Each iteration consists of 100 independent RSOs to determine the  $P_d$  value at the specified  $P_f$  of  $1e - 10$ .

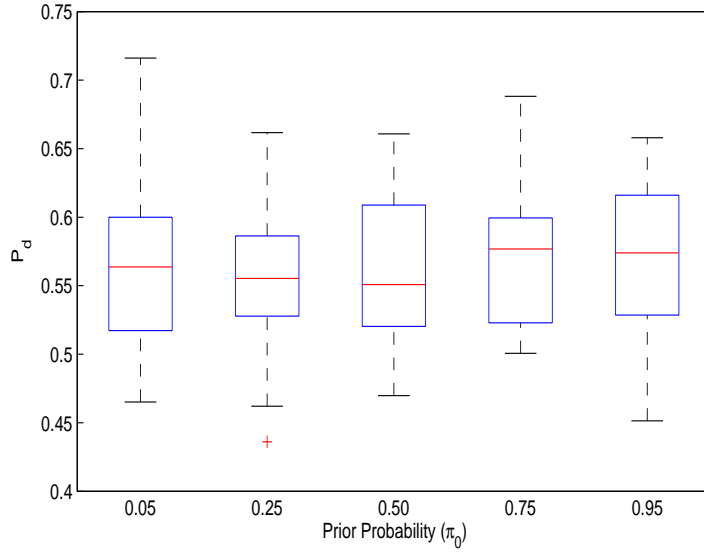


Figure 4.3: Analysis of  $P_d$  for varying  $\pi_0$  prior probabilities for  $P_f = 1e - 10$ .

Figure 4.3 shows that there is no significant change in  $P_d$  for a wide variety of  $\pi_0$  values. In addition, investigating the means and standard deviations shows that all  $\pi_0$  is well within one standard deviation. As a result, it can be assumed that the impact of changing the null hypothesis prior probability  $\pi_0$  is negligible. In simulation, the value for  $\pi_0$  is chosen to be 0.10 to match the prior probability in the ECEP algorithm, which assigned all priors to be  $\frac{1}{M}$ . The remaining  $1 - \pi_0$  probability is assigned to the alternate hypotheses with the proportions described in Table 4.1.

#### 4.2.6.2 Analytic.

All the methods for determining prior probabilities for the null hypotheses described in section 4.2.3 divide 100 percent of the decision space between the  $M$  hypothesis. This forces the sum of  $\pi_1$  to  $\pi_M$  to be one. This does not account for the fact that the total probability of all the hypotheses must sum to one, including  $\pi_0$ . To accomplish this, the calculated  $\pi_k$  are adjusted with the following equation:

$$\pi'_k = (1 - \pi_0)\pi_k. \quad (4.21)$$

If there is no analytical or empirical method of selecting a value for  $\pi_0$ , there are three potential alternate solutions. One would be to use the same assignment as ECEP,  $\pi_0 = 0.10$ , since it is the method being compared against. Another option is to investigate the actual value of  $\pi_0$ , but as mentioned earlier, this may not be possible. Alternatively, this section demonstrates analytically that the effect of changing the null hypothesis prior probability does not alter detection performance. To confirm this theory, a constant  $C$  is introduced.  $C$  acts multiplicatively with  $\pi_0$ , to adjust the null hypothesis value.

$$\begin{aligned} \pi'_0 &= C\pi_0 \\ \pi'_k &= (1 - C\pi_0)\pi_k \end{aligned} \quad (4.22)$$

Proposing different values for  $\pi_0$  can be accomplished by choosing two distinct constants,  $C_1$  and  $C_2$ . Computing the difference in weighting,  $\Delta W_k$ , gives insight into the impact of changing  $\pi_0$ .

$$\Delta W_k = W_k(C_2) - W_k(C_1) \quad (4.23)$$

$W_k(C)$  is the weighting term from equation (4.18) substituted with updated priors from equation (4.22). Combining and reducing with constants  $C_1$  and  $C_2$  gives an expression for the change in the  $k^{\text{th}}$  weighting term due to a change in the null hypothesis prior probability.

$$\Delta W_k = \frac{\sigma}{\theta} \ln \left( \frac{C_2 \pi_0}{(1 - C_2 \pi_0) \pi_k} \right) - \frac{\sigma}{\theta} \ln \left( \frac{C_1 \pi_0}{(1 - C_1 \pi_0) \pi_k} \right) \quad (4.24)$$

$$\Delta W_k = \frac{\sigma}{\theta} \ln \left( \frac{C_2(1 - C_1 \pi_0)}{C_1(1 - C_2 \pi_0)} \right) \quad (4.25)$$

Looking at equation (4.25),  $\Delta W_k$  is only a function of the constants and the original  $\pi_0$ . This signifies that  $\Delta W_k$  is independent of  $k$ , and it can be moved and grouped into the threshold  $\tau$ . The constant adjustment to the threshold will change the probability of false alarm. The false alarm probability can then be adjusted to match the  $P_f$  rate of the algorithm being compared against. This analysis demonstrates that the assignment for the value of  $\pi_0$  does not change the detection performance of the algorithm.

Combining the simulation study on  $\pi_0$  sensitivity along with the analytic derivation above provides good evidence that the choice of null hypothesis prior probability does not impact the detection capabilities of the algorithm.

### 4.3 Experiment Descriptions

In this section, the simulations and experiments used to test the algorithms developed in section 4.2.4 and 4.2.5 are described.

#### 4.3.1 *Simulation Description.*

To test the newly developed detection algorithm, simulated RSOs are analyzed. The primary reason simulated data is used is because a large number of space objects uniformly distributed across the pixels being tested are needed to test the algorithm. It is difficult to assess algorithm performance by analyzing collected telescope data of a single RSO. It is possible that the object is located in a specific sub-pixel position on the CCD and does not move throughout the collection period. In this case, the object may not represent how other randomly located PSFs appear in the data. Alternatively, another potential method is to analyze a large image of the sky, including stars, to gather a variety of locations and intensity levels. A drawback to this method is that many of the bright objects will be easily detectable to both algorithms, therefore it is necessary to define a range of intensities where the algorithms perform differently.

In this simulation, it is assumed that the RSOs occur with the prior probability that is present in an actual data collection. The ECUP algorithm has the maximum performance

advantage compared to ECEP if the true priors exactly match the priors determined through the correlation method. The priors may differ in an actual data collection if the assumption of a uniform distribution of objects does not hold, or other factors not included in the analysis affect the probability. In this analysis, the ideal performance, which does not include those factors, is tested. To give the simulated data the desired prior probabilities, a function is created to randomly select one of the hypotheses from the nine alternate hypotheses with the assigned weighting probabilities  $\pi_k$ . The optical model described in section 4.2.1,  $h(x, y)$ , is used to create the 9 candidate PSFs. As mentioned, this model includes several optical effects including a long exposure atmosphere model [34], optical aberrations, and spatial aliasing of the CCD pixels. The data model in equation (4.8) is used to combine the PSF with the background and noise model.

Two types of simulated data are needed, one with a RSO present and one without a RSO. Both data sets are needed to create the ROC curves in section 4.4.2. For this simulation, an object photocount of  $\theta = 300$  and background level of  $B = 400$  are used. In the case where no object is present,  $B$  is still 200, but  $\theta$  is set to zero. To add noise, the PSF and background is set to the mean of a Poisson random variable. Using a Poisson noise assumption implies that the signal is dominated by photon counting noise. Other factors, including dark current and read noise, are not significant contributors. The detection algorithm assumes that the received noise is Gaussian, as described in section 4.2.4. Figure 4.4 shows a flow diagram of the steps used to generate simulated data with and without an RSO present.

### ***4.3.2 Collected telescope data.***

The second experimental method used is collected SST data. This experiment uses the same data set described in Chapter 3, but focuses on a different portion of the data present in the images. This data was originally collected as an experiment to test how faint of an object can be detected by different detection algorithms. The SST is programmed to

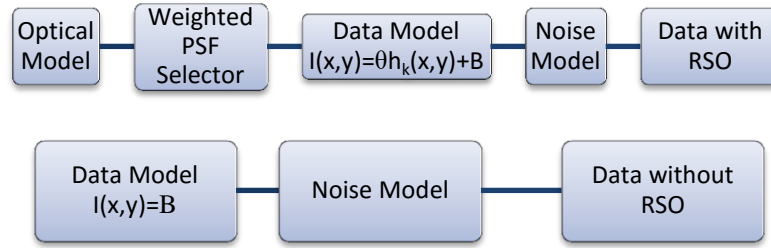


Figure 4.4: Flow diagram of process to (A) simulate data with an RSO present and (B) simulate data with no RSO present. Both data sets are needed to generate ROC curves.

track a communication satellite, ANIK-F1, as it enters eclipse. The resulting intensity loss causes the object to go from easily detectable to difficult to detect. This is used to test the performance of the UCEP algorithm.

In addition to the satellite of interest in each image, there are thousands of other objects, including stars and potentially RSOs. These stars and other space objects give a large quantity of varying intensity objects to test algorithms against. By processing a large portion of an image and totaling the number of detections, a metric of performance can be determined for each algorithm. Comparing the total number of detections with each algorithm for the same false alarm rate gives one method to compare the algorithms. All types of objects are treated similarly in this experiment, since both stars and RSOs appear as unresolved point source objects to the SST.

Each frame of collected SST data consists of 6144x4096 pixels, where each pixel contains 2x2 binned  $15\mu\text{m}$  square pixels. The data analyzed in this paper was collected on three nights 13-15 March 2012, referred to as night 073-075 respectively in the following discussions. As mentioned in the optical model description, each image is a long exposure collection. This implies that a long exposure atmosphere is present in the data.

Within each image there are areas where CCD arrays are aligned, and other areas of imperfection. To remove these edge effects, a subset of each frame is analyzed. An area consisting of 1024x1024 pixels is selected from each image. The same pixels are consistently used from each frame as the data is processed by the algorithm. Testing on each pixel is done by including a 16x16 window around the pixel being tested. Including the window gives enough samples to calculate accurate background statistics as well as enough pixels to capture both the PSF model and any potential space objects. In the next section, the false alarm probabilities are investigated.

#### ***4.3.3 Setting False Alarm Probability for Collected Data.***

It is important to ensure that both the ECEP and ECUP algorithms have the same probability of false alarm,  $P_f$ . The weighting term,  $W_k$ , is effectively changing the threshold and therefore the false alarm probability. Since the weighting term can be different for each hypothesis, the false alarm probability for the entire test needs to account for all potential hypotheses.

To accurately calculate  $P_f$ , two assumptions are made. The first is that SNR statistics calculated with equation (4.17) are Gaussian, which follows logically from the assumption that the received noise is Gaussian. The second assumption is that the probabilities of false alarm for each hypothesis are independent, and can be calculated separately. This assumption is applied to both the ECEP and ECUP algorithms. This assumption may overestimate the expected  $P_f$  if there is any dependence between hypotheses, but will do so for both the ECEP and ECUP algorithms. For the ECEP test, a base threshold of  $\gamma = 6$  is used to match previous algorithms and the SST program's threshold. The threshold for ECUP is then adjusted to match the  $P_f$  produced by the threshold of  $\gamma = 6$ .

To mathematically describe the method of calculating  $P_f$ , the term  $\mathcal{N}(\mu, \sigma)$  is defined to represent a Gaussian distribution with mean  $\mu$  and standard deviation  $\sigma$ . As described previously, the SNR in the ECEP algorithm is normalized to be a zero mean unit variance



Gaussian random variable. Since the ECUP algorithm is not normalized by  $\sigma_k$ ,  $\text{SNR}_k$  is no longer zero mean unit variance Gaussian.  $\text{SNR}_k$  has a mean of  $W_k$  and standard deviation of  $\sigma_k$  for each hypothesis.

$$\text{ECEP:} \quad X \sim \mathcal{N}(0, 1)$$

$$\text{ECUP:} \quad X_k \sim \mathcal{N}(W_k, \sigma_k)$$

Assuming independence between the hypothesis tests, the total false alarm can be calculated by summing the false alarm probability from each alternate hypothesis.

$$P_f = \sum_{k=1}^M 1 - p(X \leq \tau) \quad (4.26)$$

$p(X \leq \tau)$  is the Cumulative Distribution Function (CDF), and  $X$  is a random instance drawn from the Gaussian distribution described by either the ECUP or ECEP test. For the ECEP test, a value of 6 is used for  $\tau$ . To ensure the tests have the same probability of false alarm, a  $\tau$  needs to be found that gives equal  $P_f$  between the tests. Next, the results for the calculated prior probabilities and the number of binary detections are presented and analyzed.

## 4.4 Results

This section will investigate the results from both the simulated experiment and the data collected from the SST.

### 4.4.1 Decision Space Results.

The first important result is the calculated values for the prior probabilities  $\pi_k$ . To calculate these probabilities, the total number of each hypothesis present in the hypothesis assignment matrix  $\mathcal{H}$  is divided by the total number of sub-pixel positions tested. It is helpful to define the mathematical notation of an Iverson Bracket [70], where  $[\cdot]$  gives

a value of 1 is true or zero if false the following equation gives the value for the prior probabilities:

$$\pi_k = \sum_{\alpha=1}^{N_\alpha} \sum_{\omega=1}^{N_\omega} \frac{[\mathcal{H}(\alpha, \omega) = H_k]}{N_\alpha N_\omega}. \quad (4.27)$$

$N_\alpha$  and  $N_\omega$  are the size of the window being investigated in  $\alpha$  and  $\omega$ . Equation (4.27) is applied to each hypothesis assignment matrix. The three methods calculating the prior probabilities are shown in Figure 4.5.

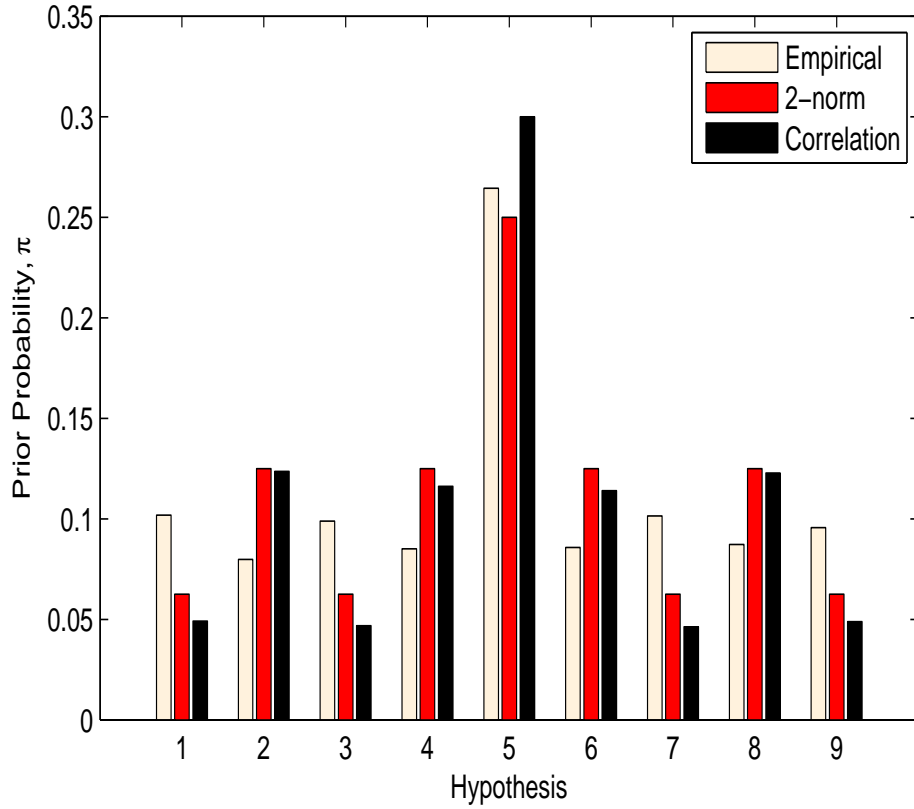


Figure 4.5: Comparison of three proposed methods: distance, correlation, and empirical based methods of assigning sub-pixel positions.

Figure 4.5 shows the prior probabilities for the three methods of segmenting the decision space. The first detail to note is that all three methods give similar prior probability values, with a maximum difference of approximately 10 percent. The general agreement between the priors gives a good indication that the methods accurately represent the true probabilities. The hypothesis at the center of the pixel,  $H_5$ , has the largest probability of occurring in all methods. The prior value ranges between 25 to 30 percent. Using a BHT, only one hypothesis is considered, and it is that the object is located directly in the center of a pixel. This analysis shows that using a BHT would only match well with 25 to 30 percent of potential objects, decreasing the ability to detect space objects.

The methods vary slightly in how they assign probability between the sides and corners. Distance and correlation metrics give higher probability to the sides, while the empirical method favors the corners. The empirical priors for the sides and corners are closer, while the other methods have a larger separation between them. These differences can be due to things not accounted for in the model that occur in measured data, such as non-uniform response across the CCD detector areas within pixel. In the empirical method, there is noise present in the data which is not present with the other methods.

Considering the three methods and their resulting priors, the empirical method of determining  $\pi_k$  values is used for analyzing collected data. This is because it is the closest match to how the ECUP detection algorithm actually operates. Additionally, it includes noise and other details that are not present in the other methods. The distance and correlation metrics also provide confidence that the empirical method is an accurate way to define prior probability since they generally agree. Table 4.1 summarizes important details about the physical locations of the hypotheses within a 30x30 pixel, prior probabilities with the empirical metric, and the resulting weighting values.

As Table 4.1 shows, probability is lower in the corners and sides, with the additional probability shifted to  $H_5$ , or the center pixel hypothesis. This implies that it is more likely

Table 4.1: The sub-pixel locations of the  $M$  hypotheses ( $\mu m$ ) along with the calculated priors  $\pi_k$  and weighting values  $W_k$  based on the empirical method.

	<b>H<sub>1</sub></b>	<b>H<sub>2</sub></b>	<b>H<sub>3</sub></b>	<b>H<sub>4</sub></b>	<b>H<sub>5</sub></b>	<b>H<sub>6</sub></b>	<b>H<sub>7</sub></b>	<b>H<sub>8</sub></b>	<b>H<sub>9</sub></b>
$\alpha, \omega$	-15,-15	-15,0	-15,15	0,-15	0,0	0,15	15,-15	15,0	15,15
$\pi_k$	0.10	0.08	0.10	0.09	0.26	0.09	0.10	0.08	0.10
$W_k$	1.78	2.57	1.78	2.56	3.75	2.56	1.78	2.56	1.78

for captured data to closely match the PSF generated, assuming the object is in the center of the pixel. Based on the empirical method,  $H_5$  hypothesis has approximately a 26 percent chance of occurring. The weighting values,  $W_k$ , from equation (4.18) which are calculated based on  $\pi_k$ , also provide interesting results. All of the weighting values are positive, and  $W_k$  is subtracted from the computed SNR. The newly computed SNR compared against the threshold will be lower than the ECEP test. This is counteracted by the new threshold  $\tau$  computed to ensure equal  $P_f$  rates. Although the weighting term is a linear effect on the SNR, calculating  $\tau$  is not linear. Considering these two competing effects, it is difficult to analyze how this will increase or decrease the number of RSOs detected. This is why collected telescope data detection performance is analyzed.

#### **4.4.2 Processing Simulated Data with MHT Algorithms.**

In this section, the detection algorithm is applied to simulated RSO data. As has been done in previous chapters, using a ROC curve gives insight to the detection behavior over a large range of potential  $P_f$  values. For the simulated data, the prior probabilities determined through the correlation metric were used. This is because the empirical method is not realistic, because there is no collected data to process. The following equation is used to generate ROC curves:

$$\max_k [\text{SNR}_k - W_k] \underset{H_0}{\overset{H_k}{\geq}} \Gamma + \tau. \quad (4.28)$$

$\tau$  is varied to give  $P_d$  and  $P_f$  pairs. The ability to correctly identify the sub-pixel hypothesis is not reported. If data containing a RSO is processed and any of the alternate hypotheses is selected, it is counted as a correct detection. Figure 4.6 shows an instance of ROC curves for both the ECEP and ECUP algorithms. To generate these ROC curves, 100 independent simulated images are analyzed. For every image, the SNR value and weighting factor  $w_k$  is calculated for all hypotheses. The maximum SNR value is selected and compared against the threshold  $\Gamma$ .

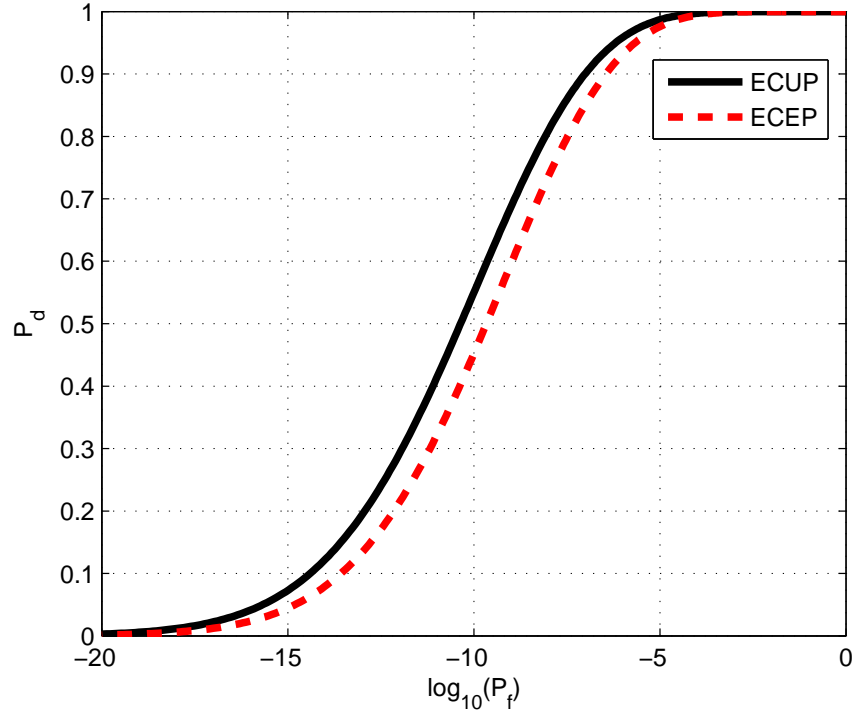


Figure 4.6: A single instance of a ROC curve for both the ECEP and ECUP algorithms. Simulated RSO and data with no objects present are needed to generate probability of detection and false alarm.

The ROC curves in figure 4.6 show up to approximately 10 percent of ECUP over ECEP. The algorithms perform similarly for relatively high and low false alarm probabilities. A typical detection algorithm would not operate in these regimes. The two curves in figure 4.6 represent a single instance of a simulation. To ensure that the ECUP algorithm detects more objects than the ECEP generally, the statistics of the ROC curve are investigated.

Defining  $\Delta_{P_d}(P_f)$  as the difference between  $P_d$  for the ECUP and ECEP algorithms gives the detection difference for the same false alarm probability.

$$\Delta_{P_d}(P_f) = \text{ECUP} - \text{ECEP} \quad (4.29)$$

Figure 4.7 shows a statistical comparison of detection performance between ECEP and ECUP algorithms. The  $P_d$  values in this figure were calculated with  $P_f = 1e - 10$ .

As figure 4.7 shows, there is a small but statistically significant difference in detection,  $\Delta_{P_d}$ , between the ECEP and ECUP algorithms. The red dashed line indicates the mean difference across 100 Monte Carlo simulations. The improvement in this simulation is approximately 5 percent. There are instances where  $\Delta_{P_d}$  is negative, or the ECEP outperforms the ECUP algorithm, but on average this is not the case. A 5 percent improvement across a large number of RSO could still be a significant number of objects. In the next section, the algorithm is used to process collected SST data.

#### ***4.4.3 Processing SST Data with MHT Algorithms.***

After assigning priors, the ECUP algorithm can be implemented on collected data. To accomplish this, the data described in section 4.3.2 is analyzed. This data contains many objects of different intensity levels, including many much greater than the current threshold. These objects will be easily detectable with both the ECEP and ECUP algorithm. The difference in detection is the RSOs that are close to the detection threshold. Objects

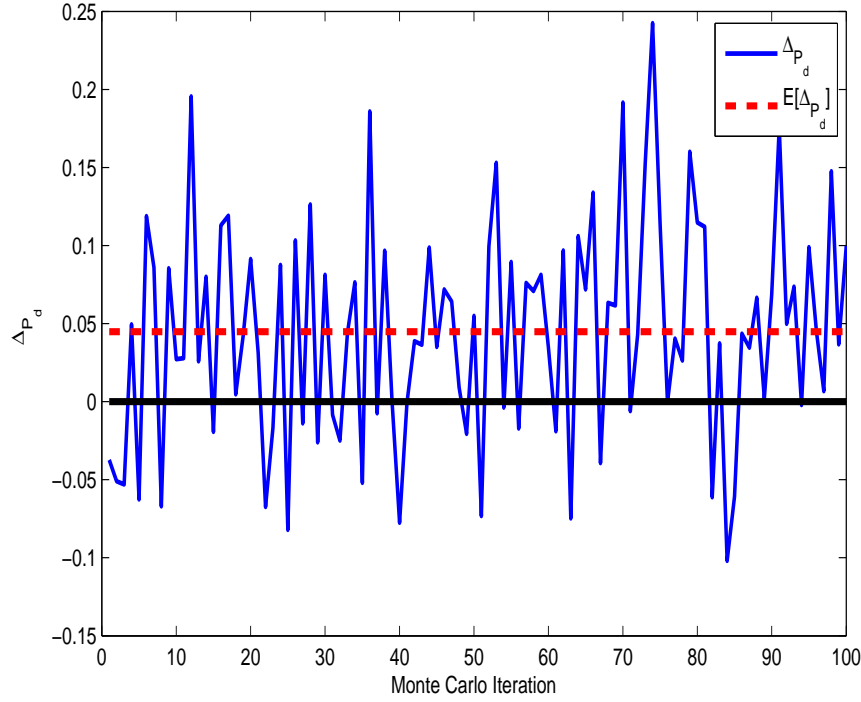


Figure 4.7: Statistical comparison of ECEP and ECUP algorithms over 100 monte carlo iterations.  $P_d$  values for both algorithms are found for a false alarm probability of  $P_f = 1e - 10$ .

much brighter than these will easily be detected with both algorithms. Space objects much dimmer than the threshold will not be detected by either algorithm.

There are several potential methods for reporting the change in detection performance. Using a probability of detection,  $P_d$ , at a specified false alarm rate  $P_f$  is a commonly used metric. Another method is reporting  $P_d$  across a large range of potential  $P_f$  values, also known as a ROC curve, typically provides insight. In this chapter, the number of additional binary detections at a specified false alarm is reported. The difference in the number of detected objects between ECEP and ECUP is defined as  $\Delta_o$ :

$$\Delta_o = \text{ECUP} - \text{ECEP}. \quad (4.30)$$

The total number of binary detections includes all alternate hypotheses where an object is considered present,  $H_1$  through  $H_9$ . Using the calculated  $P_f$  value of  $8.5\text{e-}09$ , and  $\tau = 6$  for ECEP and  $\tau = 0.98$  for ECUP, the SST data is analyzed. Figure 4.8 demonstrates a small subset of a frame of data processed with both the ECEP and ECUP algorithms. In the example shown, one additional binary detection is observed.

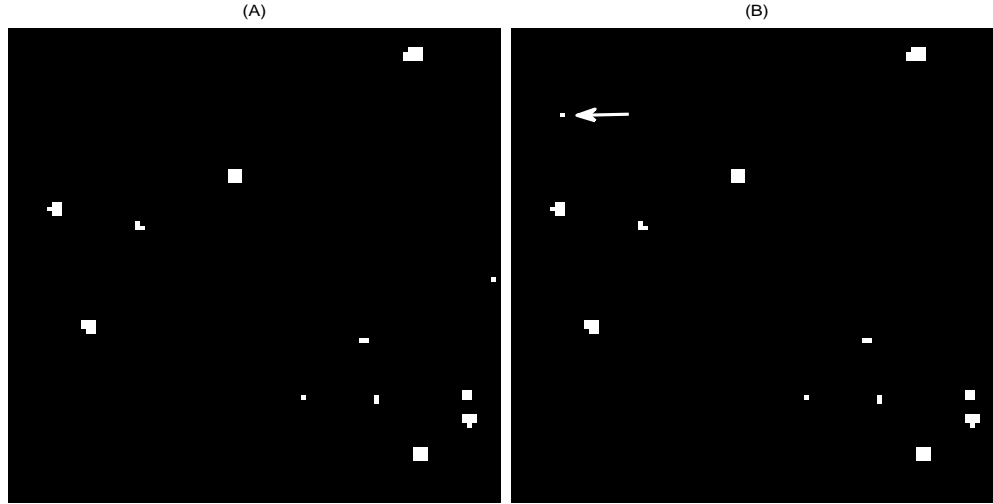


Figure 4.8: A sample subset of SST data processed with (A) the ECEP algorithm and (B) the ECUP algorithm. In this example, one additional detection is observed.

Figure 4.9 demonstrates the difference in the number of binary detections between ECUP and ECEP.

$\Delta_o$  ranges from 61 additional binary detection to 4 less detections on the days and frames processed. Across all three nights processed there were, on average, more detections with ECUP. For each frame, the total number of detections changes as objects enter and exit



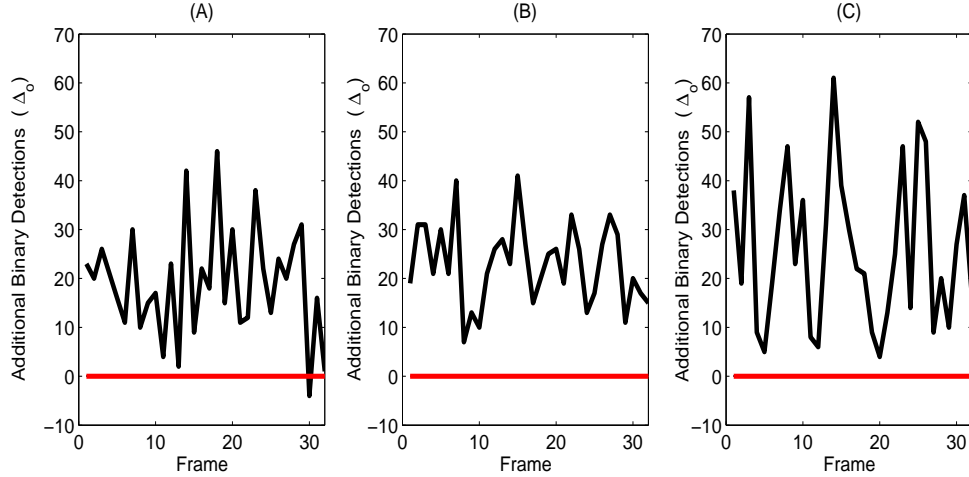


Figure 4.9: Difference in number of binary detections,  $\Delta_o$ , over 32 sample frames from data collected on nights (A) 073, (B) 074, and (C) 075.

the frame, noise spikes occur, and space objects change intensity.  $\Delta_o$  stays fairly consistent throughout these changes.

There is an obvious increase in binary detections present in the sample data analyzed, but it is important to ensure that this instance is not a random occurrence. One method is to perform a significance analysis on the mean. Looking at a paired T statistic test can indicate if there is truly a difference in means, and which is greater [71]. Night 073 has a paired T test statistic value of 9.07. This signifies it is highly likely that ECUP is detecting more objects on average than ECEP. Large T statistic values also occur on nights 074 and 075, 15.62 and 9.49 respectively.

Additional information can be gleaned from investigating the distribution of  $\Delta_o$  data. Figure 4.10 shows a histogram for  $\Delta_o$  across all three nights of the SST data processed.

The distribution of the additional number of detections appears Gaussian. Across all of the processed data,  $\Delta_o$  has a mean of 22.73 and a standard deviation of 12.65. Table 4.2

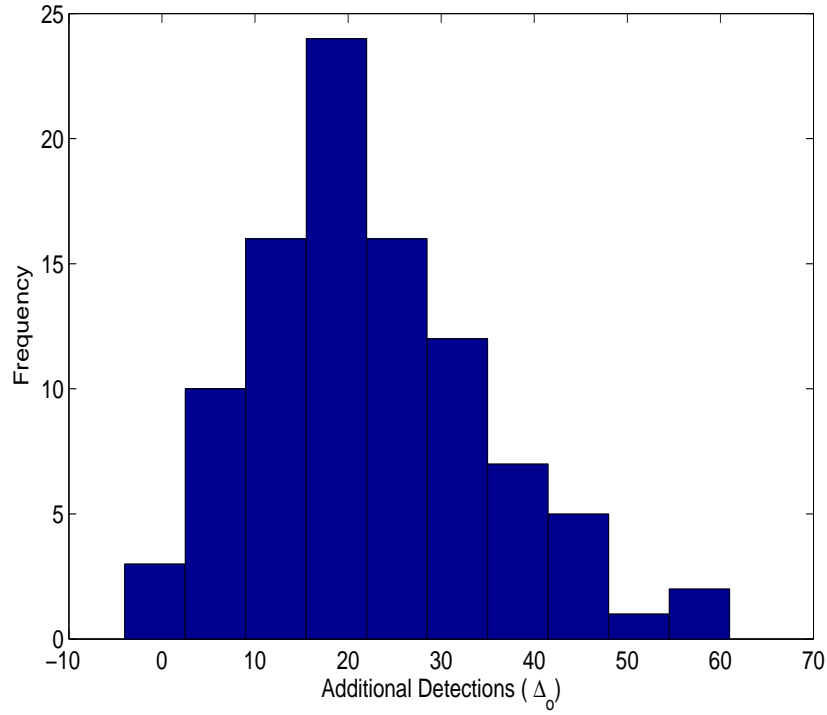


Figure 4.10: Combined histogram for  $\Delta_o$ , the number of additional binary detections with ECUP algorithm. All three nights analyzed 073-075 are included.

shows the average number of additional detections and the standard deviation of the ECUP algorithm for individual nights.

Table 4.2: Average number of additional binary detections by ECUP,  $\bar{\Delta}_o$ , and standard deviation,  $\sigma_{\Delta_o}$ , for three nights 13-15 March 2012.

	Night 073	Night 074	Night 075
$\bar{\Delta}_o$	26.13	22.97	19.10
$\sigma_{\Delta_o}$	16.30	8.32	11.38

One noticeable result from Table 4.2 is that the largest  $\Delta_o$  occurred on night 073. This was the night used to generate the priors with the empirical method. This signifies two interesting details. The first is that the empirical priors do not necessarily need to be recomputed frequently. The empirical priors are able to achieve an improvement for three consecutive nights without adjustment. The values do decrease slightly between nights. Several factors including atmospheric conditions may cause the priors to change slightly between collections. There may be an optimal update rate for priors that takes these factors into account, but this is not further investigated in this paper.

The subset of frames analyzed for this chapter are not the full image frames. Increasing the number of pixels being tested would also increase  $\Delta_o$ . A total of 24 of the 1024x1024 frames are in the full frame data. Applying the averages determined in the small frame would give approximately 458-627 additional binary detections on average.

#### **4.5 Full Frame Implementation**

An important consideration for implementing an algorithm is how long it takes to process each frame of data. If the algorithm can not be completed in real time, or the time between when each image is captured, the output of the algorithm would be constantly falling behind the captured data. Some catch up can be accomplished when data collections are not being performed. This limits the ability to adjust collections based on observations during collection.

In section 3.5, a full frame implementation of the UCEP algorithm is discussed. Similar methods can be used with the UCEP algorithm. The main difference between full frame implementation of UCEP and ECUP algorithms is exponential function. Unlike the UCEP algorithm, which is not a linear algorithm, the ECUP algorithm is able to be reduced to SNR calculation, with an additional weighting term. This weighting term,  $W_k$ , can be precomputed based on the background statistics, PSF being considered  $f_k(x, y)$ , and the assigned priors. These terms do not add a significant processing requirement.

## 4.6 Conclusions

In this chapter, the assignments of a priori probabilities in a MHT are investigated. This is achieved through developing an algorithm and testing it against simulated and collected SST data.

To analyze the simulated data, a correlation metric between the simulated RSO data  $D(x, y)$  and the modeled sub-pixel positions  $T_{\alpha, \omega}(x, y)$ , is used to assign prior probabilities for the  $M$  hypotheses. It is shown with a sensitivity analysis that the null hypothesis does not significantly impact the detection ability, and a value of 0.10 is used to match previously developed algorithms. These prior probabilities are implemented in an ECUP MHT. The derived algorithm is used to analyze simulated RSOs. The algorithm used for this research contains a hypothesis dependent threshold. ROC curve analysis shows that the ECUP algorithm has a greater  $P_d$  than the ECEP algorithm for a large range of  $P_f$  values. At a relevant false alarm level of  $P_f = 10^{-10}$ , ECUP shows an average improvement of approximately 5 percent when tested over 100 monte carlo simulations.

When tested against collected SST data, this research demonstrates that for certain applications it may be beneficial to use an ECUP MHT algorithm. It is shown that with high statistical confidence the ECUP algorithm on average has more detections than an ECEP algorithm performed on the SST data. For the small subset of the frames analyzed approximately 19-26 additional detections, which translates to 458-627 additional detections on average for full frame data. These detections are most likely threshold objects that are difficult for currently proposed detection algorithms to detect. Finding these threshold objects will provide additional information for tracking and characterization, in turn increasing SDA capabilities with the optical system.

In addition, a method of using empirical observations of representative data is developed to form a model for a priori probabilities. Distance and correlation metrics were also considered and result in similar distribution of prior probabilities.

The ECUP algorithm assumes Gaussian received noise in this paper. In the future, removing the Gaussian assumption may detect additional space objects, if the received noise is not truly Gaussian. Additional methods may also be combined to potentially improve detection performance even further. For example, using a unequal-cost and an unequal-prior probability approach may improve over a unequal-cost equal-prior test.

In the ECEP MHTs, the threshold is considered constant for each hypothesis. As a result, the modeled intensity is effectively different for each hypothesis, and is dependent on the distribution of the PSF. This assumption is changed in this paper for the ECUP algorithm. This assumption can be removed in a future ECEP test, and may provide interesting research opportunities and advancements.

Another consideration is how including unequal-priors may effect the ability to translate the detected objects into accurate tracking and orbit determination. The ECUP algorithm takes into account the probability of the alternate hypotheses, each of which corresponds to a sub-pixel position. The sub-pixel information gathered from performing a ECUP test may lead to improved sub-pixel position, and in turn more accurate tracking of detected RSOs.

## **V. Characterizing Point Spread Function fluctuations to improve Resident Space Object detection**

In the previous chapters, this dissertation examines Bayes Risk algorithms based on the assumption that the received data contains Gaussian noise. This chapter focuses on developing an accurate combined noise statistics model for noise present in a collected telescope image. The specific goal of this chapter is to determine a more accurate model for the observed noise in a PSF. By using this new model and the corresponding detection algorithms, there will be improved detection performance in the optical systems being considered. As mentioned previously, the PSF is of interest due to the fact that all objects of interest can be considered point source objects.

Building a detection algorithm based on a more accurate or complete model of noise statistics in a PSF should theoretically result in an increase in the ability to detect space objects with that optical system. The number of additionally detected objects and the complexity of the resulting algorithm are important factors in determining the feasibility of any newly proposed detection algorithm.

This chapter is organized into four main sections. In section 5.1, relevant background and methodology in optical modeling, detection theory, atmospheric effects, and relevant Probability Density Functions (PDFs) are detailed. Section 5.2 describes the simulation experiment used to analyze the distributions and detection performance. Section 5.3 discusses the results and analysis, and section 5.4 presents the conclusions on the results reached.

### **5.1 Methodology**

All objects of interest in this research, due to their relative size and distance from the observation plane, appear as point sources to the telescope. The PSF of an optical system

is the response of the system to an impulse, or point source. In the case of RSO detection, each object is an observed PSF.

The noise present in an image captured through a telescope is a combination of several potential noise sources. Traditionally, SDA detection algorithms have assumed a Central Limit Theorem justification and used a Gaussian PDF to describe the distribution of the received data. This implies that the combination of all of the noise sources present in the system result in an overall Gaussian PDF within the received data. Multiple research efforts have looked at creating detection algorithms based on the noise in the received data not being Gaussian [22, 35]. In these cases it is assumed that the received noise is dominated by Poisson noise, and other sources do not contribute significantly.

One example of building a detector based on Poisson noise is when the dominant source of noise in the received data is assumed to be the random arrival time of photons [22]. The author states this can be achieved through a very low noise CCD in a low intensity collection environment. It is found that this assumption reduces similarly to Gaussian if there is a flat background. In other words, if the detection algorithm does not have a known star map for use by the detection algorithm, the Poisson and Gaussian approaches perform similarly. Similar results, also assuming a Poisson distribution, have been demonstrated to perform comparably in collected telescope data at the Air Force Institute of Technology (AFIT) [35].

Unlike to these two non-Gaussian methods, this chapter will account for two of the main phenomena present in data collection, and combine them into a single noise model. These phenomena are atmospheric effects and photon counting noise. It is well understood that noise due to random photon arrival times follows a Poisson distribution [17]. The impact of the atmosphere and the fluctuations it causes in received intensity are not as clearly defined.

### 5.1.1 Optical Model.

As in Chapter 3, an optical model of the telescope is needed to generate the PSFs used in the detection algorithm. There are two main differences in the optical model presented here: one is the method for simulating the atmospheric effects and the second is the exclusion of lens aberrations. This implies that the optical system being modeled is either diffraction limited or that the lens aberrations do not change significantly over the time scale of interest. The PSF of an optical system,  $h_{\text{opt}}(x, y)$ , can be found by the following relation [34]:

$$h_{\text{opt}}(x, y) = |\mathcal{F}\{P(m, n)\}|^2 \quad (5.1)$$

where  $x, y$  are spatial distance pixel coordinates in the detector plane, and  $m, n$  are pixel coordinates in the pupil plane.  $P(m, n)$  is a pupil function that mathematically describes the effect of the pupil on incoming light and  $\mathcal{F}$  is a two-dimensional Fourier transform. In a diffraction limited optical system consisting of a perfect lens or mirror, the pupil function consists of only the geometry of the pupil,  $P(m, n) = A(m, n)$ , and contains no other phase distortions.  $A(m, n)$  is an amplitude function that is one or zero, depending on if light is able to pass through the pupil at a specific  $m, n$  pixel location.

In a non-ideal imaging system, imperfections in the lenses or mirrors cause phase distortions to any light passing through the optics. These distortions are modeled as phase fluctuations to the amplitude function [34].

$$P(m, n) = A(m, n) \exp[j\theta_o(m, n)] \quad (5.2)$$

For this simulation, it is assumed that the imaging system is ideal. This assumption implies that the phase function is a constant function of spatial coordinates  $m$  and  $n$ . This is justifiable due to the fact that the phase distortions caused by the optics are generally constant in time and these distortions will not impact the peak intensity as a function of



time. The lens aberrations change the shape, distribution, and intensity of the PSF, but do not generally change significantly over the observation time.

At this point, the optical model represents a field entering the pupil of an optical system, but has not accounted for the effects of propagation through the atmosphere. To randomly generate a phase screen with statistics that accurately represent the atmosphere, a Zernike method is used [58]. Although there are other accepted models for generating random phase screens, including the frequently used Fourier Transform approach [57], they are not addressed in this chapter.

One benefit to using the Zernike method is that the Zernike polynomials can be used to simulate mirror aberrations. Using Zernike coefficients for multiple functions also helps to reduce processing time. The Zernike method has a less difficult time reproducing the low frequency effects of the atmosphere, such as tilt, than the Fourier Transform method. The Zernike method does not have the same low frequency issues. The low frequency effects have the most power, and are a dominant source of error in most telescopes. Additionally, high frequency aberrations do not have a large impact on the PSF in undersampled systems, such as the telescopes discussed in this dissertation. High frequency changes will be filtered by the relatively large CCD pixels. In this chapter, a total of 15 Zernike polynomials are used to represent the random aberrations present in the atmosphere. Including a higher number of Zernikes is not found to have a significant impact on the PSF, and as a result, the determined noise model.

The atmosphere acts like a random process to any light that travels through it. The result is a propagation path for the light that has varying indices of refraction in space and time,  $n(x, y, z)$ . This random process causes distortion in the wavefront,  $\theta_a(x, y)$ , and can be represented as a sum of a set of orthonormal Zernike polynomials,  $Z_j(x, y)$ .

$$\theta_a(m, n) = \sum_j b_j Z_j(m, n) \quad (5.3)$$

where  $b_j$  are the weighting coefficients for the  $j^{\text{th}}$  polynomial. In this case,  $b_j$  are random variables that represent the amount of each type of distortion present in the atmosphere that the light is propagated through. The coefficients are zero mean random variables, implying that there is no tendency for any of the coefficients or aberrations to be skewed in one direction or another. The variance of the Zernikes due to a Kolmogorov spectrum, as described in chapter 2, are derived in [62]. These variances form a covariance matrix,  $C$ . To utilize this covariance matrix to generate coefficients with the correct statistics, a Cholesky factorization is performed on the covariance matrix  $C = \Phi\Phi^T$ . Defining  $\vec{n}$  as a Gaussian random vector with zero mean and unit variance, another vector  $\vec{b} = \vec{n}\Phi$  based on the Cholesky factorization of the covariance is formed. This vector  $\vec{b}$  accurately represents the Kolmogorov statistics present in the atmosphere. This can be shown with the following mean and variance equations:

$$E[\vec{b}] = E[\vec{n}\Phi] = \Phi E[\vec{n}] = 0 \quad (5.4)$$

$$E[\vec{b}\vec{b}^T] = E[\Phi\vec{n}\vec{n}\Phi^T] = \Phi E[\vec{n}\vec{n}] \Phi^T = C. \quad (5.5)$$

The vector  $\vec{b}$  is zero mean and has covariance of  $C$ .  $\vec{b}$  is then used as the weighting coefficients for the Zernike polynomials described in equation (5.3). These atmospheric aberrations are then included in the pupil function, along with the aperture and lens aberrations.

It is important to note that the phase screen,  $\theta_a(m, n)$ , is one instance of atmosphere experienced by the object. As mentioned previously, the phase screen representing lens aberrations  $\theta_o(m, n)$  is constant over  $m$  and  $n$ . To create images representing a non-instantaneous integration time, additional phase screens and their resulting PSFs need to be generated. This process is described in section 5.2.1.

### 5.1.2 Detection Theory.

One commonly used detection algorithm is a Log-Likelihood Ratio (LLR). Assuming an Equal-Cost Equal-Prior (ECEP) model, a Bayes risk criterion for a BHT can be described with the following LLR [25]:

$$\text{LLR} = \log \left( \frac{p(D|H_1)}{p(D|H_0)} \right) \underset{H_0}{\overset{H_1}{\gtrless}} \tau \quad (5.6)$$

$H_1$  is the hypothesis that a RSO is present in the image and  $H_0$  is the hypothesis that there is no RSO present.  $\tau$  is the threshold that sets the acceptable false alarm rate.  $D$  is the received data, which can be either the photon count in a single pixel or across multiple pixels,  $D(x, y)$ , depending on if a point detector or matched filter detector is being used. Algorithms for the detection of space objects have been developed for both point detectors [16] and matched filter-based detectors [22, 24] under different received noise distribution assumptions. The conditional probabilities  $p(D|H_0)$  and  $p(D|H_1)$  are the probability of the received data given that the specified hypothesis is true. The received data is modeled with the following equation:

$$D(x, y) = \theta h_n(x, y) + B \quad (5.7)$$

$D(x, y)$  is the received intensity at the CCD before photon counting noise is included. The normalized PSF  $h_n(x, y)$  is the optical PSF,  $h_{\text{opt}}(x, y)$ , normalized to sum to one. The variable  $\theta$  is the intensity of the object being investigated. In the case where an object is considered present,  $H_1$ ,  $\theta$  can be any positive non-zero integer. Under the hypothesis where no object is present,  $\theta$ , is zero and the model reduces to a constant background level  $B$ . The conditional probability of data given  $H_1$ ,  $p(D|H_1)$ , is the distribution of interest to this research. The distribution fit theory is described in section 5.1.3 and analyzed in section 5.3. The probability of the data given  $H_0$ ,  $p(D|H_0)$ , is considered to be Poisson, due to the

fact that the dominant noise source present under this hypothesis is photon counting noise [17]. The Poisson conditional probability can be expressed with the following equation:

$$p(D_B|H_0) = \frac{B^{D_B} e^{-B}}{D_B!}. \quad (5.8)$$

$D_B$  is the number of background photons received, and  $B$  is the expected number of background photons.

### 5.1.3 Received Noise Distributions.

As mentioned previously, detection algorithms in electro-optical telescopes focus primarily on two types of PDF for noise statistics, Gaussian [24, 56] and Poisson [16, 35]. To justify these distributions, limiting assumptions are made. The assumptions made can degrade or limit the performance of the detection algorithm and the capabilities of the telescope system. Often these noise assumptions demonstrate a trade-off between computational complexity and increased performance. For example, one benefit of a Gaussian noise assumption is that it allows for easier computation of the SNR. This may potentially result in reduced performance, if the received data is not truly Gaussian.

The model proposed in this chapter combines two important effects into a mixed distribution to attempt to achieve a closer match to the true measured noise distribution. In previous research efforts [36, 56], a Gamma distribution is investigated, both theoretically and analytically, to describe the statistics of intensity fluctuations in the atmosphere. There have been other proposed distributions, including Log-normal and Beta [56], but these are not explored in this chapter.

The derivation of the mixed PDF models begins with the assumption that the underlying intensity fluctuations are Gamma distributed. Once the perturbed field from the space object reaches the CCD and is captured, the photons experience Poisson counting noise. Mathematically this combination of distributions is achieved by combining the

continuous Gamma function with the discrete photon counting noise present, leading to a negative binomial distribution for  $p(D|H_1)$  [72]:

$$p(D_s|H_1) = \frac{\Gamma(M + D_s)}{\Gamma(M)\Gamma(D_s)} \left(1 + \frac{S}{M}\right)^{-M} \left(1 + \frac{M}{S}\right)^{-D_s} \quad (5.9)$$

$\Gamma$  is the Gamma function and  $M$  is the number of degrees of freedom.  $M$  represents the amount of scintillation present in the received data. A value of one for  $M$  gives the largest scintillation effect. Alternatively, larger  $M$  values decrease the amount of scintillation present in the received data.  $S$  is the intensity of the RSO of interest, and  $D_s$  is the number of photons received from the target object.

The scintillated received data described to this point does not include the total number of photons captured. In addition to photons for the object being observed, background photons from ambient light sources will also be captured in the data. The total number of photons received by the CCD,  $D$ , is a combination of the number of photons from the object and the number of photons from the background:  $D = D_s + D_B$ . Assuming that background and scintillated light from RSO are statistically independent, the two sources can be combined into a joint Probability Mass Function (PMF). To achieve a marginal PMF, the joint PMF is summed over the number of photons received from the object  $D_s$  under the  $H_1$  hypothesis:

$$p(D|H_1) = \frac{e^{-B} B^D}{\Gamma(M)} \left(1 + \frac{S}{M}\right)^{-M} \sum_{D_s=0}^D \frac{\Gamma(M + D_s)}{\Gamma(D_s)} \left(1 + \frac{M}{S}\right)^{-D_s} \frac{B^{-D_s}}{(D - D_s)!} \quad (5.10)$$

There are two main challenges presented by the mixed PMF shown in 5.10. The first is that the conditional probability given  $H_1$  is not easily reduced to a simple PDF. Additionally, when combined to get a LLR, the new method does not reduce to a sufficient statistic similar to Gaussian and Poisson. Instead of a simple sufficient statistic such as SNR found through a correlation of the data and expected PSF, the probability needs to be calculated directly. Secondly, the distribution relies on two parameters that are not

immediately apparent from the received data: the coherence parameter  $M$  and the true object intensity  $S$ . These parameters need to be estimated from the data. Methods of determining these parameters are described in section 5.3.1.

## 5.2 Simulation Description

In this section, a simulation is developed to generate realistic data that would model the received data from a telescope observing a RSO. The model accounts for both scintillation from the atmosphere and photon counting noise effects. The simulated data serves two purposes in this research. The first is to analyze the intensity fluctuations present in the PSF, and determine which PMF is the best fit. After the most appropriate distribution fit has been determined, the RSO data is processed with the detection algorithm developed in the previous section to evaluate the performance against traditionally used detection algorithms.

### 5.2.1 *Evolving Phase Screen Over Time.*

The weighting vector coefficients,  $\vec{b}$ , developed in the previous section accurately represent the statistics of the atmosphere at one instant in time. To simulate any non-instantaneous and measurable period of exposure time, the behavior of the atmosphere over time is essential. It has been shown that unless there are very strong winds, or a long time between observations, the statistics of the atmosphere are correlated over time [58]. This implies that over a short period of time, the optical system is likely to see correlated phase errors,  $\theta_a(m, n)$  across the pupil. It is important to account for this effect in order to properly simulate the behavior over time. To account for the correlated atmosphere, each of the  $j$  Zernikes modeled have a corresponding correlation term,  $R_j$ . Taylor's frozen flow hypothesis is used to create this model of correlation. In Taylor's Frozen Flow, a constant wind blows a frozen atmosphere across the pupil [48]. This correlation for the  $j^{th}$  Zernike is a function of the separation between two points in time along with wind velocities and seeing parameter  $r_o$ .

$$R_j(\Delta t) = E[b_j(t_1)b_j(t_2)] \quad (5.11)$$

Examining the expected value of the coefficient at these two times shows how correlated each new Zernike at time  $t_2$ ,  $b_j(t_2)$ , will be to the previous at time  $t_1$ ,  $b_j(t_1)$ . The correlation for a specific time separation,  $\Delta t = t_2 - t_1$ , is found numerically through the structure function of the atmosphere. As screens evolve over time, the weighting coefficients are no longer zero mean, and have a variance of  $\sigma_{a_j}^2$ . A new mean is calculated based on the previous values of each coefficient  $b_j$ , and the correlation  $R_j(\Delta t)$ .

$$\hat{\mu}_j = b_j \frac{R_j(\Delta t)}{\sigma_j^2} \quad (5.12)$$

The variance of the next instance of Zernike coefficients is also a conditional variance. The variance is based on the unconditioned variance of the Zernike and the correlation for the specified time separation of  $\Delta t$ .

$$\hat{\sigma}_j = \frac{(\sigma_j^2)^2 - R_j^2(\Delta t)}{\sigma_j^2} \quad (5.13)$$

A new vector of coefficients,  $c_j$ , is formed from the conditional mean and variance in equations (5.12) and (5.13). These coefficients are also Gaussian distributed random variables, but with a mean  $\hat{\mu}_j$  and variance  $\hat{\sigma}_j$ .

$$c_j \sim \mathcal{N}(\hat{\mu}_j, \hat{\sigma}_j) \quad (5.14)$$

The variance in the fluctuations is related to the ratio between the diameter of the aperture of the telescope,  $d$  and Fried's Atmosphere coherence diameter,  $r_o$  [17]. This ratio,  $d/r_o$ , determines the amount of each type of phase error present.

### 5.2.2 Final System Model and Implementation.

To finalize the model for the simulation, the telescope and random phase screen simulations are combined. There are different approaches to simulating propagation

through the atmosphere and placement of the phase screen. Figure 5.1 demonstrates two distinct methods of simulation.

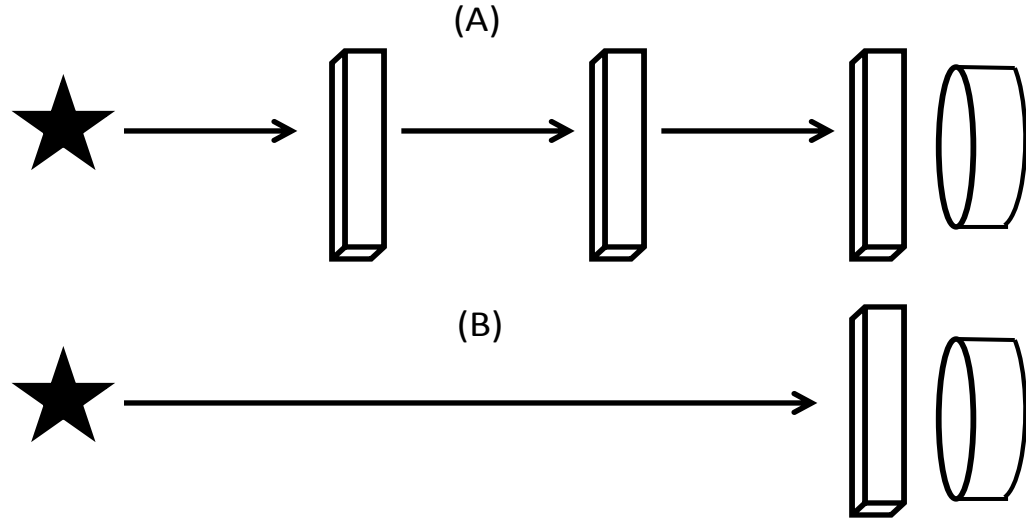


Figure 5.1: Diagram of two potential different atmosphere propagations. In (A) a multiple step propagation is demonstrated, in (B) a single phase screen directly against the pupil is demonstrated.

In (A), the field is propagated through multiple phase screens placed along the propagation path. Each screen may contain different statistics that represent the section of atmosphere around that location. This method allows for more complicated interactions between the field after each new simulated section of atmosphere. In (B), the phase screen,  $\theta_a(x, y)$ , is simulated to be a thin phase screen placed directly against the pupil of the telescope. Generally this method may not accurately represent the atmospheric effects, unless an isoplanatic assumption is valid. The isoplanatic assumption implies that light from any part of an object of interest experiences the same section of atmosphere. To ensure this is a valid assumption, a model for the atmosphere is needed.



One popular model of refractive-index structure constant  $C_n^2$  is Hufnagal-Valley<sub>5/7</sub>. This structure constant is a measure of the strength of fluctuations in the refractive index. Under normal vertical viewing conditions, it gives an isoplanatic angle of  $7\mu\text{rad}$  [36]. The isoplanatic angle is an angle over which the isoplanatic assumption can be considered valid. Most SDA search telescopes have a large field of view, much much larger than  $7\mu\text{rad}$ , so an isoplanatic assumption is not valid when simulating an entire field of view. However, since only a single point object is being simulated and investigated to generate a PSF, an isoplanatic assumption can be accurately made. For example, a 150m object in GEO would still only represent an angle of  $4.2\mu\text{rad}$ , which is less than the isoplanatic angle in the Hufnagal-Valley model. Now that there is a model for the phase screens,  $\theta_a(m, n)$ , these simulated phase errors created from equation (5.14) are added to the pupil function from equation (5.2) to give an updated pupil function,  $P_a(m, n)$ , that is used to generate the PSF.

$$P_a(m, n) = A(m, n) \exp [j\theta_o(m, n)] \exp [j\theta_a(m, n)] \quad (5.15)$$

This model now accounts for the first phenomenon being considered, the scintillation due to the atmosphere. The next step is to add in the background light as shown in equation (5.7). Finally, photon counting Poisson noise is added on top of the expected image  $D(x, y)$  to give the final received data.

The optical model, random phase screens, and data analysis are processed in MATLAB. All phase screens are generated with a separation of  $\Delta t = 1\text{ms}$ . To simulate a desired exposure time,  $1/\Delta t$  correlated phase screens are used and each is put through the combined model. Since a non-instantaneous exposure time is desired, it is necessary to evolve the Zernike polynomials coefficients to generate each subsequent phase screen, as described in section 5.2.1. In each new Monte Carlo simulation, an independent phase screen is generated. Next, the remaining  $(1/\Delta t - 1)$  phase screens are generated based on the statistics of the first screen and the correlation of Zernike polynomials. Each of these

screens are then placed in the optical model to create PSFs. The resulting PSF images are averaged and normalized to create a single simulated PSF. This PSF is the result of the desired exposure time, optical system, and atmospheric conditions.

### 5.3 Results and Analysis

To demonstrate that the received data more accurately matches the newly developed mixed PDF than traditional assumption, the mixed PDF is compared against both Gaussian and Poisson distributions. An error metric is used to determine the best fit between the simulated received data and the potential distributions for various atmospheric conditions.

#### 5.3.1 Distribution Matching.

The first step in analyzing the distribution fits is to create a histogram that represents the PDF of the received data. This PDF can then be compared against the theoretical PDF of the potential distributions. The center pixel intensity values in the PSF are noted across 1000 independent Monte Carlo iterations and then normalized. An important aspect in fitting the distributions is determining the correct parameters for each PDF based on the received intensities. The Gaussian is found by investigating the mean and standard deviation of the received data. The Poisson is described completely by the mean. The mixed PDF depends on four parameters:  $M$ ,  $S$ ,  $B$ , and  $D$ . The value of  $D$  is the simulated data of the pixel being investigated. The value of  $M$  is found by providing the true values for  $S$  and  $B$ , then selecting the  $M$  that provides the best fit. The value of  $M$  is a function of atmospheric conditions and the integration time  $T_s$ . Once the fit for  $M$  is found, the values for  $S$  and  $B$  are estimated from the data.

Each PDF is evaluated against the received PDF at the histogram bin locations. The difference between PDFs is considered the error between simulated data and the candidate PDF. Each vector of errors is then combined into a total RMSE,  $E_{\text{RMS}}$ :

$$E_{\text{RMS}} = \sqrt{\sum_{l=1}^{N_b} \frac{(p(l) - D(l))^2}{N_b}} \quad (5.16)$$

where  $N_b$  is the number of buckets, or places in the histogram that the PDFs are being compared against.  $l$  is the bin locations,  $p(l)$  is the value of the PDF being investigated at bin  $l$ , and  $D(l)$  is the simulated data value evaluated at the histogram bin  $l$ . Figure 5.2 shows the  $E_{\text{RMS}}$  values for the three candidate PDFs considered versus the seeing parameter,  $r_o$ .

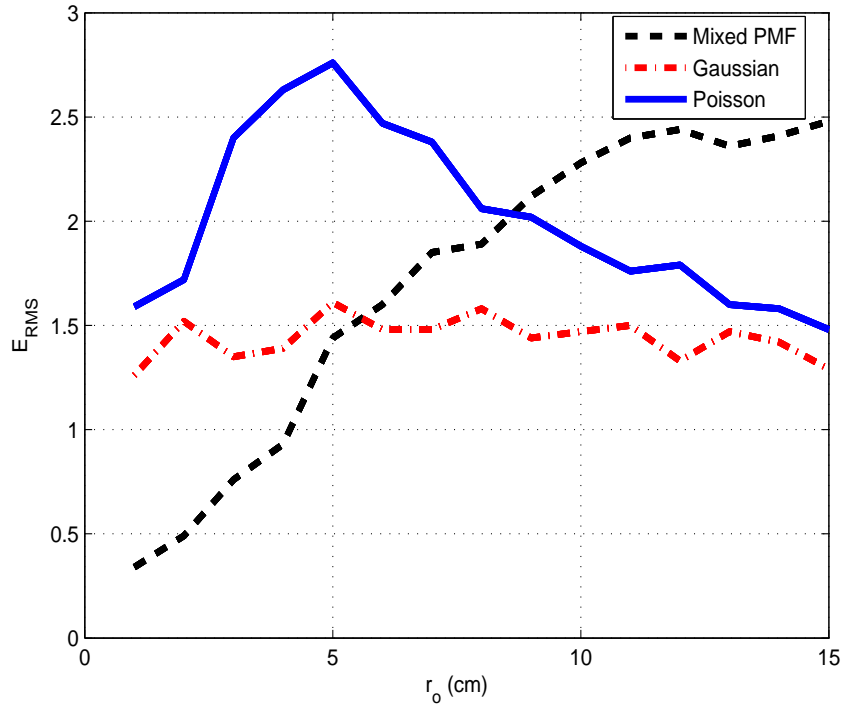


Figure 5.2: Error between candidate PDFs and received intensity fluctuations.  $E_{\text{RMS}}$  is calculated for a variety of seeing values,  $r_o$

The error between the mixed distribution and the simulated data is smallest for  $r_o$  values less than 6 cm. After 6cm, the Gaussian PDF more closely matches the received data. Physically this means that during conditions of increased turbulence, or lower  $r_o$ , the

temporal scintillation will be more prominent. There are several locations where survey telescopes are located that routinely experience  $r_o$  values of less than 6cm, indicating that it is not unrealistic to expect these conditions. It is found that the distribution match is largely a factor of the seeing parameter,  $r_o$ , used. Additional factors including the integration time, wind speed, and number of Zernikes used demonstrate a negligible impact on the distribution fit. Although the Poisson does not have the lowest error for the data analyzed, it can not be universally stated that Gaussian is better than Poisson. This data set was generated making assumption about the noise sources present. Not all possible noise sources are considered.

These findings indicate that for certain conditions, the mixed PDF results in the closest distribution match to the simulated PSF fluctuations. An important note is that the analysis performed is based on the statistics of a single pixel, the center pixel of the PSF. To generalize this analysis to include the entire PSF, it is assumed that each pixel in the PSF is independent. Moving from a point detection strategy to a matched filter, or entire PSF strategy, allows for more advanced detection algorithms. In reality, there may be a correlation in the temporal scintillation of adjoining pixels that propagate through similar portions of the atmosphere. This effect is not analyzed in this research effort. In the next section, the mixed distribution is implemented in a LLR test to determine the performance of the newly developed algorithm. The algorithms are compared on their ability to find potential RSOs.

### ***5.3.2 Receiver Operating Characteristic Curves.***

A Receiver Operating Characteristic (ROC) curve is a method of comparing the detection performance across the entire range of false alarm values. It is generated by sliding the threshold  $\tau$  from equation (5.6), and noting  $P_d$  and  $P_f$  value pairs at that threshold. To demonstrate the maximum performance achievable with this detection algorithm, simulated data is created with the mixed PDF developed in section 5.1.3.

Figure 5.3 shows two instances of simulated PSFs created with (A) a long exposure atmosphere, and (B) an atmosphere scintillated with the mixed negative binomial and Poisson distribution.

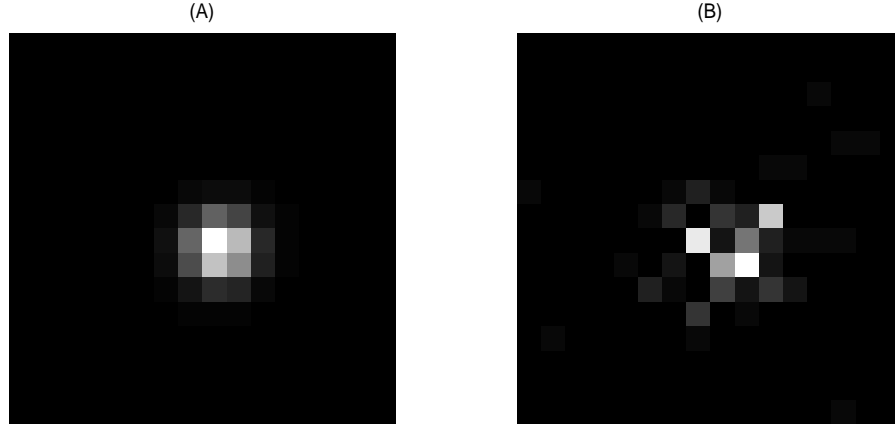


Figure 5.3: A demonstration of a simulated received PSF under two different conditions. In (A) a long exposure atmosphere model is used, and in (B) a PSF generated with the negative binomial and Poisson model or the ideal mixed PDF.

Using a Monte Carlo simulation of the PSFs, the detection performance of the two algorithms that most closely match the PSF fluctuations are investigated. These two distributions are the mixed and Gaussian PDFs. To produce a ROC curve, two types of data are needed. These two data sets are images with and without a RSO. Performing the detection algorithm on data with an object present gives the probability of detection, while performing the detection algorithm on data with no object present determines the probability of false alarm. Images without an RSO are generated by creating a flat background with a value of  $B$ , and adding Poisson photon counting noise.

One method of determining  $P_d$  and  $P_f$  is to compute the LLR and compare it against a threshold and assign either a one for a detection or a zero for no detection. This can be

done over a large number of independent Monte Carlo iterations. The ratio of detection or false alarms to the number of Monte Carlo iterations gives a value for  $P_d$  and  $P_f$ . This direct computational method requires significant data processing at each threshold value. In addition, the ROC curve is limited in false alarm range by the number of iterations performed. To achieve false alarm rates of  $10^{-5}$ , on average  $10^5$  iterations would be needed to generate a single false alarm.

Instead, a Monte Carlo simulation is performed with a large number of iterations,  $N = 1000$ , and the LLR statistics are analyzed. By investigating the statistics of the LLR, values for  $P_d$  and  $P_f$  can be calculated with a CDF. Figure 5.4 shows  $N = 100$  instances of LLR generated under two conditions (A) where the Gaussian detector is implemented and (B) where the mixed PDF detector is implemented.

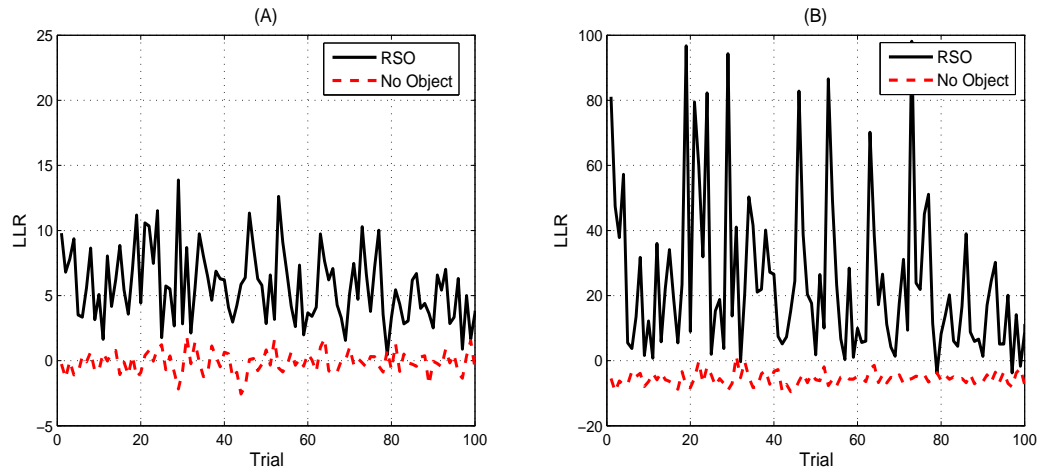


Figure 5.4: LLR observations over 100 Monte Carlo iterations. The LLR is generated for both the (A) Gaussian algorithm and the (B) mixed PDF algorithm.

The LLR values in the case where no RSO is present, shown as the dashed line in Figure 5.4, for both Gaussian and mixed PDF algorithms, closely follows a Gaussian distribution. Due to this fact, the LLR statistics can be summarized by their mean and

standard deviation. The LLR values with an RSO present utilizing the Gaussian detection algorithm is also Gaussian. The exceptions are the LLR values with an object present in the mixed PDF algorithm. Analyzing the data shows that it more closely follows an exponential distribution. This can be seen in Figure 5.4 (B), as the data tends to skew upwards of the mean instead of symmetrically around the mean.

In Figure 5.4,  $P_d$  is found by computing the CDF of the solid line using the statistics of the LLR and a sliding threshold value  $\tau$ . Alternatively,  $P_f$  is found by computing the CDF using the statistics of the dashed line and the threshold  $\tau$ . To ensure that the entire range of  $P_d$  and  $P_f$  values are investigated, it is necessary to use a threshold that spans from the most negative to the most positive potential LLR values. Using this method, ROC curves are found for both algorithms, and are shown in Figure 5.5.

For high  $P_f$  values, the algorithms perform similarly, but the mixed PDF algorithm shows  $P_d$  improvement as the acceptable  $P_f$  rate is decreased. The new algorithm demonstrates detection improvements of up to 35 percent for sufficiently low false alarm rates. The mixed PDF algorithm appears to begin at approximately  $P_f = 0.01$ , but actually has a  $P_d$  value of one and is difficult to distinguish from the plot border. Low  $P_f$  rates are typically where SDA systems operate, and as a result this algorithm can potentially have a benefit over the Gaussian.

For telescope systems with CCDs containing a large number of pixels, a low  $P_f$  is desirable. For example, a 512x512 array utilizing a false alarm rate of  $10^{-5}$  would still average approximately 2.6 false alarms per image. Depending on the program objectives and process timing requirements, this may or may not be an acceptable number of incorrectly identified RSOs. The performance achieved in this ROC curve is the theoretical maximum improvement. Factors including the independence of adjacent pixels and how closely the atmospheric conditions match the simulated parameters will determine the realizable detection increase of the new algorithm, including how many more RSOs can

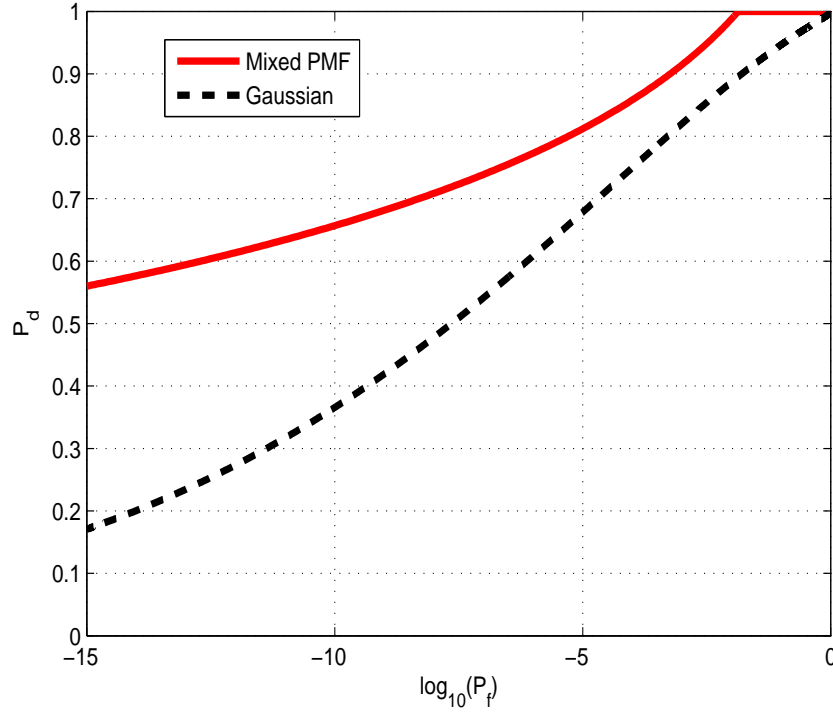


Figure 5.5: ROC curves comparing the new mixed PDF (solid line) against the traditional Gaussian detection algorithm (dashed line). These curves were generated with simulated RSO and background data.

be found. The better the seeing parameter  $r_o$  experienced, the less effective the new mixed PDF algorithm would perform. The equal performance point occurs at approximately 6cm, and the Gaussian algorithm has a larger  $P_d$  for larger  $r_o$  values.

Additionally, factors including spatial aliasing and integration time have a large impact on the effectiveness of this mixed PDF model. Spatial averaging due to aliasing can hide the intensity fluctuations that give this new algorithm its benefits. In the case of long integration times, the phase screen model is less accurate, and a long exposure atmosphere more accurately represents the received data.



## 5.4 Conclusions

This research demonstrates that under certain atmospheric conditions, a mixed PDF model combining negative binomial scintillation and Poisson background light can more accurately represent the received noise statistics of the atmosphere present in an observed PSF than a Gaussian assumption. For seeing values of less than 6cm, this new PDF is found to more accurately match received intensity fluctuations. Using this model under ideal assumptions, the mixed PDF model shows improvements of up to 35 percent detection for realistic  $P_f$  values typically used in SDA telescopes. Accounting for the scintillation that is present in the RSO data, but not the background data helps distinguish objects from the background. In this way, the additional atmospheric noise improves detection performance in this model.

There are a few areas related to the research presented in this chapter where additional future work could be performed. This work could be expanded in the future by applying the algorithm to collected telescope data. Only simulated data is investigated in this chapter, and to enable future implementation it is important to test the algorithms on collected telescope data. There are other methods of hypothesis testing besides LLR. Using an alternative detection algorithm along with the noise model described in this chapter may show additional benefits over a LLR.

This research did not investigate the optimal methods of estimating object signal strength  $S$  and the background  $B$ . There may be benefit to optimizing the estimation techniques for these parameters. In addition, it is assumed that the pixels in the data are statistically independent as well as the background and photons from the object of interest. The model could be expanded further by investigating the impacts of these assumptions being incorrect.

The next chapter discusses the conclusions and results from throughout this dissertation, as well as combining areas of future research. The contributions of this

research effort as well as a broad overview of how research fits into the field is also discussed.

## VI. Summary and Future Work

This chapter will summarize results and contributions of this dissertation as well as present potential topics for additional future work.

### 6.1 Work Completed

In chapter 1, a research goal and three associated research questions are presented. Throughout this dissertation and research, each of these questions is addressed and answered. In the following list, a summary of the research results that answer each question is included.

1. *Will a new realistic cost function improve the detection performance of a Bayes Criterion MHT?*

In chapter 3, it is shown that a new cost function in a MHT improves detection performance over traditional point detection approaches, BHT algorithms like Source Extractor, and ECEP MHT algorithms. It is demonstrated that the probability of detection is increased by using an UCEP MHT detection algorithm when compared to an ECEP algorithm.  $P_d$  gains of up to 80 percent are observed for the same  $P_f$  rate. The number of hypotheses used within the MHT is also investigated. It is found that there is a relationship between the number of hypotheses used and detection performance. The results show that a MHT clearly detects more objects than a BHT, and that using 6 hypotheses slightly outperforms the algorithm when 10 hypotheses are used, with the additional benefit of reduced computational time.

2. *Do the assignments of a priori probabilities in a MHT improve the detection performance?*

Chapter 4 addresses this research question. It is shown that increased performance is achievable, in both simulated and collected SST data. When tested with simulated

data, ROC curve analysis shows that the ECUP algorithm has a greater  $P_d$  than the ECEP algorithm for a large range of  $P_f$  values. At a relevant false alarm level of  $P_f = 10^{-10}$ , ECUP shows an average improvement of approximately 5 percent when tested over 100 Monte Carlo iterations.

When tested against collected SST data, this research demonstrates that for certain applications it may be beneficial to use an ECUP MHT algorithm. It is shown with high statistical confidence that the ECUP algorithm on average has more detections than an ECEP algorithm when performed on the SST data. For the small subset of frames analyzed, approximately 19-26 additional detections are found, which translates to 458-627 additional detections on average for full frame data. These objects are most likely threshold objects that are difficult for currently proposed detection algorithms to detect. Finding these threshold objects will provide additional information for tracking and characterization, in turn increasing SDA capabilities with the optical system.

### 3. *Can using a more realistic noise model for detection algorithms increase the ability to detect space objects?*

In chapter 5 it is shown that under certain atmospheric conditions, a mixed PDF model combining negative binomial scintillation and Poisson background light can more accurately represent the received noise statistics of the atmosphere present in an observed PSF than a Gaussian assumption. For seeing values of less than 6cm, this new PDF is found to more accurately match received intensity fluctuations. Using this model under ideal assumptions, the mixed PDF model shows improvements of up to 35 percent detection for realistic  $P_f$  values typically used in SDA telescopes. Accounting for the scintillation that is present in the RSO data, but not the background data, helps distinguish objects from the background. In this way, the additional atmospheric noise improves detection performance in this model.

## 6.2 Algorithm Comparison

Throughout this dissertation, several algorithms are presented that addresses the issues of spatial undersampling in CCD arrays, as well as the assumed noise distribution. In this section, the performances of the algorithms developed are compared and contrasted.

In a MHT, there are two key variables: the cost and prior probabilities. Table 6.1 shows how the chapters of this dissertation, as well as a previous research effort, relate to choices for costs and priors.

Table 6.1: Description of MHT algorithms including the assignment of costs and prior probabilities and where they are developed.

	<b>Equal-Cost</b>	<b>Unequal-Cost</b>
<b>Equal-Prior</b>	Zingarelli et. al. [24]	Chapter 3: UCEP
<b>Unequal-Prior</b>	Chapter 4: ECUP	N/A

Table 6.1 shows research into four different assumptions that can be used in a hypothesis test. In this case, the research relates to improvements in SDA detection techniques. Figure 6.1 is a diagram of the general relationship between computational complexity and  $P_d$  for SDA algorithms from other sources, as well as newly developed algorithms proposed in this dissertation.

Moving along the y-axis in figure 6.1 from bottom to the top increases the probability of detection. The algorithms above the x-axis all utilize multiple pixels to decide if an object is present. The point detector on the other hand uses only a single pixel to make decisions. Moving along the x-axis from left to right increases the complexity of the algorithm. Algorithms to the right of the y-axis use a MHT, while the matched filter and point detection techniques use a BHT.

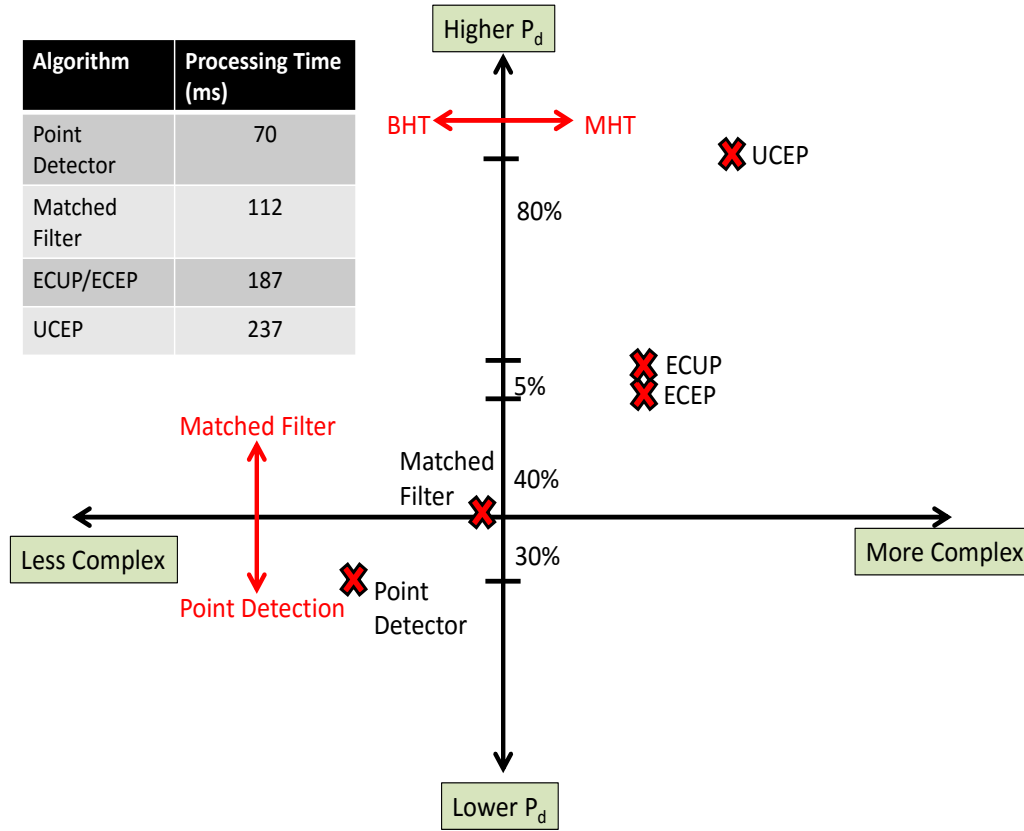


Figure 6.1:  $P_d$  versus computational complexity diagram for several SDA algorithms. Processing time for a full frame of SST data is also included.

The ECUP algorithm developed in Chapter 4 provides an improvement in  $P_d$ , and is slightly more complex due to the calculation of the weighting term  $W_k$ . The UCEP algorithm detects even more objects, but is more computationally complex.

### 6.3 Future Research Items

There are several opportunities for continued research based on the work presented in this dissertation. In each chapter ideas are included for potential future research. This section compiles and describes these future research items.

### Chapter 3 future work:

This research focuses on received data that is assumed to be Gaussian. Through this research, a method for implementing a different model for received data is developed that can be used on any potential distribution of received data. The limiting cases of costs are considered in this chapter. There are many additional cost structures in between the two presented here. For specific applications, these cases may give better detection performance. The drawback is that they will not reduce as well as the equal- or unequal-cost algorithms described in this dissertation. Additionally, the unequal cost method here is more computationally complex than the currently implemented algorithms. Simplification and efficient implementation are not a focus of this research. To use this algorithm operationally, these factors will need to be investigated further.

### Chapter 4 future work:

The ECUP algorithm developed assumed Gaussian received noise in this chapter. In the future, removing the Gaussian assumption may detect additional space objects. Additional methods can be combined to potentially improve detection performance even further. For example, using a Unequal-Cost Unequal-Prior (UCUP) algorithm may improve detection performance when compared to an ECUP algorithm.

In the ECEP MHTs, the threshold is considered constant for each hypothesis. As a result, the modeled intensity is effectively different for each hypothesis, dependent on the distribution of the PSF. This assumption is changed in this paper for the ECUP algorithm. This assumption can be removed in a future ECEP test, and may provide interesting research opportunities and advancements.

Another consideration is how including unequal-priors may affect the ability to translate the detected objects into accurate tracking and orbit determination. The ECUP

algorithm takes into account the probability of the alternate hypotheses, each of which correspond to a sub-pixel position. The sub-pixel information gathered from performing a ECUP test may lead to improved sub-pixel position, and in turn, more accurate tracking of detected RSOs.

#### Chapter 5 future work:

There are a few areas related to the research presented in this chapter where additional future work could be performed. This work could be expanded in the future by applying the algorithm to collected telescope data. Only simulated data was investigated in this chapter. To enable future implementation, it is important to test the algorithms on collected telescope data. There are other methods of hypothesis testing besides LLR. Using an alternative detection algorithm along with the noise model described in this chapter may yield additional benefits over a LLR.

This research did not investigate the optimal methods of estimating object signal strength  $S$  and the background  $B$ . There may be benefits to optimizing the estimation techniques for these parameters. In addition, it is assumed that the pixels in the data are statistically independent, as well as the background and photons from the object of interest. The model could be expanded further by investigating the impacts of these assumptions being incorrect.

One final area that may be beneficial to address in the future is an Unequal-Cost Unequal-Prior (UCUP) algorithm. This algorithm is not discussed in this dissertation, but could improve detection performance above what was demonstrated with UCEP. It would be the most computationally complex, and would not provide sub-pixel information, as is the case with the UCEP algorithm.



## 6.4 Publications

To ensure this work is novel and well received by the community, several portions of this dissertation have been submitted for conference and journal papers. In total, two journal articles and two conference papers have been written and submitted.

### Journals:

- **Based on Chapter 3:**

T. Hardy, S. Cain, J. Jeon, and T. Blake. “*Improving space domain awareness through unequal-cost multiple hypothesis testing in the space surveillance telescope.*” Applied Optics 54.17 (2015): 5481-5494.

- **Based on Chapter 4:**

T. Hardy, S. Cain, and T. Blake. “*Unequal A Priori Probability Multiple Hypothesis Testing in Space Domain Awareness with the Space Surveillance Telescope.*” Applied Optics. Accepted April 2016

### Conference Papers and Presentations:

- **Based on Chapter 5:**

T. Hardy and S. Cain. “*Characterizing point spread function (PSF) fluctuations to improve resident space object detection (RSO),*” in SPIE Defense+ Security, International Society for Optics and Photonics, 2015.

- **Based on Chapter 4:**

T. Hardy and S. Cain. “*Investigating prior probabilities in a multiple hypothesis test for use in space domain awareness,*” in SPIE Defense+ Security, International Society for Optics and Photonics, 2016.

## Bibliography

- [1] Defense Advanced Research Projects Agency (DARPA), “Space Surveillance Telescope (SST) - Our Work.” [http://www.darpa.mil/Our\\_Work/TTO/Programs/Space\\_Surveillance\\_Telescope\\_\(SST\).aspx](http://www.darpa.mil/Our_Work/TTO/Programs/Space_Surveillance_Telescope_(SST).aspx), 2014. [Online; accessed 2-June-2014].
- [2] Department of Defense Directive 3100.10, “Space policy,” 2012.
- [3] United States Government, “NATIONAL SPACE POLICY of the UNITED STATES of AMERICA,” 2010.
- [4] J. Finch, “Sustainability and the National Security Space Strategy: an Approach to the Congested Environment,” 2012. Office of the Under Secretary of Defense for Policy.
- [5] NASA Orbital Debris Program Office, “<http://orbitaldebris.jsc.nasa.gov/photogallery/beehives.html>.” <http://orbitaldebris.jsc.nasa.gov/photogallery/beehives.html>, 2014. [Online; accessed 25-Nov-2014].
- [6] United States Government, “Public Law 109-155, NASA Authorization Act 2005,” 2005. 109th United States Congress.
- [7] Committee to Review Near-Earth Object Surveys and Hazard Mitigation Strategies Space Studies Board; National Research Council, *Defending Planet Earth: Near-Earth Object Surveys and Hazard Mitigation Strategies*. The National Academies Press, 2010.
- [8] P. Martin, “NASAs Efforts to Identify Near-Earth Objects and Mitigate Hazards,” tech. rep., NASA Inspector General, 2014.
- [9] C. R. Chapman, D. Morrison, *et al.*, “Impacts on the earth by asteroids and comets: assessing the hazard,” *Nature*, vol. 367, no. 6458, pp. 33–40, 1994.
- [10] D. Morrison, C. R. Chapman, P. Slovic, *et al.*, “The impact hazard,” *Hazards due to Comets and Asteroids*, vol. 24, p. 59, 1994.
- [11] J. S. Stuart and R. P. Binzel, “Bias-corrected population, size distribution, and impact hazard for the near-earth objects,” *Icarus*, vol. 170, no. 2, pp. 295–311, 2004.
- [12] R. Willstrop, “The mersenne–schmidt: a three-mirror survey telescope,” *Monthly Notices of the Royal Astronomical Society*, vol. 210, no. 3, pp. 597–609, 1984.
- [13] J. Zingarelli, “Enhancing Ground Based Telescope Performance with Image Processing.” Air Force Institute of Technology AFIT-ENG-DS-13-D-04, 2013.
- [14] J. Scotti, “Near-earth object surveying in the late 20th century,” in *Completing the Inventory of the Solar System*, vol. 107, pp. 107–113, 1996.

- [15] G. H. Stokes, J. B. Evans, H. E. Viggh, F. C. Shelly, and E. C. Pearce, "Lincoln near-earth asteroid program (linear)," *Icarus*, vol. 148, no. 1, pp. 21–28, 2000.
- [16] H. Viggh, G. Stokes, F. Shelly, M. Blythe, and J. Stuart, "Applying Electro-Optical Space Surveillance Technology to Asteroid Search and Detection: The Linear Program Results," in *Proceedings of the 1998 Space Control Conference*, 1998.
- [17] J. Goodman, *Statistical Optics*. New York: John Wiley & Sons, Inc, 2000.
- [18] E. Bertin and S. Arnouts, "SExtractor: Software for source extraction," *Astronomy and Astrophysics Supplement Series*, vol. 117, no. 2, pp. 393–404, 1996.
- [19] E. Bertin and M. Dennefeld, "Galaxy evolution at low redshift?—i. optical counts," *Arxiv preprint astro-ph/9602110*, 1996.
- [20] E. Bertin, "Automated morphometry with sextractor and psfex," in *Astronomical Data Analysis Software and Systems XX*, vol. 442, p. 435, 2011.
- [21] P. Gural, J. Larsen, and A. Gleason, "Matched filter processing for asteroid detection," *The Astronomical Journal*, vol. 130, no. 4, p. 1951, 2005.
- [22] S. Pohlig, "An Algorithm for Detection of Moving Optical Targets," *IEEE Transactions on Aerospace and Electronic Systems*, vol. AES-25, no. 1, pp. 56–63, 1989.
- [23] A. O'Dell, "Detecting Near-Earth Objects Using Cross-Correlation with a Point Spread Function.." Air Force Institute of Technology AFIT/GE/ENG/09-30, 2009.
- [24] J. Zingarelli, E. Pearce, R. Lambour, T. Blake, C. Peterson, and S. Cain, "Improving the Space Surveillance Telescope's Performance Using Multi-Hypothesis Testing," *The Astronomical Journal*, vol. 147, no. 5, p. 111, 2014.
- [25] H. V. Trees, *Detection, Estimation, and Modulation Theory*. John Wiley and Sons, Inc., 1968.
- [26] E. Ertin and L. Potter, "Polarimetric classification of scattering centers using m-ary bayesian decision rules," *Aerospace and Electronic Systems, IEEE Transactions on*, vol. 36, no. 3, pp. 738–749, 2000.
- [27] C. Baum and M. Pursley, "Bayesian methods for erasure insertion in frequency-hop communication systems with partial-band interference," *Communications, IEEE Transactions on*, vol. 40, no. 7, pp. 1231–1238, 1992.
- [28] N. Goodman, P. R. Venkata, and M. Neifeld, "Adaptive waveform design and sequential hypothesis testing for target recognition with active sensors," *Selected Topics in Signal Processing, IEEE Journal of*, vol. 1, no. 1, pp. 105–113, 2007.
- [29] M. D. Richard and R. P. Lippmann, "Neural network classifiers estimate bayesian a posteriori probabilities," *Neural computation*, vol. 3, no. 4, pp. 461–483, 1991.

- [30] J. Ediriwickrema and S. Khorram, “Hierarchical maximum-likelihood classification for improved accuracies,” *Geoscience and Remote Sensing, IEEE Transactions on*, vol. 35, no. 4, pp. 810–816, 1997.
- [31] R. M. Everson and J. E. Fieldsend, “Multi-class roc analysis from a multi-objective optimisation perspective,” *Pattern Recognition Letters*, vol. 27, no. 8, pp. 918–927, 2006.
- [32] F. B. Butar and P. Lahiri, “On measures of uncertainty of empirical bayes small-area estimators,” *Journal of Statistical Planning and Inference*, vol. 112, no. 1, pp. 63–76, 2003.
- [33] K. R. Varshney and L. R. Varshney, “Quantization of prior probabilities for hypothesis testing,” *arXiv preprint arXiv:0805.4338*, 2008.
- [34] J. Goodman, *Introduction to Fourier Optics*. Englewood, Co: Roberts & Company, 3rd ed., 2005.
- [35] C. Peterson, “Near Earth Object Detection using a Poisson Statistical Model for Detection on Images Modeled from the Panoramic Survey Telescope & Rapid Response System..” Air Force Institute of Technology AFIT/GE/ENG/12-33, 2012.
- [36] L. Andrews and R. Phillips, *Laser Beam Propagation through Random Media*. Bellingham, Washington: SPIE, 2nd ed., 2005.
- [37] F. Roddier, “The effects of atmospheric turbulence in optical astronomy,” *Progress in optics*, vol. 31, pp. 281–281, 1993.
- [38] M. Al-Habash, R. Phillips, and L. Andrews, “Mathematical model for the irradiance probability density function of a laser beam propagating through turbulent media,” *Optical Engineering*, vol. 40, no. 8, pp. 1554–1562, 2001.
- [39] R. Racine, G. Walker, D. Nadeau, R. Doyon, and C. Marois, “Speckle noise and the detection of faint companions,” *Publications of the Astronomical Society of the Pacific*, vol. 111, no. 759, pp. 587–594, 1999.
- [40] T. Fusco, J. Conan, L. Mugnier, V. Michau, and G. Rousset, “Characterization of adaptive optics point spread function for anisoplanatic imaging. application to stellar field deconvolution,” *Astronomy and Astrophysics Supplement Series*, vol. 142, no. 1, pp. 149–156, 2000.
- [41] D. Monet, T. Axelrod, C. Claver, T. Blake, R. Lupton, E. Pearce, R. Shah, and D. Woods, “Rapid cadence collections with the space surveillance telescope,” tech. rep., DTIC Document, 2012.
- [42] E. Marchetti, N. N. Hubin, E. Fedrigo, J. Brynnel, B. Delabre, R. Donaldson, F. Franza, R. Conan, M. Le Louarn, C. Cavadore, *et al.*, “Mad the eso multi-conjugate

- adaptive optics demonstrator,” in *Astronomical Telescopes and Instrumentation*, pp. 317–328, International Society for Optics and Photonics, 2003.
- [43] University of California Berkeley Astronomy Department, “Adaptive Optics Near-Infrared Imaging: Orbital Motion in a Young Triple System.” <http://ugastro.berkeley.edu/infrared10/adaptiveoptics/index.html>, 2014. [Online; accessed 25-Nov-2014].
  - [44] D. Kundur and D. Hatzinakos, “Blind image deconvolution,” *Signal Processing Magazine, IEEE*, vol. 13, no. 3, pp. 43–64, 1996.
  - [45] J. Rhodes, R. Massey, J. Albert, N. Collins, R. Ellis, C. Heymans, J. Gardner, J. Kneib, A. Koekemoer, and A. Leauthaud, “The stability of the point-spread function of the advanced camera for surveys on the hubble space telescope and implications for weak gravitational lensing,” *The Astrophysical Journal Supplement Series*, vol. 172, no. 1, p. 203, 2007.
  - [46] D. Fried, “Optical resolution through a randomly inhomogeneous medium for very long and very short exposures,” *JOSA*, vol. 56, no. 10, pp. 1372–1379, 1966.
  - [47] C. Roddier and J. Vernin, “Relative contribution of upper and lower atmosphere to integrated refractive-index profiles,” *Applied optics*, vol. 16, no. 8, pp. 2252–2256, 1977.
  - [48] J. Caccia, M. Azouit, and J. Vernin, “Wind and  $c_n^2$  profiling by single-star scintillation analysis,” *Applied optics*, vol. 26, no. 7, pp. 1288–1294, 1987.
  - [49] A. Sivaramakrishnan, J. Lloyd, P. Hodge, and B. Macintosh, “Speckle decorrelation and dynamic range in speckle noise-limited imaging,” *The Astrophysical Journal Letters*, vol. 581, no. 1, p. L59, 2002.
  - [50] G. Potvin, J. Forand, and D. Dion, “Some theoretical aspects of the turbulent point-spread function,” *JOSA A*, vol. 24, no. 9, pp. 2932–2942, 2007.
  - [51] V. I. Tatarskii, “Wave propagation in turbulent medium,” *Wave Propagation in Turbulent Medium, by Valerian Ilich Tatarskii. Translated by RA Silverman. 285pp. Published by McGraw-Hill, 1961.*, vol. 1, 1961.
  - [52] V. I. Tatarskii, “The effects of the turbulent atmosphere on wave propagation,” 1971.
  - [53] G. Parry, “Measurement of atmospheric turbulence induced intensity fluctuations in a laser beam,” *Journal of Modern Optics*, vol. 28, no. 5, pp. 715–728, 1981.
  - [54] R. L. Phillips and L. C. Andrews, “Measured statistics of laser-light scattering in atmospheric turbulence,” *JOSA*, vol. 71, no. 12, pp. 1440–1445, 1981.
  - [55] M. Jee, J. Blakeslee, M. Sirianni, A. Martel, R. White, and H. Ford, “Principal component analysis of the time- and position-dependent point-spread function of the advanced camera for surveys,” *Publications of the Astronomical Society of the Pacific*, vol. 119, no. 862, pp. 1403–1419, 2007.

- [56] D. Dravins, L. Lindegren, E. Mezey, and A. Young, “Atmospheric intensity scintillation of stars. i. statistical distributions and temporal properties,” *Publications of the Astronomical Society of the Pacific*, pp. 173–207, 1997.
- [57] J. Schmidt, *Numerical Simulation of Optical Wave Propagation with examples in MATLAB*. Bellingham, Washington: SPIE, 2010.
- [58] S. Cain and D. Richmond, *Direct-Detection LADAR Systems*. Bellingham, Washington: SPIE, 2010.
- [59] A. Kolmogorov, “The local structure of turbulence in incompressible viscous fluid for very large reynolds numbers,” in *Dokl. Akad. Nauk SSSR*, vol. 30, pp. 299–303, 1941.
- [60] A. Kolmogorov, “A refinement of previous hypotheses concerning the local structure of turbulence in a viscous incompressible fluid at high reynolds number,” *Journal of Fluid Mechanics*, vol. 13, no. 01, pp. 82–85, 1962.
- [61] F. Roddier, M. Northcott, J. Graves, D. McKenna, and D. Roddier, “One-dimensional spectra of turbulence-induced zernike aberrations: time-delay and isoplanicity error in partial adaptive compensation,” *JOSA A*, vol. 10, no. 5, pp. 957–965, 1993.
- [62] R. Noll, “Zernike Polynomials and Atmospheric Turbulence,” *J. Opt. Soc. Am.*, vol. 66, pp. 207–211, 1976.
- [63] D. Woods, “The Space Surveillance Telescope: Focus and Alignment of a Three Mirror Telescope.” Advanced Maui Optical and Space Surveillance Technologies Conference, 2012.
- [64] S. Kay, *Fundamentals of Statistical Signal Processing Estimation Theory*, vol. 1. Prentice-Hall, Inc., 1993.
- [65] S. Kay, *Fundamentals of Statistical Signal Processing, Vol. II: Detection Theory*. 1998.
- [66] G. Healey and R. Kondepudy, “Radiometric CCD Camera Calibration and Noise Estimation,” *Pattern Analysis and Machine Intelligence, IEEE Transactions on*, vol. 16, pp. 267–276, Mar 1994.
- [67] T. Hardy, S. Cain, J. Jeon, and T. Blake, “Improving space domain awareness through unequal-cost multiple hypothesis testing in the space surveillance telescope,” *Appl. Opt.*, vol. 54, pp. 5481–5494, Jun 2015.
- [68] T. J. Hardy and S. C. Cain, “Characterizing point spread function (psf) fluctuations to improve resident space object detection (rso),” in *SPIE Defense+ Security*, pp. 946904–946904, International Society for Optics and Photonics, 2015.
- [69] A. Sligar, “Measuring Angular Rate of Celestial Objects using the Space Surveillance Telescope..” Air Force Institute of Technology AFIT-ENG-MS-15-M-019, 2015.

- [70] D. E. Knuth, “Two notes on notation,” *American Mathematical Monthly*, pp. 403–422, 1992.
- [71] J. S. Milton and J. C. Arnold, *Introduction to probability and statistics: principles and applications for engineering and the computing sciences*. McGraw-Hill, Inc., 2002.
- [72] A. Leon-Garcia, *Probability, Statistics, and Random Processes for Electrical Engineering*. Prentice Hall, 2008.

REPORT DOCUMENTATION PAGE					Form Approved OMB No. 0704-0188	
<p>The public reporting burden for this collection of information is estimated to average 1 hour per response, including the time for reviewing instructions, searching existing data sources, gathering and maintaining the data needed, and completing and reviewing the collection of information. Send comments regarding this burden estimate or any other aspect of this collection of information, including suggestions for reducing this burden to Department of Defense, Washington Headquarters Services, Directorate for Information Operations and Reports (0704-0188), 1215 Jefferson Davis Highway, Suite 1204, Arlington, VA 22202-4302. Respondents should be aware that notwithstanding any other provision of law, no person shall be subject to any penalty for failing to comply with a collection of information if it does not display a currently valid OMB control number. PLEASE DO NOT RETURN YOUR FORM TO THE ABOVE ADDRESS.</p>						
1. REPORT DATE (DD-MM-YYYY)		2. REPORT TYPE		3. DATES COVERED (From — To)		
15-09-2016		Doctoral Dissertation		Sep 2013-Sep 2016		
4. TITLE AND SUBTITLE  Optical Theory Improvements to Space Domain Awareness				5a. CONTRACT NUMBER		
				5b. GRANT NUMBER		
				5c. PROGRAM ELEMENT NUMBER		
6. AUTHOR(S)  Hardy, Tyler J., Captain, USAF				5d. PROJECT NUMBER  16G288		
				5e. TASK NUMBER		
				5f. WORK UNIT NUMBER		
7. PERFORMING ORGANIZATION NAME(S) AND ADDRESS(ES) Air Force Institute of Technology Graduate School of Engineering and Management (AFIT/EN) 2950 Hobson Way WPAFB, OH 45433-7765				8. PERFORMING ORGANIZATION REPORT NUMBER  AFIT-ENG-DS-16-S-011		
9. SPONSORING / MONITORING AGENCY NAME(S) AND ADDRESS(ES)  Julie J. Moses Air Force Office of Scientific Research 875 N Randolph St, Arlington, VA 22203 (703) 696-9586				10. SPONSOR/MONITOR'S ACRONYM(S)  AFOSR/RTB		
				11. SPONSOR/MONITOR'S REPORT NUMBER(S)		
12. DISTRIBUTION / AVAILABILITY STATEMENT DISTRIBUTION STATEMENT A: APPROVED FOR PUBLIC RELEASE; DISTRIBUTION UNLIMITED						
13. SUPPLEMENTARY NOTES This work is declared a work of the U.S. Government and is not subject to copyright protection in the United States.						
14. ABSTRACT This dissertation focuses on increasing the ability to detect space objects and increase Space Domain Awareness (SDA) with space surveillance sensors through image processing and optical theory. SDA observations are collected through ground-based radar and optical systems as well as space based assets. This research focuses on a ground-based optical telescope system, the Space Surveillance Telescope (SST). By increasing the number of detectable Resident Space Objects (RSOs) through image processing, SDA capabilities can be expanded. This is accomplished through addressing two main degrading factors present in typical SDA sensors; spatial undersampling in the collected data and noise models and assumptions used in current algorithms. The assigned cost and a priori probabilities of a Bayes Multiple Hypothesis Test (MHT) are investigated in this dissertation to address the spatial undersampling. New algorithms are developed and tested, and demonstrated improved detection capabilities at operationally realistic false alarm rates. Additionally, a new noise model is developed which more accurately represents the received noise present in data collected with surveillance telescopes under certain atmospheric conditions. These algorithm have demonstrated probability of detection improvement of up to 80 percent in collected SST data over the currently employed detection techniques.						
15. SUBJECT TERMS Telescope, Detection, Optics, Atmosphere, Space Domain Awareness						
16. SECURITY CLASSIFICATION OF:			17. LIMITATION OF ABSTRACT	18. NUMBER OF PAGES	19a. NAME OF RESPONSIBLE PERSON	
a. REPORT	b. ABSTRACT	c. THIS PAGE			Stephen C. Cain (ENG)	
U	U	U	U	152	19b. TELEPHONE NUMBER (include area code) (937) 255-3636 x4716 stephen.cain@afit.edu	